Source and Fate of Contaminants in a Pit Lake and Water Treatment at the Faro Mine Complex

by

Esteban Larrea

A thesis

presented to the University of Waterloo

in fulfillment of the

thesis requirement for the degree of

Master of Science

in

Earth Sciences

Waterloo, Ontario, Canada, 2022

Author's Declaration

I hereby declare that I am the sole author of this thesis. This is a true copy of the thesis, including any required final revisions, as accepted by my examiners.

I understand that my thesis may be made electronically available to the public.

Abstract

The Faro Mine Complex (FMC) is an abandoned zinc-lead mine in Yukon, Canada that requires extensive remediation efforts to manage the environmental liabilities associated with mine wastes stockpiled at the site. Active care and maintenance are necessary to manage surface water and groundwater impacted by acid rock drainage (ARD) and metal leaching (ML). The Faro Pit lake (FPL) is the largest reservoir of water at the FMC, multiple mine impacted water sources are pumped to the pit lake for storage and mixing. The FPL is also the main influent source to the FMC treatment plant. Active pumping from other mine components and continuous degradation of ARD seepage quality flowing into the pit lake alter the concentration and distribution of contaminants at the FMC. Changes to the load balance of the site may therefore affect contaminant removal processes at the FMC treatment plant. This research project aims to combine a mass balance of contaminant loading in water at the FMC with the characterization of metal removal during the treatment of mine waters. The results would characterize the source, distribution, and fate of contaminants within the FPL.

A sampling apparatus was installed into the FPL on two occasions, in September 2019 and September 2021. Profile samples and *in situ* measurements were obtained to a depth of 47 m in 2019 and 25 m in 2021. In both years, the pit lake was thermally stratified with a well-defined thermocline between 8 m and 10 m depth. The stratification is caused by the difference in specific density of water at 10 ºC and 4 ºC, in the epilimnion and hypolimnion respectively. Multiple parameters changed sharply at the well-defined thermocline because mixing between the epilimnion and hypolimnion is limited. In 2019, most concentrations of dissolved species were higher in the hypolimnion than in the epilimnion, whereas the concentrations were generally higher in the epilimnion in 2021. The pH was higher in the epilimnion in 2019, and in 2021 it was lower in the epilimnion at pH 3.8. Increasing contaminant loads from the tailings area Intermediate Pond and seepage from the mine waste surrounding the Faro Pit drive geochemical changes in the pit-lake water quality.

Batch experiments were conducted to understand the processes resulting in removal of dissolved metals during treatment of mine-impacted waters. FPL water samples were placed in a stirred cell reactor (SCR) and dosed with calcium hydroxide to a pH of 10. Samples were collected for characterization of kinetic and thermodynamic controls during water treatment. Contaminant removal during lime treatment is controlled by processes that occur consistently over narrow pH ranges. Results of the batch experiments show that most Fe removal occurred at pH 6.5, Zn was removed at pH 9, Mn removal at pH 9.7, and Ni and Cd removal occurred above pH 10. Characterization of the precipitated solids showed that Fe and some Zn coprecipitated in the initial stage of the experiments. Later in the experiment, Zn precipitated separately, likely as amorphous Zn hydroxides, mixed with Mn (hydr)oxides. The solution remained undersaturated in respect to gypsum and minimal removal of SO_4 from solution was observed.

The results from all components of this study suggest that changing geochemical conditions and additional load sources have the potential to change the contaminant distribution and effectiveness of treatment process. This study increased the understanding of the necessary actions to efficiently remove contaminants from a mine with deteriorating water quality and changing operating conditions.

Acknowledgements

I would like to thank my supervisor Dr. David Blowes, for his mentorship and support. I appreciated your insightful answers to all my technical questions and sharing your understanding of "the big picture". I would also like to thank my committee members: Dr. Andrea Brookfield and Dr. Peter Huck for their valuable feedback and thoughtful questions.

I would like to thank the members of the GGR team that were colleagues, mentors, and most importantly friends. Mainly David Hilger, David Geuder, Emily Saurette, Joanne Angai, Alexei Tarnopolski, and Peter Van Eck. Thank you Krista Elena and Steve Holland, your support in the early stages of my degree taught me about planning and conceptualization of the research. Thank you for the hard work and support from co-op students Olivia Clay, Matthew Erdelsky, and Dana Hallman.

I would like to express my gratitude to Jeff Bain, David Wilson, and Zhongwen Bao. Thanks for the valuable lessons, support in planning, hard work, and good times in the field; it was a pleasure working alongside you.

Thank you to my family for encouraging me to work hard and pursue my interests and ambitions. Finally, and most importantly, I would like to thank Joanne Doyle. Your support, patience, and love meant the world to me. I enjoyed our life in Waterloo and all the wonderful things that came from our years there.

Table of Contents

List of Figures

List of Tables

List of Abbreviations

ARD	Acid rock drainage
EC	Electrical conductivity
EDS	Energy dispersive X-ray spectroscopy
FMC	Faro Mine Complex
FPL	Faro Pit Lake
IP	Intermediate Pond
MDMER	Metal and Diamond Mining Effluent Regulations
ML	Metal leaching
N/A	Parameter not measured
NRD	Neutral rock drainage
RCTF	Rose Creek Tailings Facility
rpm	Revolutions per minute
SCR	Stirred cell reactor
SEM	Scanning electron microscope
TDS	Total dissolved solids
XRD	X-ray powder diffraction

Chapter 1: Introduction

1.1 Mining Waste

Extraction of metal ores generates large quantities of waste materials. After the operational life-cycle of a project, these materials continue to pose an environmental risk. At many abandoned mines, closure efforts have not successfully eliminated the social and environmental liability associated with the extractive activities. Often the most serious concern with abandoned mines is the generation of acidic drainage from exposed rock and mill-tailings. Acid rock drainage (ARD) is produced by the oxidation of sulfide minerals in contact with oxygen and water, resulting in drainage with low pH and high concentrations of dissolved metals and metalloids. Deterioration of water quality affects receiving environments because low pH and high concentrations of dissolved metal can be toxic for aquatic organisms, plant life, and municipal water supply. Managing ARD can be complex because it is challenging to predict the quality and quantity of contaminated water generated from the different components of a mine. In addition, management solutions often involve high capital costs and continuous care and maintenance.

The extraction and milling processes of mine operations result in large volumes of waste rock and mill-tailings, considered too dilute in regards to elements of economic interest for the metallurgical extraction process (Blowes et al. 2014). To access ore deposits, overburden must be excavated and stockpiled in waste-rock piles. The ore that is extracted is milled to concentrate the valuable elements. Waste rock and mill-tailings contain iron sulfide minerals, which can oxidize and can lead to effluent with acidic pH, and high concentrations of sulfate, iron, and metals (Evangelou and Zhang 1995). The rate of acid drainage generation is controlled by the rate of oxidation of sulfide minerals. Subsequent geochemical reactions may change the composition and pH of seepage from a given mine component (Johnson et al. 2000). Often, the geochemical conditions within the waste rock or tailings do not result in acidic conditions, yet water drainage has high concentrations of sulfate, metals, and metalloids, characterized as neutral mine drainage (NMD) (Amos et al. 2015).

1.2 Generation of ARD

Pyrite is the principal sulfide mineral found in most mine wastes. The oxidation of pyrite in mine wastes is complex, as it is dependent on factors such as pH, ρO_2, mineral morphology, and presence of catalyzing bacteria (Amos et al. 2015). The oxidation of pyrite occurs when it is exposed to O_2 and H_2O:

$$FeS_{2(s)} + \frac{7}{2}O_2 + H_2O \rightarrow Fe^{2+} + 2SO_4^{2-} + 2H^+ \quad [1.1]$$

$$Fe^{2+} + \frac{1}{4}O_2 + H^+ \rightarrow Fe^{3+} + \frac{1}{2}H_2O \quad [1.2]$$

$$Fe^{3+} + 3H_2O \rightarrow Fe(OH)_3 + 3H^+ \quad [1.3]$$

$$FeS_{2(s)} + \frac{15}{4}O_{2(aq)} + \frac{7}{2}H_2O \rightarrow 2SO_4^{-2} + Fe(OH)_{3(s)} + 4H^+_{(aq)} \quad [1.4]$$

During reaction [1.1], Fe(II) may further oxidize to Fe(III) and form amorphous ferric hydroxide [$Fe(OH)_3$; Reaction 1.3] to produce two additional moles of H^+, as shown in the combination of reactions 1.2 and 1.3 (Amos et al. 2015). The overall pyrite oxidation reaction [Reaction 1.4] produces four moles of H^+ for each mole of pyrite. The primary electron acceptors involved in pyrite oxidation in mine waste are atmospheric oxygen and Fe(III). The oxidation products formed on pyrite surfaces depend on the solution pH, the stability of these species dictates the overall oxidation rate (Todd et al. 2003). Under acidic conditions (pH<4) Fe(III) is the prevalent pyrite oxidant, as the rate of oxidation by molecular oxygen slows under low pH conditions (Singer and Stumm, 1970). Iron-oxidizing bacteria catalyze the oxidation of Fe(II) (Evangelou and Zhang 1995; Blowes et al. 2014).

Acidic drainage may be progressively neutralized as it migrates through the mine waste and reacts with gangue minerals, increasing the solution pH. The migration of dissolved metal species is controlled by two contrary sets of reactions: acid generation from sulfide minerals and acid neutralization by gangue minerals (Jurjovec 2002). The acid-consuming reactions result in the release of cations into solution, e.g., Ca, Mg, Mn, Fe, which may re-precipitate as secondary oxy-hydroxide and sulfate minerals (Gunsinger et al. 2006).

The most prevalent minerals that dissolve to neutralize the mine drainage pH are: carbonates, aluminum hydroxides, ferric oxyhydroxides, and aluminosilicate minerals; reaction [1.5] and [1.6] show the dissolution of calcite (Blowes et al. 2014).

$$CaCO_3 + H^+ \leftrightarrow Ca^{2+} + HCO_3^- \quad [1.5]$$

$$CaCO_3 + 2H^+ \leftrightarrow Ca^{2+} + CO_2 + H_2O \quad [1.6]$$

Acid-neutralizing reactions control the pH of mine water as it migrates, the availability and depletion of a reacting phases may cause a sequence of sharp changes in pH along the water flow path (Johnson et al. 2000). The accounting of neutralization and acid-producing potentials of mine waste repositories can predict the likelihood of mine waste to generate acidic drainage (Jambor et al. 2007).

1.3 Site Description

The Faro Mine Complex (FMC) is an abandoned zinc, lead, and accessory silver mine that operated between 1969 and 1998 close to the town of Faro, Yukon, Canada. The FMC is located approximately 350 km northeast of Whitehorse, Canada (Figure 1.1). The Faro Mine was once the largest open pit lead-zinc mine in the world (CIRNAC 2019). Currently, it is one of the largest and most complex mine remediation projects in Canada. The site elevation is between 1000 m and 1400 m above sea level. The climate is subarctic, characterized by long winters and short summers. The mine, which extends over 25 km^2, is currently owned by the Government of Canada. The FMC is presently under care and maintenance and closure planning stages, with the objective of maintaining site safety and reducing environmental impacts to surrounding receptors.

More than 320 MT of waste rock and more than 70 MT of tailings were generated and deposited on site through the production of lead and zinc concentrates. The FMC can be subdivided into three mine components: Faro Mine, Rose Creek Tailings Facility (RCTF), and Vangorda Plateau (Figure 1.2). This study will mainly focus on the Faro Mine and RCTF components of the property. The Faro Mine consists of waste-rock piles, surrounding a partially inundated open pit containing mine impacted water. The RCTF retains 25,500,000

m^3 of process tailings separated into three impoundments. Supernatant water accumulates in the Intermediate Pond (IP), located on the west side of the RCTF. Immediately downstream of the IP, the Cross Valley Pond (CVP), a pond previously used for polishing or seepage capture is now filled with contaminated water. Water flow through the FMC is constantly monitored and managed, with the goal to capture and treat mine-impacted water and diversion of non-contact water. Surface and groundwater are impacted by acid rock drainage (ARD) and metal leaching (ML) resulting from the weathering of sulfide minerals and the release and transport of contaminated drainage, which requires treatment to minimize environmental impacts. The current contaminants of concern at the site are Pb, Zn, Cd, Fe and SO_4^{2-}.

The Faro Pit has an area of approximately 1 km^2 and is filled with water to a depth between 40 m and 100 m. Supernatant tailings water and mine-impacted groundwater, intercepted by the different mine components, is pumped to and stored in the Faro Pit, which is presently the largest reservoir of contaminated water on site. Contaminated water is pumped from the pit for treatment and subsequently released to the environment following treatment. Calcium oxide is used at the FMC to treat around 6 million m^3 of mine-impacted water per year. Treating such a large volume of water is costly, and water treatment will be necessary for the foreseeable future. The treatment influent quality is likely to change as the oxidation of sulfide minerals continues at the waste rock and tailings impoundments. Removal of contaminants from mine-impacted water prior to discharge from the site is crucial to conserve the aquatic ecosystems downstream of the FMC.

1.4 Research Objectives

The overall goal of the thesis work is to develop tools and analyses to aid effective water management at the FMC. Moreover, the aim of the thesis is to provide a conceptual model and actions to promote the efficient removal contaminants from a mine site with deteriorating water quality and changing operating conditions. The specific research objectives are:

1. Assess the mass balance of water and contaminants into the Faro Pit; determine the loading rates and distribution of contaminants.
2. Understand the vertical distribution of contaminants in the FPL and how they change over time.
3. Characterize the thermodynamic and kinetic controls of metal removal during water treatment.

Figure 1.1 Political map of the Yukon showing boundaries, populated places with black dots, water bodies in blue, and main roads with red lines. The location of the Faro Mine Complex is magnified to show additional details. (Adapted from Natural Resources Canada, 2006)

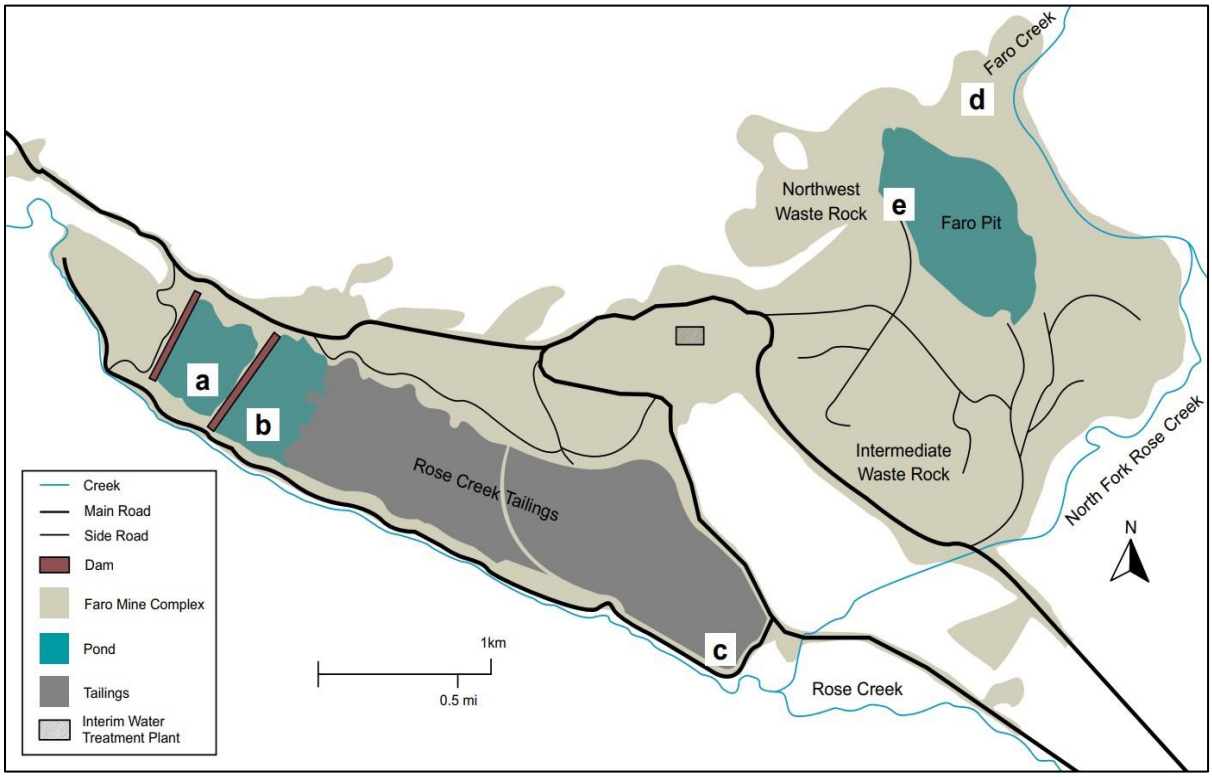

Figure 1.2 Map of the FMC with relevant sites highlighted with letters. The sites are: a. Cross Valley Pond (CVP), b. Intermediate Pond (IP), c. Rose Creek Diversion, d. Faro Creek Diversion, e. Faro Pit pumping station for the water treatment plant (Photo modified from CH2M 2013).

Chapter 2:

Stratification, Solubility Controls, and Sources of Dissolved Contaminant at the Faro Pit lake: Field Characterization and Mass Balance Calculations

2.1 Introduction

Pit lakes are formed following closure of surface mining operations. If the excavations reach a depth below the water table the open pit will fill with water unless the pit is backfilled or continually dewatered (Castendyk et al. 2015). The physical and geochemical characteristics of pit lakes differ from most natural lakes. Open pits are usually relatively narrow and deep excavations. When they are filled with water, the circulation of water and the ingress of oxygen is limited (Miller et al. 1996). The concentration and distribution of constituents is also affected by the geochemistry of input loads. Water that is discharged into a pit lake is often affected by sulfide oxidation products, generated in the surrounding mine waste (Moncur et al. 2006). Acidity inputs and leaching of metals into the pit, coupled by evapo-concentration in pit lakes can lead to the progressive accumulation of dissolved metal(loid)s. Additional acidity can be generated in a pit lake when Fe(II) from anoxic groundwater is discharged into surface water, oxidizes and precipitates as amorphous ferric oxide through reaction 1.2 and 1.3, and when a low pH in a pit leads to subaqueous pyrite oxidation (Gammons and Duaime, 2006).

Vertical circulation of the water within a pit lake is controlled by heat exchange with the atmosphere and vertical distribution of dissolved solids. Seasonal temperature variations cause periods of stagnation and circulation in sufficiently large lakes in most climate zones (Pieters and Lawrence 2009). While the surface layers of a lake are in thermal contact with the atmosphere, deeper layers are isolated from heat propagation (Pieters and Lawrence 2014). The limited kinetic energy reaching deeper into the lake causes temperature stratification of the lake (Castendyk et al. 2015). Similarly, a pit lake may also be stratified by differences in buoyancy due to density contrasts in salinity, between the pit-lake water and surface-water and groundwater inputs to the open pit (Boehrer and Schultze 2008).

The energy that stratifies or mixes pit lakes is derived from the heat and mass exchanges with the surroundings. Stratification is driven by differential mass and heat exchange, throughout the depth of the lakes (Livingstone and Imboden, 1989). Mass and heat inputs into the pit include: groundwater inflow, solar short-wave radiation, atmospheric long-wave radiation, and direct precipitation. Mass and heat losses include evaporative latent heat loss; and conductive heat (Castendyk et al. 2015). In an operational mine setting, there are often inputs and outputs associated with water management activities, including pumping from seepage capture systems and treatment and dewatering operations. De-stratification is driven by wind drag on the water surface, sudden turbulent inflows, and convective turnover. The relative impact of each of these factors determines the presence and depth of the vertical stratification in a pit lake.

Management and prediction of the quality and quantity of contaminated water generated from the different mine components is complex. Load-balance models provide numerical representations of storage and flows of contaminants and water, based on the law of conservation of mass (Usher et al. 2010). Inverse modelling of a geochemical system can be performed for the mass-balance of phases along the water flow paths from known minerology or water chemistry (Nordstrom and Campbell 2014). This study integrates existing load-balance models with field data collected at the Faro site. Inverse modelling of the water quality from waste rock and tailings is integrated with characterization of the water reservoirs at the FMC. The objective of this task is to characterize the contaminant input source terms for the water treatment process, including the temporal changes. The model integrated water and load balances with a representation of the hydrological response of the waste rock, water moved by pumps, and inputs from the tailings reservoir.

2.2 Methodology

2.2.1 Pit Lake Sampling Apparatus

A sampling apparatus was installed into the FPL on two occasions, September 2019 and September 2021. In September 2019, the Faro Pit 1 (FP1) sampler was installed to collect depth-discrete water samples to understand the geochemistry, stratification, and

vertical distribution of dissolved contaminants within the pit. The FP1 sampler was deployed in the SW corner of the pit extending from the ramp used for intake pipe for the water treatment plant (Figure 2.1). The FP1 sampler was constructed using ¼" natural nylon tubing, tied together as a bundle to a stainless-steel cable. Each tube in the bundle ended at a discrete depth within the pit and extended horizontally to shore, where it was connected to a sampling manifold (Figure 2.2). The FP1 sample bundle extended along surface of the pit lake with evenly spaced buoys and was anchored to the bottom of the pit with a heavy weight attached to the cable. The sampler allowed for the collection of water samples from precise depths within the pit, while providing a safe access point away from the shore of the FPL. A peristaltic pump (Geotech Geopump Series I) was used to purge the Faro Pit sampler, collect water samples for laboratory and in-field analysis. Samples were collected from 16 ports, sampling every 2.5 m for the first 20 m of depth and every 10 m for the remaining 30 m depth (Table 5).

The Faro Pit 2 (FP2) sampler, was installed into the FPL in September, 2021. The FP2 sampler was installed to replace the FP1 sampler, which was damaged as a result of two winters in the pit-lake during the COVID-19 pandemic when site access was limited. The FP2 sampler was deployed in the SW corner of the pit, close to the location of the 2019 FP1 sampler installation (Figure 2.1). The design and sampling methodology of the FP2 sampler was similar to the FP1 sampler, with the exception that sampling ports depths were altered to provide more sample points near the chemocline identified in 2019 (Figure 2.3).

Water samples and measurements were also collected from the FMC ponds and seeps. Surface water sample collection was scheduled from the two ponds in the tailings area, two seeps daylighting from the waste rock, and the treatment plant.

2.2.2 Depth Profile Temperature

The FP2 sampler included a 24 AWG thermistor cable that extended across the surface of pit-lake and extended to a depth of 25 m in the pit. Thermistor beads (10K3A1I SERIES II) were placed at 2.5 m intervals to assess the thermal stratification of the pit lake

(Figure 2.3). Resistance measurements from the thermistor cable were transformed to temperature values using the Steinhart-Hart equation (Steinhart and Hart, 1968):

$$T = \frac{1}{A + B\ ln(R) + C\ [\ln(R)]^3}$$

where: T is temperature in Kelvin and R is the resistance in Ohms. A, B, C are coefficients; A= 0.001129, B= 0.000234, C = 8.78E-08 (Campbell Scientific, 2014)

2.2.3 Analytical Techniques

Water extracted from each sample port was pumped through a flow-through cell that held an Orion 9107BN Triode pH probe and a Thermo Scientific Orion 9678BNWP redox potential probe. The pH and redox potential probes were connected to a Thermo Orion 3-Star Portable pH meter and an Orion Star A321 portable Meter respectively, and calibrated daily. Alkalinity was determined using a digital titrator (HACH model 1690001), with a bromocresol green/methyl red indicators. Turbidity was measured on pit water samples using a turbidimeter (HACH 2100P). Dissolved oxygen (DO) was measured as soon as the water was obtained from a sampling manifold with a DO indigo carmine method test kit (CHEMets ASTM D 888-87), which was compared against a visual comparator standard. A field spectrophotometer (HACH DR/2400) was used to measure concentrations of H_2S, NH_3, and PO_4^{3-}. Concentrations of H_2S in the pit water were measured at the time of water collection with the methylene blue spectrophotometry method (Fogo and Popowsky 1949). Concentrations of ammonia and phosphate were measured in the field using the salicylate and orthophosphate methods, respectively (Patton and Crouch 1977; Webb 1992).

2.2.4 Water Chemistry

Samples from the surface, process, and seep water were collected and analyzed to determine the concentrations of dissolved anions and cations. All samples were filtered through cellulose acetate syringe 0.45 μm filters. Samples were stored at 4 ºC for transport and prior to analysis. Dissolved-metal samples were acidified to pH<2 with concentrated nitric acid to limit precipitation during transport and storage. Cations were analyzed at the

University of Waterloo Trace Metal Clean Room by inductively-coupled plasma optical emission spectroscopy (ICP-OES; Thermo iCAP 6500 Duo) and inductively coupled plasma mass spectrometry (ICP-MS; Thermo XSeries 2). Samples collected for anion analysis were filtered using cellulose acetate syringe 0.45 μm filters. Anion concentrations were determined by ion chromatography (IC; Dionex ICS-3000).

2.2.5 Load Balance Calculations

A load-balance model was developed to simulate flow of water and transport of contaminants to and from the FPL. Mass balance calculations were used to couple contaminant generation from mine waste with hydrological inputs and outputs from the local watershed of the FPL. The model integrated active pumping inputs and outputs managed by the mine operators, including seasonal withdrawals for water treatment and inputs from contaminated-water capture systems and supernatant water from the tailings facilities.

The GoldSim platform was used to model the Faro Mine water balance (GoldSim Technology Group 2018). GoldSim is a flexible general-purpose simulation program for complex engineering and environmental systems. The GoldSim software can be used to develop dynamic and probabilistic models, with object-oriented elements that represent: data, equations, logic, processes, or events.

Water quality, hydrology, and flow data from multiple data sources was integrated in a water and load balance model. The main model input for water into the system is a stochastic element to represent the precipitation over the study site, based on the historical precipitation record at the site. To calculate the waste rock drainage rate, the model has a simple hydrological response based on the available seep flow records, evaporation calculations, and infiltration estimates. The dissolved metal loading rate from tailings and waste rock was calculated by extrapolating the seasonal load and flow trends from the records of representative seepage sampling points. The seepage water and contaminant load were coupled to a PHREEQC mixing model to calculate the concentration of dissolved species after mixing with surface waters. The dynamic water level and concentrations of

dissolved species at the FPL was simulated by integrating the flowing or pumped water-sources and outputs.

The operational water balance was based on site schedules and operational decisions, with enough flexibility for changes in the management of the site. The main elements of the operational water balance were the volumes of water pumped from: i) tailing ponds, ii) seep capture systems, and iii) the water treatment plant. The model relies on the Monte Carlo approach to propagate the uncertainty associated with the assumptions of the hydrological and geochemical inputs. The model results were expressed as a probability distribution that quantitatively represents the possible model outcomes.

2.3 Results

2.3.1 Field measurements – September 2019

Profiled water quality results were obtained between the depths of 0 and 47 m from the FPL in September 2019 (Figures 5, 6). The water chemistry of the FPL was vertically stratified with multiple parameters changing sharply at a well-defined thermocline between 8 m and 10 m depth. The stratification was caused by the difference in specific density of water at 10 ºC and 4 ºC, in the epilimnion and hypolimnion respectively. The water temperature below the thermocline was ~4 ºC, which is the temperature of maximum density of pure water. The density of the water, as calculated by the Steinhart-Hart equation, was lower in the epilimnion (μ=1000.6 kg m^{-3}, SD=0.2, n=4), than in the hypolimnion (μ=1001.1 kg m^{-3}, SD=0.1, n=10). The metalimnion, the layer defined by a sharp change in temperature, is a narrow layer between 8 m and 10 m depth. Some parameters change at the top of the thermocline, some change below it.

An inflection point in the TDS measurements was observed at 8 m depth, corresponding to the top of the thermocline. The stratification was clearly defined by other parameters (Figure 2.4). The TDS values in the epilimnion ranged between 1067.50 and 1085.00 mg L^{-1} (μ=1075.9, SD=8.1, n=5), and TDS measurements in the hypolimnion were between 1120.0 to 1159.9 mg L^{-1} (μ=1135.4, SD=12.5, n=9).

In 2019, the pH of FPL waters was circumneutral at all the sampled depths. The pH distribution was stratified, with a marked increase at the bottom of the thermocline (10 m depth; Figure 6). In the epilimnion, the pH values ranged from 6.58 to 6.79 (μ=6.7, SD=0.1, n=5). In the hypolimnion the pH ranged from 6.1 to 6.4 (μ=6.2, SD=0.1, n=9), the pH increased to 6.48 below a depth of 27.5 m. The pH of the FPL waters was within the defined *tolerable* threshold of pH between 6.0 and 9.5, set by the Metal and Diamond Mining Effluent Regulation guidelines (MDMER).

The water in the pit lake was slightly oxidizing, throughout the sampled depth. There was no clear stratified trend in the Eh measurements (Figure 2.4). In the epilimnion, Eh measurements ranged from 376 to 398 mV (μ=389, SD=9, n=4). In the hypolimnion, Eh measurements ranged from 361 to 389 mV (μ=375, SD=9, n=10).

2.3.2 Water Chemistry – September 2019

The concentration of SO_4 in the FPL above the thermocline ranged from 912 to 937 mg L^{-1} (μ=924, SD=8.8). The concentration of SO_4 increased gradually downwards to the bottom of the pit (Figure 2.3). The concentration of SO_4 in the hypolimnion ranged from 965 to 1015 mg L^{-1} (μ=987, SD=19). Concentration of dissolved Mn showed a similar vertical trend to SO_4, with concentrations between 9.5 and 9.8 mg L^{-1} (μ=9.7, SD=0.1) within the epilimnion, and increased to between 9.9 to 10.1 mg L^{-1} (μ=10.0, SD=0.1) below the thermocline.

The dissolved concentrations of Ca and Mg exhibited similar slightly stratified profiles in the FPL to that of SO_4 and Mn. The concentration of Ca in the FPL ranged from 192.5 to 221.5 mg L^{-1} (μ=208.8, SD=9.2) (Figure 2.3). The concentration of Mg was ~45% lower than the concentrations of Ca. The concentration of Mg ranged throughout the pit lake from 107.9 to 124.8 mg L^{-1} (μ=117.5, SD=5.9).

The concentrations of transition metals Zn, Fe, and Ni were stratified in the pit lake. The concentrations exhibited a sharp increase at the thermocline (10 m depth). The concentrations of Fe, Ni and Zn continued to increase gradually to the bottom of the pit lake (Figure 2.3). In the epilimnion the concentration of Zn were lower than in the hypolimnion,

ranging from 30.5 to 30.9 mg L^{-1} (μ=30.8, SD=0.2, n=5). In the hypolimnion, the concentration of Zn ranged from 32.5 to 33.5 mg L^{-1} (μ=32.9, SD=0.3, n=9). All the measured concentrations of Zn exceeded the MDMER grab sample concentration of 0.8 mg L^{-1}. The concentrations of Fe had the greatest difference in magnitude across the thermocline, the values in the epilimnion were 22 times lower than in the hypolimnion. In the epilimnion, the concentration of Fe ranged from 0.05 to 0.24 mg L^{-1} (μ=0.1, SD=0.1, n=5). Concentration of Fe in the hypolimnion ranged from 1.8 to 2.7 mg L^{-1} (μ=2.2, SD=0.3, n=9). Concentration of Ni in the pit-lake epilimnion ranged from 170.6 to 172.9 μg L^{-1} (μ=171.7, SD=1.1, n=5). Concentration of Ni below the thermocline ranged from 185.0 to 196.3 μg L^{-1} (μ=190.7, SD=4.0, n=9). All concentrations of Ni measured in the FPL were more than 2 orders of magnitude greater than the MDMER limit of 0.5 μg L^{-1}.

The concentrations of Cd in the FPL also were stratified. There was a sharp decrease at 10 m, which is consistent with the temperature depth distribution (Figure 2.3). The trend of Cd concentration in the FPL profile differed from other described parameters because dissolved concentrations were slightly higher above the thermocline (μ=13.6, SD=0.4, n=5) than below it (μ=12.3, SD=0.2, n=9).

Saturation index analysis indicates that the FPL water was undersaturated with respect to Al phases within the epilimnion, including gibbsite (γ-$Al(OH)_3$) and basaluminite ($Al_4(OH)_{10}\cdot 4H_2O$) . Conditions shifted at the thermocline and water within the hypolimnion was supersaturated with respect to K-jarosite ($KFe_3(SO_4)_2(OH)_6$) and alunite ($KAl_3(SO_4)_2(OH)_6$) (Figure 2.5). The pit-lake water was also supersaturated with respect to iron oxides, hydroxides, and oxyhydroxide throughout the surveyed depth, including amorphous $Fe(OH)_3$, goethite (α-FeO(OH)), magnetite ($Fe^{2+}Fe^{3+}{}_2O_4$), and hematite (α-Fe_2O_3).

2.3.3 Field Measurements – September 2021

In September 2021, a second set of samples from the FPL were collected (Figures 8, 9). The results from *in situ* geochemical tests, cation, and anion analyses from profile samples were obtained between depths of 0 m and 25 m. The pit was vertically stratified with

a well-marked thermocline at 7.5 m. The temperature of the top 7.5 m was between 10.85 to 11.08 ºC (μ=11.0, SD=0.1, n=3), after a sharp transition the temperature was 3.8 ºC (SD=0.20, n=8) down to the bottom of the pond. Nine temperature measurements were taken from the installed thermistor over three days (Figure 2.8). The temperature measurements at each depth were similar within the three-day period. However, the depth of the thermocline varied between 3 m and 10 m. Water density calculations in the FPL showed clear contrast at the thermocline. The water density of the epilimnion was between 1000.76 to 1000.82 kg m^{-3} (μ=1000.79, SD=0.2, n=3). In the hypolimnion, the water density was between 1001.16 to 1001.26 kg m^{-3} (μ=1001.21, SD=0.03. n=8).

The profile of the pH measurements at the pit-lake was also stratified, with a pH of 4.0 (SD=0.1, n=3) within the epilimnion, and a higher pH of 5.8 (SD=0.04, n=8) in the hypolimnion (Figure 2.6). The mean pH of the FPL was outside of the *tolerable* range of pH, between pH 6.0 and 9.5, set by MDMER guidelines.

Total dissolved solid values in the epilimnion was 8% higher than in the hypolimnion. The TDS in the epilimnion ranged between 1365.0 and 1435.0 mg L^{-1} (μ=1404.2, SD=33.1, n=3) (Figure 2.6). The TDS in the hypolimnion ranged from 1365.0 to 1379.0 mg L^{-1} (μ=1374.3, SD=5.72, n=8). The dissolved oxygen (DO) and the water turbidity varied little throughout the pit-lake depth, with slightly higher values above the thermocline. The DO concentration corresponds to suboxic conditions μ=4.3 mg L^{-1} (SD=0.9, n=11) in the pit lake. The average turbidity was 4.2 NTU (SD=0.4).

2.3.4 Water Chemistry – September 2021

The concentration of SO_4 in the FPL in the epilimnion ranged from 1189.71 to 1199.51 mg L^{-1} (μ=1194.4, SD=4.9, n=3) and decreased by 5% in the metalimnion relative to the hypolimnion. The concentration of SO_4 in the hypolimnion were lower and more variable, with values between 1102.2 to 1142.4 mg L^{-1} (μ=1125.7, SD=15.4, n=8).

Concentrations of Zn in the epilimnion were higher than in the hypolimnion. The Zn concentrations in the epilimnion ranged from 35.62 to 35.92 mg L^{-1} (μ=35.7, SD=0.2, n=3), and decreased sharply at the thermocline (Figure 2.7). Concentration of Zn in the

hypolimnion ranged from 32.6 to 34.7 mg L^{-1} (μ=33.3, SD=0.6, n=8). All the Zn concentrations measured in the pit lake exceed the MDMER grab sample threshold of 0.8 mg L^{-1}. Concentrations of Fe were also sharply stratified, the concentrations in the epilimnion were 8.8 times higher than in the hypolimnion. Concentration of Fe in the epilimnion were between 4.36 and 4.45 mg L^{-1} (μ=4.4, SD=0.05, n=3). Concentration of Fe in the hypolimnion were between 0.48 and 0.54 mg L^{-1} (μ=0.5, SD=0.02, n=7). The Mn showed a similar vertical trend as Fe, with concentrations between 17.66 to 17.79 mg L^{-1} (μ=17.7, SD=0.1, n=3) at the epilimnion. Concentration of Mn below the thermocline were between 14.8 to 16.3 mg L^{-1} (μ=15.2, SD=0.4, n=8).

The concentrations of Pb, Cd, and Cu in the FPL exhibited similar vertical trends to each other and were higher in the epilimnion, and decreased between 5 m and 10 m depth (Figure 2.7) to lower concentrations in the hypolimnion. The concentration of these metals in the metalimnion were intermediate between the mean concentrations of the epilimnion and hypolimnion. Concentrations of Pb in the epilimnion range between 59.97 to 61.82 μg L^{-1} (μ=60.9, SD=0.93, n=3). Concentration of Pb in the hypolimnion ranged from 2.38 to 3.13 μg L^{-1} (μ=2.8, SD=0.24, n=7). Concentrations of Pb in the epilimnion of the pit lake were 22 times higher than in the hypolimnion. None of the Pb concentrations measured in the pit lake exceeded the MDMER grab sample threshold of 0.16 mg L^{-1}. The mean Cd concentration in the epilimnion was 19.6 μg L^{-1} (SD=0.4, n=3) and in the hypolimnion the mean concentration was 14.8 μg L^{-1} (SD=0.2, n=7). Concentrations of Cu in the epilimnion of the pit lake were 5 times higher than in the hypolimnion. The mean Cu concentration in the epilimnion was 71.4 μg L^{-1} (SD=1.2, n=3), and the concentration in the hypolimnion was 14.1 μg L^{-1} (SD=0.4, n=7)

The distribution of Ni in the FPL was different from other metals. The concentrations of Ni in the epilimnion (μ=170.3 μg L^{-1}, SD=2.0, n=3) were lower than the concentrations in the hypolimnion (μ=187.43 μg L^{-1}, SD=2.3, n=8) (Figure 2.7). All the concentrations of Ni measured in the FPL were more than 2 orders of magnitude greater than the MDMER guideline value of 0.5 μg L^{-1}.

The vertical distribution of Ca and Mg differ from each other in the FPL. The concentration of Ca (μ=250.7 mg L^{-1}, SD=0.3, n=3) were higher in the epilimnion than in the hypolimnion (μ=241.3 mg L^{-1}, SD=2.4, n=8) (Figure 2.7). For concentrations of Mg the relative trend was reversed. The concentrations of Mg in the epilimnion (μ=127.8 mg L^{-1}, SD=0.3, n=3) were lower than in the hypolimnion (μ=129.1 mg L^{-1}, SD=1.0, n=8).

2.3.5 Input Loads

The FPL serves as storage for multiple mine impacted water streams that originate in the FMC (Figure 2.9). Each year 50,000 m^3 of groundwater from the S-Wells capture system are pumped into the Faro Pit (Figure 2.10). Total discharge from the S-Wells each year did not change by more than ±30% between 2018 and 2020. Discharge increased by 160% in 2021 which corresponds to an increase of 130,000 m^3. The concentration of dissolved species in the S-Wells remained constant between 2018 and 2021, with a decrease in concentration in all species at the start of 2021 (Figure 2.11). The concentrations of Fe range between 10 and 20 mg L^{-1}, the concentrations of Zn ranged between 250 and 1000 mg L^{-1}, the concentration of Cd mostly remained between 0.4 and 0.7 mg L^{-1}. The water from the S-Wells was a small load contributor of Fe, Mn, and SO_4 to the FPL but it accounted for 33% of the Cd and Ni load in 2018 and 2019. Although the flow from the S-Wells increased in 2021, the overall load decreased due to lower concentration of dissolved species. The backfilled Zone 2 pit capture system was pumped year-round, at a total volume of 40,000 to 75,000 m^3 yr^{-1}. The input from the Zone 2 capture system represented a small load of all dissolved species into the Faro Pit, except for Ni. Before 2020, Zone 2 contributed 15% of the total Ni load into the FPL.

The volume of effluent pumped from the IP to the Faro Pit vary from year to year: 0.15M m^3 in 2018, 1.7M m^3 in 2019, 4.2M m^3 in 2020, and 3.7M m^3 in 2021 (Figure 2.10). The concentration of dissolved species fluctuated in a seasonal pattern. The concentrations of Fe fluctuated between 10 and 200 mg L^{-1}, with lower concentrations in the summer (Figure 2.11). Concentrations of dissolved Mn exhibited a similar seasonal variation pattern with concentrations between 16 and 45 mg L^{-1}. The concentrations of Zn and Cd increased 50%

during the second half of 2021, and increased up to 75 and 33 mg L^{-1} respectively. The pH in the IP remained at 6.4, except for two occasions, in 2018 and 2021, when the pH decreased to 4.0 and 3.8 respectively. The cumulative load from the IP was the first or second most important load input to the FPL for all dissolved species (Figure 2.12). The Fe load into the pit lake was between 100 and 200 T yr^{-1} between the years 2018 and 2019, and then increased to 400 T yr^{-1} in 2020 and 2021. After the year 2020 the Fe loads to the pit doubled, mainly due by additional IP load into the pit lake. In a similar way, the Mn annual load to the pit lake increased from 70 T yr^{-1} in 2018 and 2020, to 150 T yr^{-1} in 2020 and 2021. The observed increase in overall Mn was almost exclusively driven by the increased load from the IP.

The groundwater discharge that percolates through the waste rock surrounding the Faro Pit is an additional source of contaminant loading into the FPL. Each year between 37,000 and 120,000 m^3 yr^{-1} of mine impacted water flows into the Faro Pit from surrounding waste rock and mine waste (Figure 2.10). The concentrations of dissolved species in the waste-rock effluent have increased since the year 2000, with a sharper increase after February 2020. The average concentration of Fe from the waste rock seepage was 650 mg L^{-1} between 2018 and 2020 (Figure 2.11). Between 2020 and 2021, the concentrations rose steadily to 1500 mg L^{-1}. Similarly, concentrations of Zn between 2020 and 2021 doubled compared to the 2018-2020 period, from 1.1 g L^{-1} to 2.1 g L^{-1}. The pH from the waste rock seepage mostly fluctuated between 6.0 and 6.2. In 2021, but there was one pH measurement of 4.0 in May 2021. The cumulative load from the waste rock was one of the largest inputs to the FPL after the contribution from the IP (Figure 2.12). Each year, 205 T of Zn, 110 T of Fe, 98 kg of Cd, 400 kg of Ni were transported from the waste rock to the FPL in the mine impacted drainage.

The seepage rate from the foot of the Intermediate waste rock dump at the X23 monitoring station was variable from year to year. Between 2014 and 2020, the cumulative annual discharged range from 15,000 to 45,000 m^3 yr^{-1} (Figure 2.13). There was a weak correlation observed between annual precipitation and cumulative discharge (R^2= 0.26). The highest precipitation year, 2017, corresponded to the highest discharge year. The lowest

precipitation year corresponded to the lowest discharge year. The discharge and precipitation values in 2015 diverged from the linear correlation relationship, and when discounting the 2015 values as an outlier, the correlation was improved (R^2= 0.71). The correlation reflects the change in seepage rate as a result of the increased hydraulic loading at the top of the pile from precipitation, not the movement of water through the full depth of the pile.

2.4 Discussion

2.4.1 *In Situ* Parameter Distribution

The FPL was thermally stratified, with the thermocline at around 10 m depth. The stratification is caused by the difference in specific density of water at 10 ºC and 4 ºC, in the epilimnion and hypolimnion respectively. In 2021, the average density of the water in the epilimnion was 1000.8 kg m^{-3} (1000.76-1000.8 kg m^{-3}) compared to an average density of 1001.21 kg m^{-3} (1001.16 - 1001.26 kg m^{-3}) in the hypolimnion (Figure 2.6). Pure water is most dense at 4 ºC, therefore as the surficial water cools to 4º C it settles at the bottom of the pond. The thermally stratified pit lake is divided by a sharp thermocline, which limits the water and dissolved element exchange between the epilimnion and hypolimnion. The depth of the thermocline fluctuates between 8 m and 10 m, but the thermocline remains sharp (Figure 2.8). Fluctuations on the depth of the thermocline are likely driven by internal waves, caused by wind action on the pit-lake surface (Stevens and Lawrence 2003). The electrical conductivity (EC), and the calculated TDS, show sharp boundary at the same depth as the thermocline (Figure 2.14). There was limited mixing between the epilimnion and hypolimnion at the time of sampling, i.e. water present in the epilimnion or hypolimnion remained in that layer when the density stratification was present. In 2019, the epilimnion had lower TDS than the hypolimnion. In 2021, a higher volume of water with higher TDS was pumped to the surface of the FPL. The high TDS water remained in the epilimnion in 2021, which reversed the trend from previous years when the epilimnion had higher TDS (SRK, 2020).

Between 2004 and 2008, separate measurements and sampling was conducted in the fall at the location where the FPL is deepest. The vertical trend of EC showed that there were

three distinct zones of stratification in the pit lake with sharp boundaries at 10 m and 20 m (Pieters and Lawrence, 2014). The EC inflection point at 10 m depth corresponds to the location of the thermocline, as observed in subsequent surveys. The deeper EC inflection point likely corresponds to a chemocline, with higher salinity water at the bottom of the pit and lower salinity in the shallower portion of the pit lake (Moncur et al. 2006). Strong salinity stratification in pit lakes can prevent the complete mixing of the water column (Pieters and Rogers, 2014). Lakes that do not undergo mixing are classified as meromictic. In the surveys conducted in 2019 and 2021, there was no evidence of a chemocline at the surveyed depths. In 2021, despite having water with higher TDS at epilimnion, the density difference caused by the temperature of the water was sufficient to maintain the stratification of the pit lake.

The EC values from 2019 are similar to those measured as part of a separate FPL survey, found to be ~5% higher (SRK, 2020). The recorded EC values of the comparable SRK study in 2019 showed a sharp increase around depth 10 m, same depth as the thermocline observed by this study, but the reported EC in the deep hypolimnion is higher.

The stratification observed in the fall of 2019 and 2021 did not persist throughout the year. The FPL TDS profile from March 2019, when the pit was still covered in ice, was uniform throughout the depth of the pit (SRK, 2020). The TDS profile was uniform except for a thin layer of fresh water characterized by relatively lower TDS that remained close to the water-ice interface. There was likely a mixing event in the late fall or early winter, which classifies the FPL as a dimictic water body.

The pit-lake pH remained in a narrow circumneutral range in 2019, with a small decrease in pH (<0.5 SU) below the thermocline. In September 2021, the pH was acidic at the surface, with a pH of 4 within the epilimnion (Figure 2.14). Below the thermocline, the pH in the hypolimnion was acidic to near-neutral with an average pH of 5.77 (range 5.68 - 5.83 SU). The spatial trend of pH corresponded to the thermal stratification of the pit lake. The lower pH in the epilimnion was not observed in any of the previous surveys. Prior to 2021, the pH in the epilimnion remained circumneutral and higher than the pH in the hypolimnion.

In the fall of 2019, the pit-lake water was slightly oxidizing with a temperature corrected Eh between 380 mV and 400 mV (Figure 2.4). In 2021, dissolved oxygen (DO) was measured from the water samples. The pit lake remained suboxic with DO concentrations between 3 mg L^{-1} and 6 mg L^{-1} (Figure 2.6). These observations also suggest that the stratification of the pit lake limited the abundance of DO in the deeper pit lake, as the concentrations of dissolved oxygen decreased in the hypolimnion.

2.4.2 Water Chemistry Distribution

Dissolved SO_4 was the principal anion in all water samples collected from the FPL. Sulfide minerals, such as pyrite, galena, sphalerite, chalcopyrite, pyrrhotite, and tetrahedrite, are widely distributed on the pit walls and in the surrounding waste rock (Pigage, 1991, Bao et al. 2020). Oxidation of sulfide minerals results in the release of SO_4, metals, and metalloids into the influent water (Blowes et al., 2014; Evangelou & Zhang, 1995). The pit water was slightly undersaturated with respect to gypsum and $Zn_4(OH)_6SO_4$ (Figure 2.5). There was no detectable presence of dissolved H_2S in the sampled water, likely due to the oxidizing conditions in the pit lake. The identity of S in solution was predominantly SO_4 species, as evidenced from speciation calculations. The abundant SO_4 in solution could lead to the precipitation of secondary minerals like barite, alunite, and K-jarosite.

The most abundant cations in all the water samples collected from the pit lake are Ca and Mg. The source of Ca and Mg in solution was the acidic drainage neutralizing reactions, mainly the dissolution of carbonate minerals present in the surrounding waste rock (Jurjovec et al. 2002). Calcite and dolomite are the main carbonate minerals in the upper benches of the waste rock surrounding the Faro Pit (Bao et al. 2020). The dissolved concentration of Ca was likely controlled by equilibrium with respect to gypsum, as the water samples were saturated or near saturation with respect to gypsum. The pit water did not approach saturation with respect to any minerals likely to remove Mg from solution (Figure 2.5). Both the Ca and Mg concentrations increased between 2019 and 2021 throughout the depth of the pit lake (Figure 2.15). The vertical distribution of Ca and Mg in the pit lake was not clearly influenced by the thermal stratification like other parameters.

In 2019, concentration of total Fe was higher in the hypolimnion than in the epilimnion, whereas the concentration of total Fe was higher in the epilimnion in 2021, reflecting the composition of water pumped onto the surface of the pit lake (Figure 2.15). In 2021, the lower pH of the epilimnion influenced the Fe speciation, 12% of the Fe was present as Fe(II) (Figure 2.6). Concentration of total Fe in the hypolimnion was less than 50 µg L^{-1} of Fe(II), where Fe was mainly present as Fe(III). The saturation index analysis showed that the pit lake was saturated with respect to iron oxide and hydroxide phases including goethite and $Fe(OH)_3$ throughout the entire depth (Figure 2.5). The presence of turbidity in the pit lake (3.88 - 5.11 NTU) was likely related to the presence of ferric (oxy)hydroxides precipitates in the water column (Figure 2.14). Amorphous ferric iron (oxy)hydroxides are likely to precipitate under the conditions prevalent in the pit lake, and form low-density flocs that remained suspended in the water column causing turbidity, consistent with the vertical profile of turbidity and dissolved Fe.

The elevated concentrations of Zn and Mn are indicative of the deterioration of the water quality. The FPL water was saturated with respect to Mn and Zn carbonates ($MnCO_3$, $ZnCO_3$; Figure 7). These phases, or less crystalline precursors, could control the aqueous concentrations in combination with sorption onto iron oxides or oxyhydroxides (Farley, 1985). The concentrations of Zn and Mn changed sharply at the well-defined thermocline at 10 m depth in 2019 and 7.5 m depth in 2021 (Figure 2.14). The thermal stratification was strong enough to maintain distinct concentration zones separated by a thin thermocline layer. In 2019, the Zn concentrations were higher in the hypolimnion, the Mn concentrations were uniform throughout the pit depth (Figure 2.15). In 2021, both the Mn and Zn concentrations were higher in the epilimnion. The density gradient was an effective barrier against the mixing of the contaminants of concern flowing into the FPL.

The concentrations of Pb and Cd both increased between 2019 and 2021. Particularly in the epilimnion, the concentrations of these metals were higher in the in 2021. The vertical trend of higher concentrations in the epilimnion compared to the hypolimnion was maintained, but this pattern became more pronounced in 2021 (Figure 2.15). The Pb concentrations in the epilimnion increased by two orders of magnitude between 2019 to

2021. The concentrations of Cd in the pit-lake epilimnion were 70% higher in 2021 compared to 2019. Although the concentrations of Pb remain below the MDMER grab sample threshold of 0.16 mg L^{-1}, it could become a contaminant of concern that requires a high-pH treatment to maintain acceptable Pb concentrations (Figure 3.4). Treatment of Pb and Cd requires the treatment system to reach a pH of 10 (Chermak et al. 2004). To achieve the target pH of 10 the amount of neutralizing base input into the treatment base would have to increase between 50% and 100% (Figure 3.2).

Concentrations of Ni remained constant between 2019 and 2021. The concentration distributions were similar except for the depth of the thermocline that separates lower concentrations in the epilimnion (μ=170.3 μg L^{-1}, SD=2.0) than in the hypolimnion (μ=187.43 μg L^{-1}, SD=2.3; Figure 12). The depth of stratification is different between 2019 and 2021, which is consistent with the relative density plots (Figure 2.14).

2.4.3 Pit-lake Load Balance

Chemical differences between the epilimnion and the hypolimnion can be caused by warm water inputs into the surface of the pit, causing accumulation of dissolved species and acidity (Sánchez España et al. 2008). Multiple mine-impacted water-capture and pumping systems discharge into the Faro Pit for storage and mixing (Figure 2.9). The main inputs into FPL are the Zone 2 backfilled pit pumping system, S-wells groundwater capture system, supernatant tailings water accumulated at the IP, and drainage from waste rock surrounding the Faro Pit. The S-Wells discharge increased from 50,000 m^3 yr^{-1} from 2018 to 2020, up to 130,000 m^3 yr^{-1} in 2021. The Zone 2 discharge ranged from 40,000 to 75,000 m^3 yr^{-1}. The discharge from the IP in 2018 was 0.15M m^3 yr^{-1} and in 2019 was 1.7M m^3 yr^{-1}, in 2020 was 4.2M m^3 yr^{-1}, and in 2021 was 3.7M m^3 yr^{-1}. The discharge from the surrounding waste rock was between 37,000 and 120,000 m^3 yr^{-1} between 2018 and 2021 (Figure 2.10).

The water with the highest concentrations of dissolved metals was derived from the surrounding waste rock seepage followed by the S-Wells groundwater. The Fe concentration from the waste rock ranged from 650 mg L^{-1} and 1500 mg L^{-1}; and the Zn concentrations ranged from 1.1 g L^{-1} to 2.1 g L^{-1} (Figure 2.11). The Fe concentrations in the S-Wells ranged

between 10 and 20 mg L^{-1}, the Zn concentrations ranged between 1000 and 250 mg L^{-1}. The dissolved species concentrations in the Zone 2 and IP influent waters were lower. The pH from all sources was between 6 and 7 during most of the study period, except at the start of 2021 the water pH from the waste rock and IP decreased to between 3.8 and 4.0. Lower pH values during this period brought additional acidity to the pit lake, compared to the previous years. The pH in the epilimnion of the pit lake in 2021 was the same as the local minimum pH from the waste rock and IP in the same period.

The concentrations of dissolved species in the waste-rock seepage and IP have increased linearly starting in 2020 and 2021, respectively. Concentrations of Fe and Zn in the waste-rock seepage doubled between the start of 2020 and the end of 2021, and the concentration of Cd increased by an order of magnitude (to 1.5 mg L^{-1} in 2021). The concentrations of Pb, Zn, and Ni in the IP were highly variable, but the annual concentration maxima were 50% to 100% higher in the years 2020 - 2021 compared to 2018 - 2020.

The cumulative load from the waste rock and IP were the largest inputs to the FPL. Between 2020 and the end of 2021 the Fe loads doubled into the pit from 220 T to 450 T, mainly due to an additional load from the IP. Similarly, the annual load of Mn into the pit lake increased from around 60 T yr^{-1} in 2018 and 2020 to 150 T yr^{-1} in 2020 and 2021, mainly from increase of IP contributions to the FPL. The load of Ni, Zn, and Cd also doubled, driven by a combination of loads from the IP, S-Wells, and waste-rock seepage. With the increasing concentrations in the waste-rock effluent from 2020 and additional discharge in 2020 and 2021, the loads from the waste rock increased by a factor of two for Fe, Zn, and Ni and by a factor of four for Cd. The inputs from the Zone 2 capture system represented a small load of all dissolved species into the FPL, except for Ni. Before 2020, Zone 2 contributed 15% of the Ni load into the FPL.

The seepage flow rate from the waste rock is dependent on the precipitation inputs and hydrogeological conditions of a rock pile (Figure 2.13). Between 2014 and 2020, there was a linear correlation between cumulative discharge and annual precipitation (R^2= 0.71), excluding the year 2015. Increased discharge from the foot of the waste rock piles after precipitation or snow melting events is associated with pressure wave propagation through

the pile, which forces the pore-water from the saturated soil matrix (Bao et al. 2020). Increased discharge after a high infiltration event is instantaneous, though the water particles have years-long residence times in the waste rock piles. Generally, lower concentrations of dissolved species were recorded in the summer than in the winter, likely due to the dilution of the seepage water with additional percolation and overland flow from the waste-rock piles. Though, the mass loading from the waste rock was higher during the summer, likely due to dissolution and mobilization of secondary minerals within the pile (Bao et al. 2020).

The degradation of water quality in the epilimnion in 2021 was consistent with the contaminant load balance of the pit lake. The operational loading sources were discharged at or near the surface of the pit lake. The increased pumping volume from the IP caused most of the load increase in 2021, with little effect of the changing water quality from that source. The increase in concentrations from the waste rock, starting in 2020, was also a contributing factor for the degraded water quality in the pit-lake epilimnion. These concentrations increased in a decades-long breakthrough of dissolved species from the oxidizing mine waste at the FMC. As break-through of dissolved species continue to seep from the waste rock, the load will progressively increase.

2.5 Summary and Implications

2.5.1 Summary

The FPL is the largest reservoir of water in the FMC, multiple mine impacted water sources are pumped to the pit lake for storage and mixing. A sampling apparatus was installed into the FPL on two occasions, in September 2019 and September 2021. The results from *in situ* geochemical tests, temperature measurements, cation, and anion analyses from profile samples were obtained down to a depth of 47 m in 2019 and 25 m in 2021. The main vertical trend in the FPL was the thermal stratification; multiple parameters changed sharply at a well-defined thermocline between 8 m and 10 m depth. At the time of sampling, the pit lake was well stratified into an epilimnion down to a depth of 8 m, metalimnion 8 to 10 m, and hypolimnion from 10 m to the bottom of the lake. The stratification was caused by differences in the specific density of water at 10 ºC and 4 ºC. The density of the water was

lower in the epilimnion (μ=1000.6 kg m^{-3}, SD=0.2, n=4), than in the hypolimnion (μ=1001.1 kg m^{-3}, SD=0.1, n=10). The FPL is not stratified year-round, the lake likely turns over in the late fall or early winter. The results from 2019 and 2021 show no indication of a chemocline in the pit lake.

The FPL sampling locations in 2019 and 2021 were overall similar, but the results showed differences in water chemistry profile. The pit-lake pH remained in a narrow circumneutral range in 2019 between 6.58 and 6.79, with a small decrease in pH (<0.5 SU) below the thermocline. In September 2021, the pit lake was acidic at the surface with a pH of 4.0 within the epilimnion. Below the thermocline in 2021, the water was acidic to neutral with a pH of 5.8. Both in 2019 and 2021, the pit lake was slightly oxidizing, with DO values between 3 mg L^{-1} and 6 mg L^{-1}.

There is a sharp boundary in the TDS profile at the same depth as the thermocline. There is limited mixing between the epilimnion and hypolimnion. Water that flowed into the epilimnion or hypolimnion remained in that layer for the duration of the summer. In 2019, the epilimnion had lower TDS than the hypolimnion. In 2021, the epilimnion had higher TDS than the hypolimnion

In 2019 the total Fe concentration was higher in the hypolimnion than in the epilimnion, whereas the total Fe concentration was higher in the epilimnion in 2021. In 2021, due to the lower pH of the epilimnion 12% of the iron on the surface was present as Fe(II). The total Fe concentration in the hypolimnion in 2021 was less than 50 μg L^{-1} of Fe(II) iron, the iron was mainly present as Fe(III).

In 2019 the concentrations of Zn were higher in the hypolimnion, the concentrations of Mn were uniform throughout the pit depth. In 2021, concentrations of both the Mn and Zn were higher in the epilimnion. The density gradient was an effective barrier against the mixing of the contaminants within the pit lake. The concentrations of Pb in the pit-lake epilimnion increased by two orders of magnitude between 2019 to 2021. Concentrations of Cd in the pit-lake epilimnion are 70% higher in 2021 compared to 2019.

The main inputs into the FPL are the Zone 2 pumping system, S-wells groundwater, tailings water from the IP, and drainage from waste rock surrounding the Faro Pit. The volume of water pumped from the IP to the Faro Pit was the largest, up to 4.3M m^3 yr^{-1}. The other sources into the FPL are generally under 120,000 m^3 yr^{-1}.

The water with the highest concentrations of dissolved metal discharged into the Faro Pit was sourced from the surrounding waste-rock seepage and the pumping from the S-Wells groundwater. Concentrations of Fe and Zn in the waste-rock seepage doubled between the start of 2020 and the end of 2021, and the concentration of Cd increased by an order of magnitude. The pH from all sources was between 6 and 7, except at the start of 2021 when the pH of waters sourced from waste rock and IP water decreased to 4.0, the same pH as the FPL epilimnion.

The cumulative load from the waste rock and IP are the largest inputs to the FPL. Between 2020 and the end of 2021, the Fe load doubled due by additional IP load into the pit lake. The annual load of Mn into the pit lake increased by 150% between 2018 and 2020 from additional IP loading. The loads of Ni, Zn, and Cd into the pit doubled, driven by the source waters from the IP, S-Wells, and waste rock seepage. With higher concentrations from the waste rock and additional discharge in 2020 and 2021, the loads from the waste rock increased 2x for Fe, Zn, and Ni and 4x for Cd.

2.5.2 Implications

Results of this study complement the ongoing care and maintenance and closure activities at the FMC. The detailed characterization of the FPL is useful to understand the distribution and concentrations controls of contaminants in a central part of the water-management system. The stratification of the pit lake is likely to occur each year, unless disturbed by excessive pumping to the surface of the pit. The presence of a well-defined epilimnion can be used as a reservoir within the lake. Geochemically distinct water can be selectively stored in the upper layer and separated from the rest of the lake volume by the density gradient. This separation can be beneficial for planning the influent water quality for treatment, based on the blend of water stored in the epilimnion.

The pH of the epilimnion decreased from 6.7 to 4.0 between 2019 and 2021. This change represents a major shift in the geochemistry of the lake and the influent into the water-treatment plant. At lower pH, metals tend to dissolve more readily. Higher solubility may lead to higher concentrations in solution from external inputs and *in situ* oxidation of sulfide minerals. Deteriorating water quality inputs into the pit alter the pit-lake water quality. These processes are likely to continue as the seepage water and stored water in the site becomes more acidic and the concentrations of dissolved metals increase.

Care and maintenance of the FMC requires capturing, pumping, storing, and treating large volumes of mine water. Load-balance calculations are useful when deciding where to store the water prior to treatment, to streamline the treatment process and ensure the safety of the water management infrastructure. The operations team at the FMC can plan and adapt for changes if the load balance and water balance of the site is well monitored and understood.

The characterization of the pit-water quality and load-balance calculations suggest that metal(loid) and acidity pumped into the pit lake in the summer will accumulate in the epilimnion. In the short-term, the concentrations of dissolved species in the pit-lake epilimnion will increase more rapidly, from high load water pumped near the water surface. In the medium-term, increased loads pumped to the pit lake will gradually change the pit-water quality, as the pit lake mixes annually. In the long-term, acidification of the entire pit lake is possible, as seen in the epilimnion, which in turn increases solubility of metals and represents an increasing environmental liability.

The volume of water that enters the impacted water-management circuit is likely to increase due to additional sources of water becoming non-compliant in respect to discharge standards. In addition, deterioration of IP and waste-rock seepage water quality is expected to continue, as part of decades-long breakthrough of contaminants through the mine waste and consumption of buffering capacity. These processes could be diminished by reducing the load sources from the mine waste through a reclamation process prior to discharge into the FPL. Alternatively, the high load streams could be isolated and treated separately. Separating treatment streams would necessitate a treatments system design that accommodates lower flow rates and higher load influents, for efficient contaminant removal.

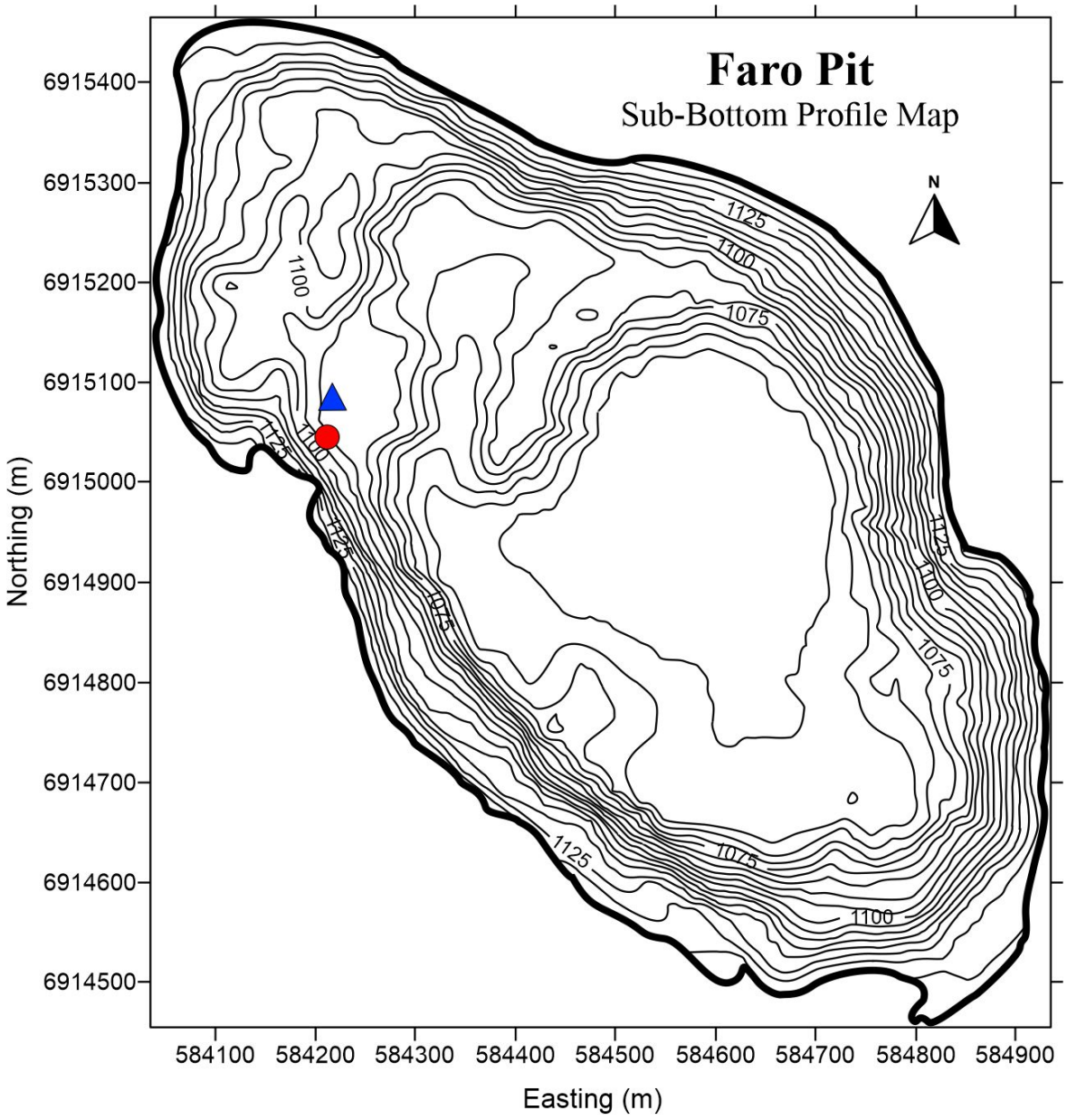

Figure 2.1 Faro Pit bathymetry survey results (Laberge 2012). The blue triangle shows the location were the first sampler (FP1) was placed in September 2019. The red circle shows the location were the second sampler (FP2) was placed in September 2021. The sampling manifold was placed on the closest shore to the sampling points, close to the Faro Pit pumping station.

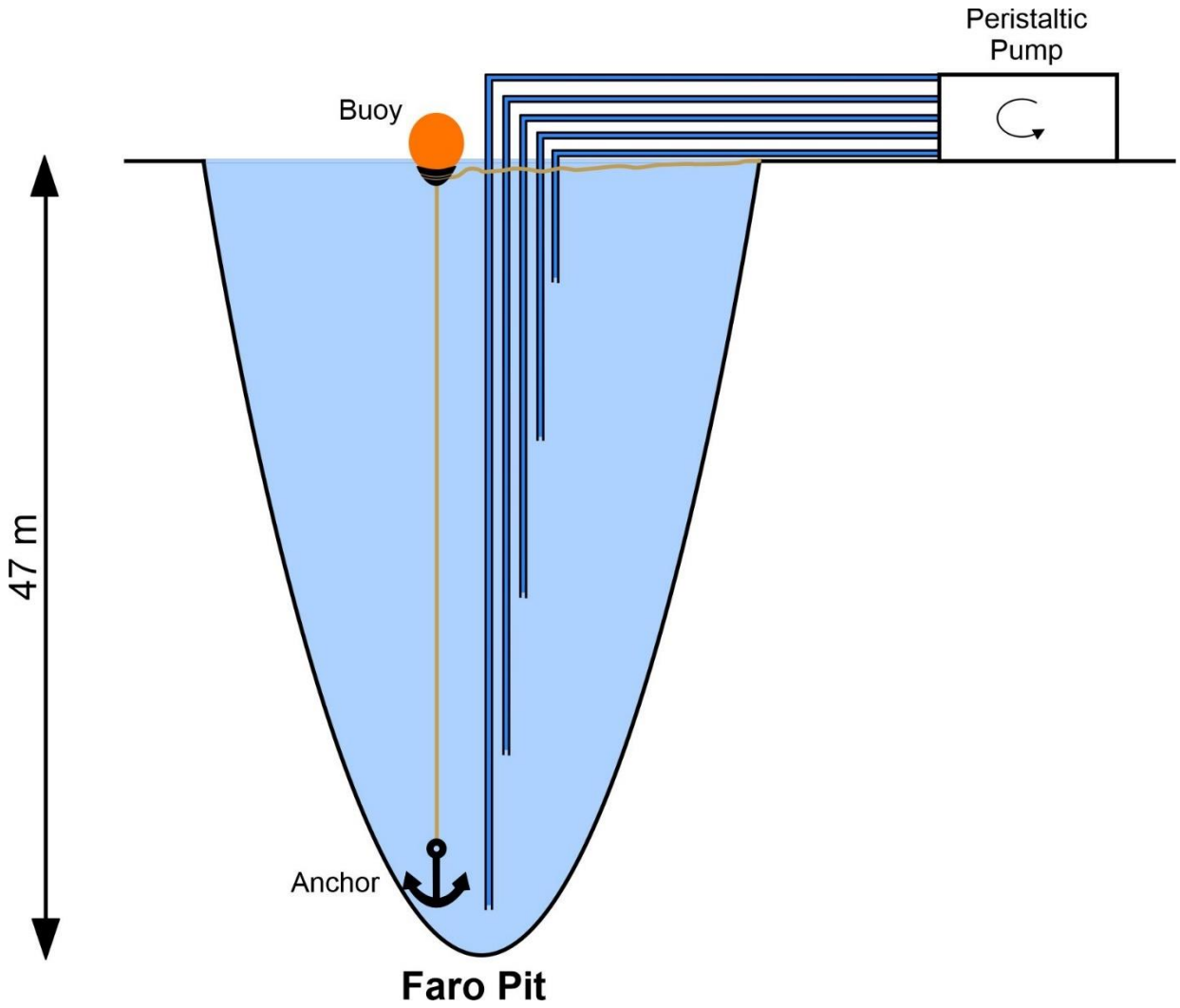

Figure 2.2 Diagram of the Faro Pit lake sampler. Representation of the components of the sampler when it was installed in the pit lake in September 2019. This figure is not to scale.

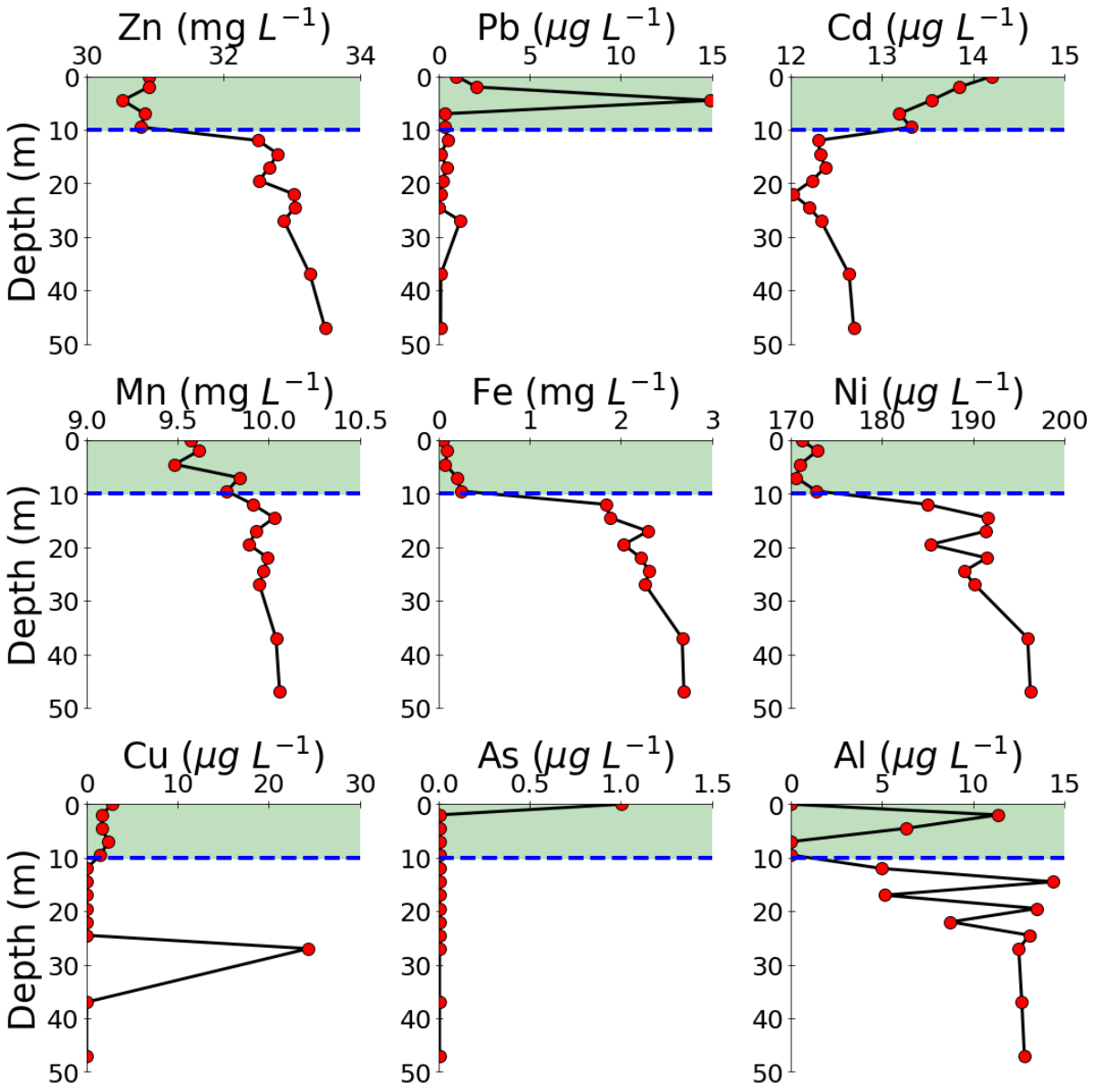

Figure 2.3a Dissolved elemental concentration depth profile in the FPL, sampled on September 5th, 2019. The blue line marks the thermocline, the green highlighted are above depth 10 m marks the epilimnion, and the plain white are under the blue line is the hypolimnion.

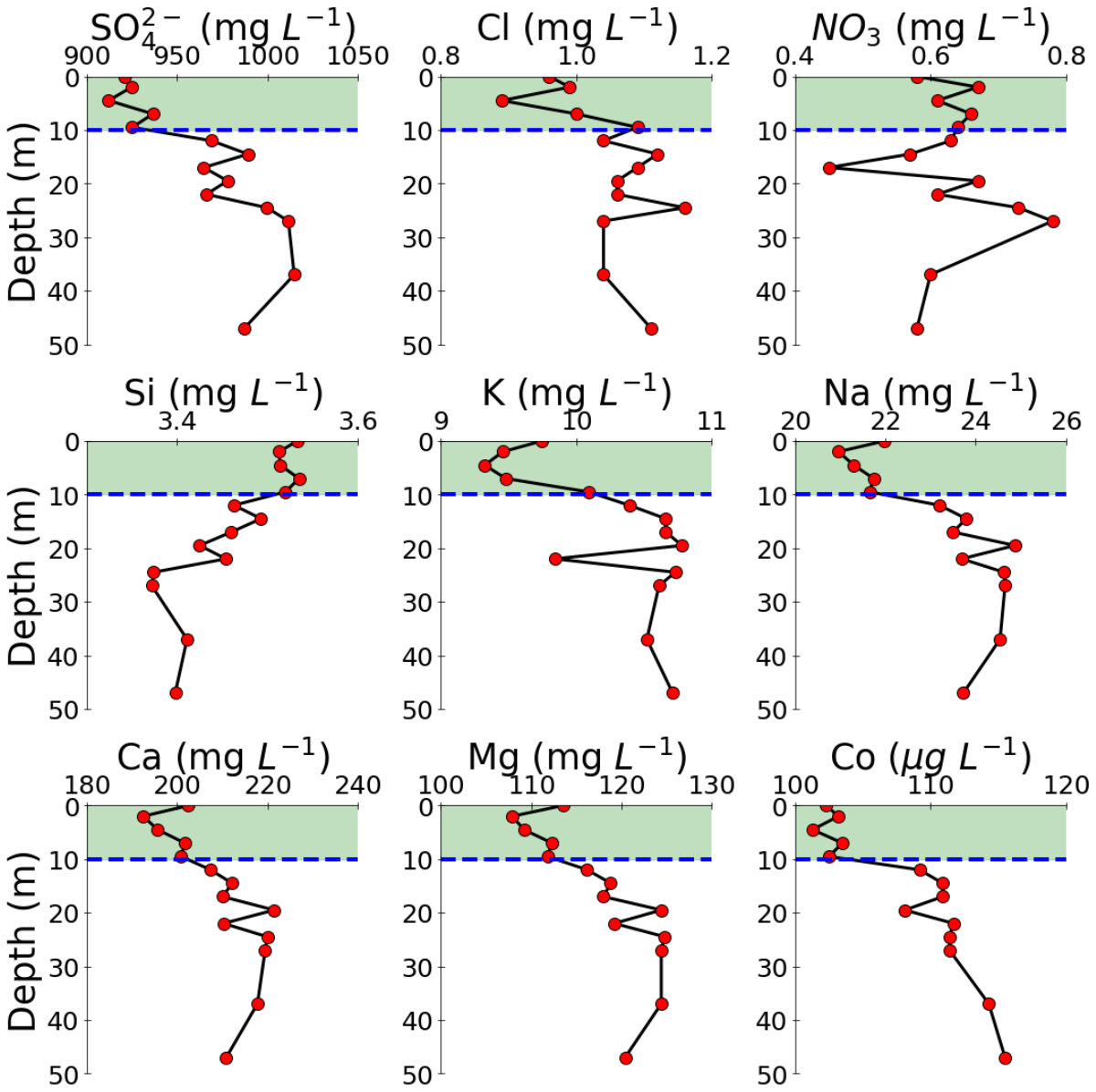

Figure 2.3b. Dissolved elemental concentration depth profile in the FPL, sampled on September 5th, 2019. The blue line marks the thermocline, the green highlighted are above depth 10 m marks the epilimnion, and the plain white are under the blue line is the hypolimnion.

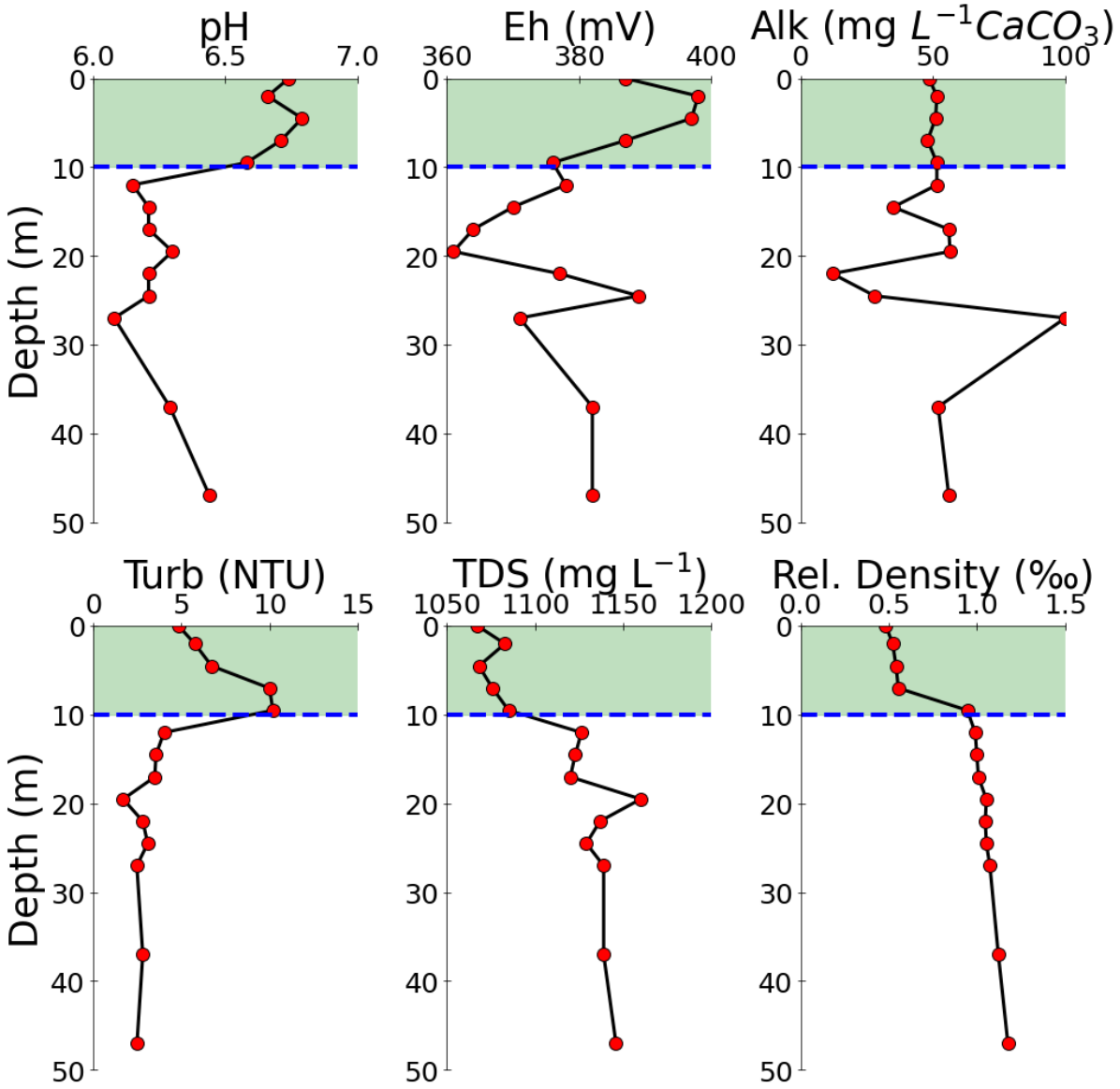

Figure 2.4 Depth profile of geochemical tests performed at the FPL on September 5, 2019. The blue line marks the thermocline, the green highlighted are above depth 10 m marks the epilimnion, and the plain white are under the blue line is the hypolimnion.

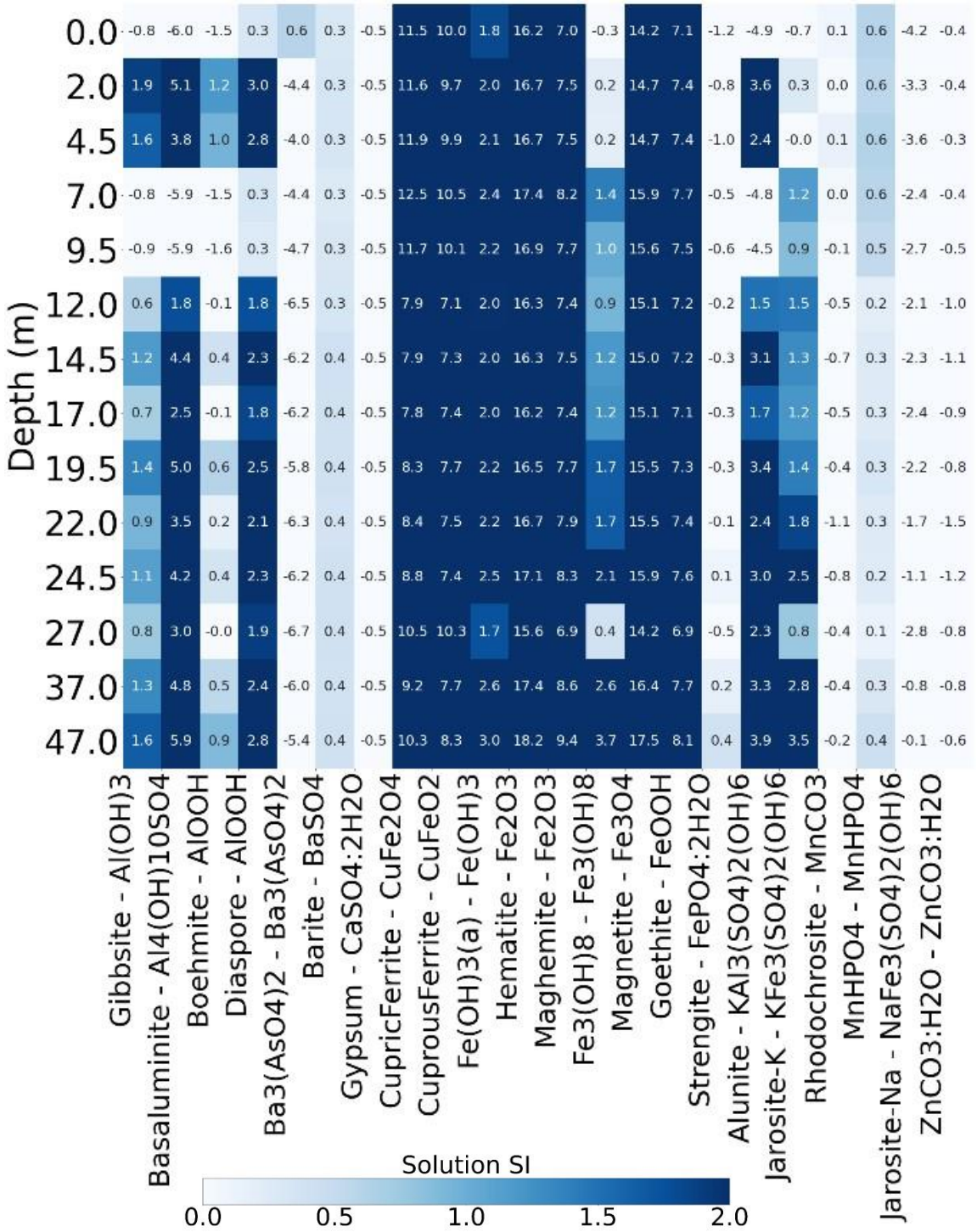

Figure 2.5 Crosstab of the mineral phases and depth, for the FPL on September 5th, 2019. The values show the saturation index (SI), and the shade of color highlights positive values as shown in the continuous scale. Only mineral phases with SI values above -0.5 are included. The depth values are not spaced to scale.

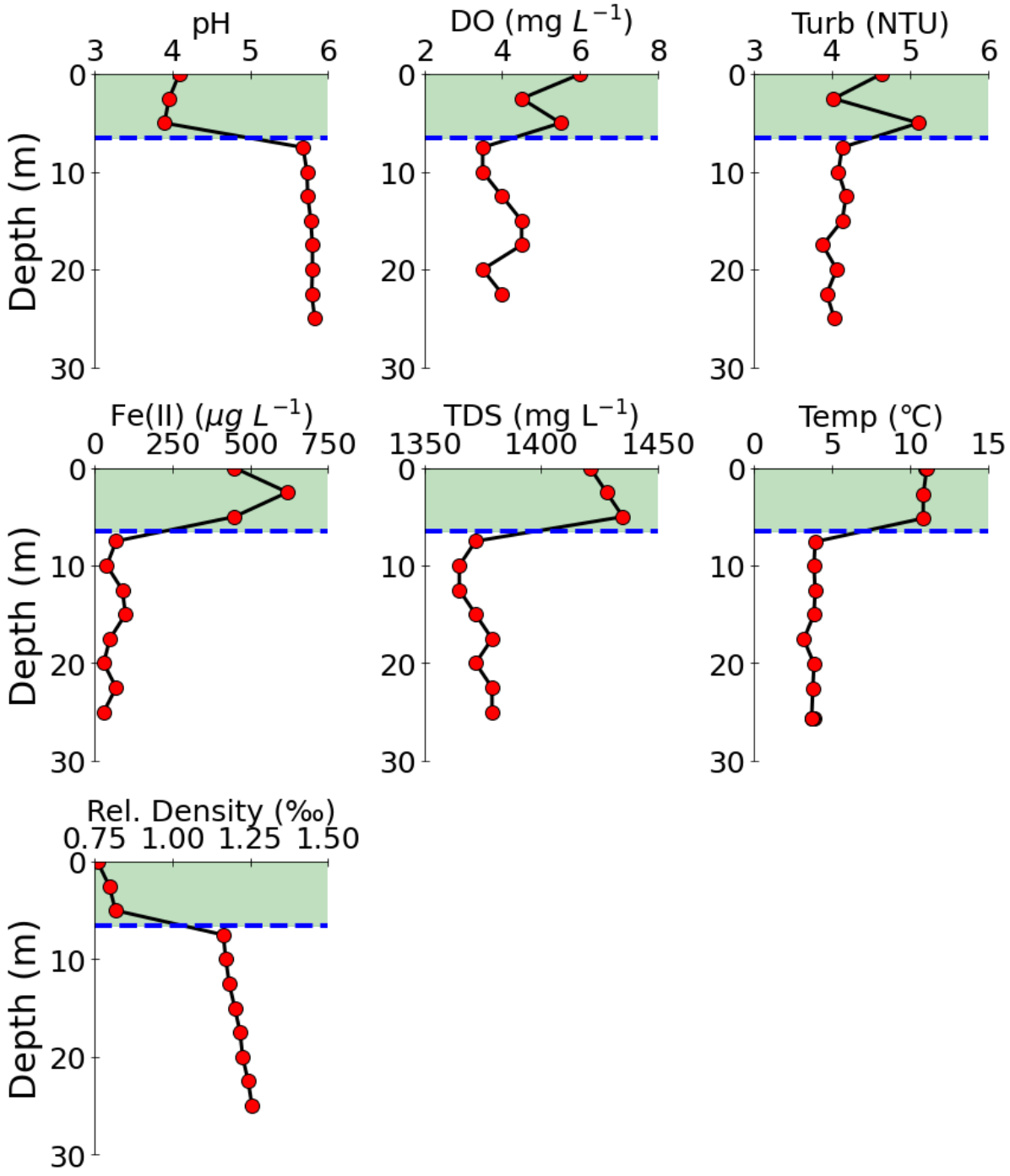

Figure 2.6 Depth profile of geochemical tests performed at the FPL on September 4th, 2021. The blue line marks the thermocline, the green highlighted are above depth 7.5 m marks the epilimnion, and the plain white are under the blue line is the hypolimnion.

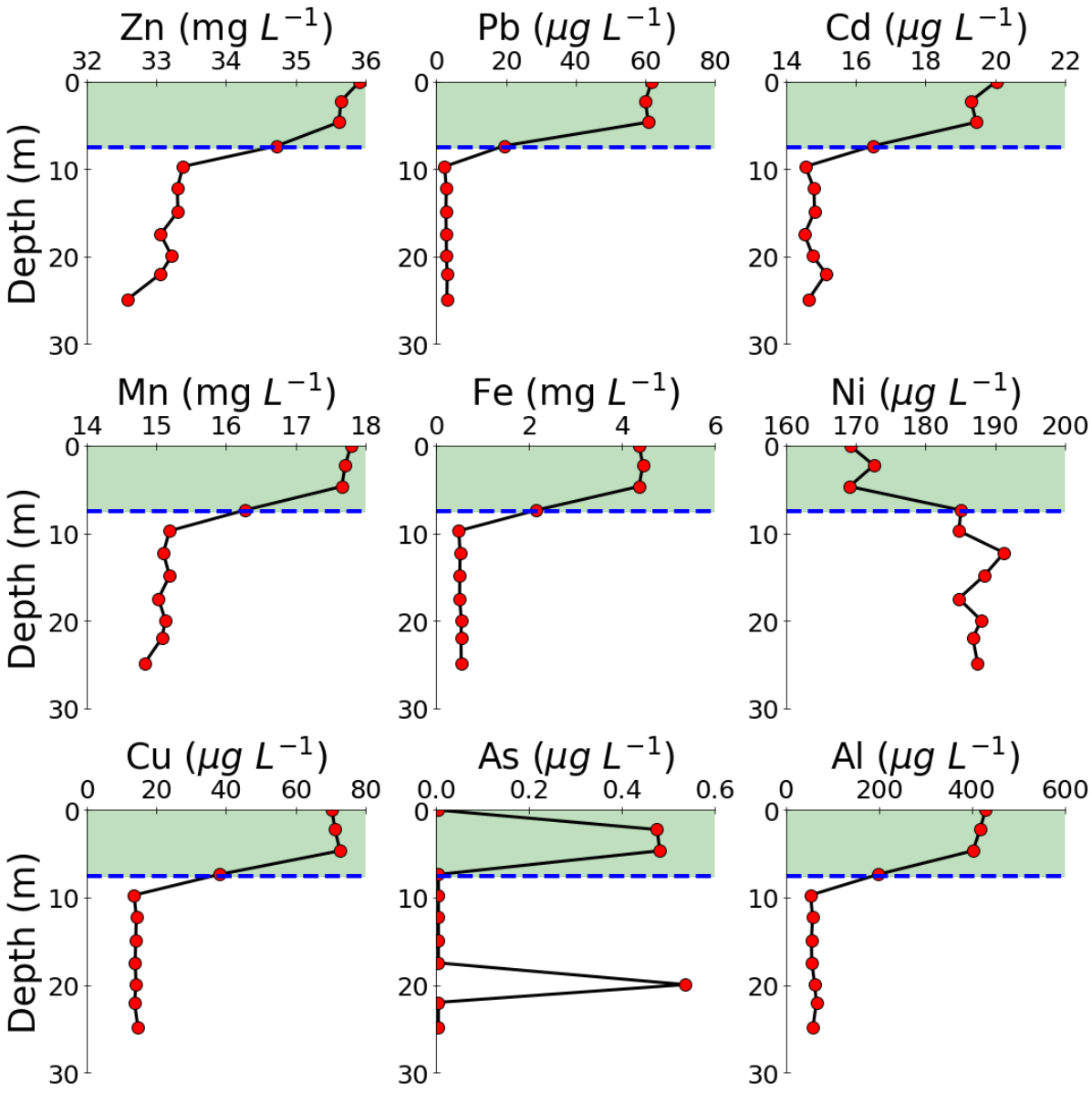

Figure 2.7 Dissolved elemental concentration depth profile in the FPL, sampled on September 4th, 2021. The blue line marks the thermocline, the green highlighted are above depth 10 m marks the epilimnion, and the plain white are under the blue line is the hypolimnion.

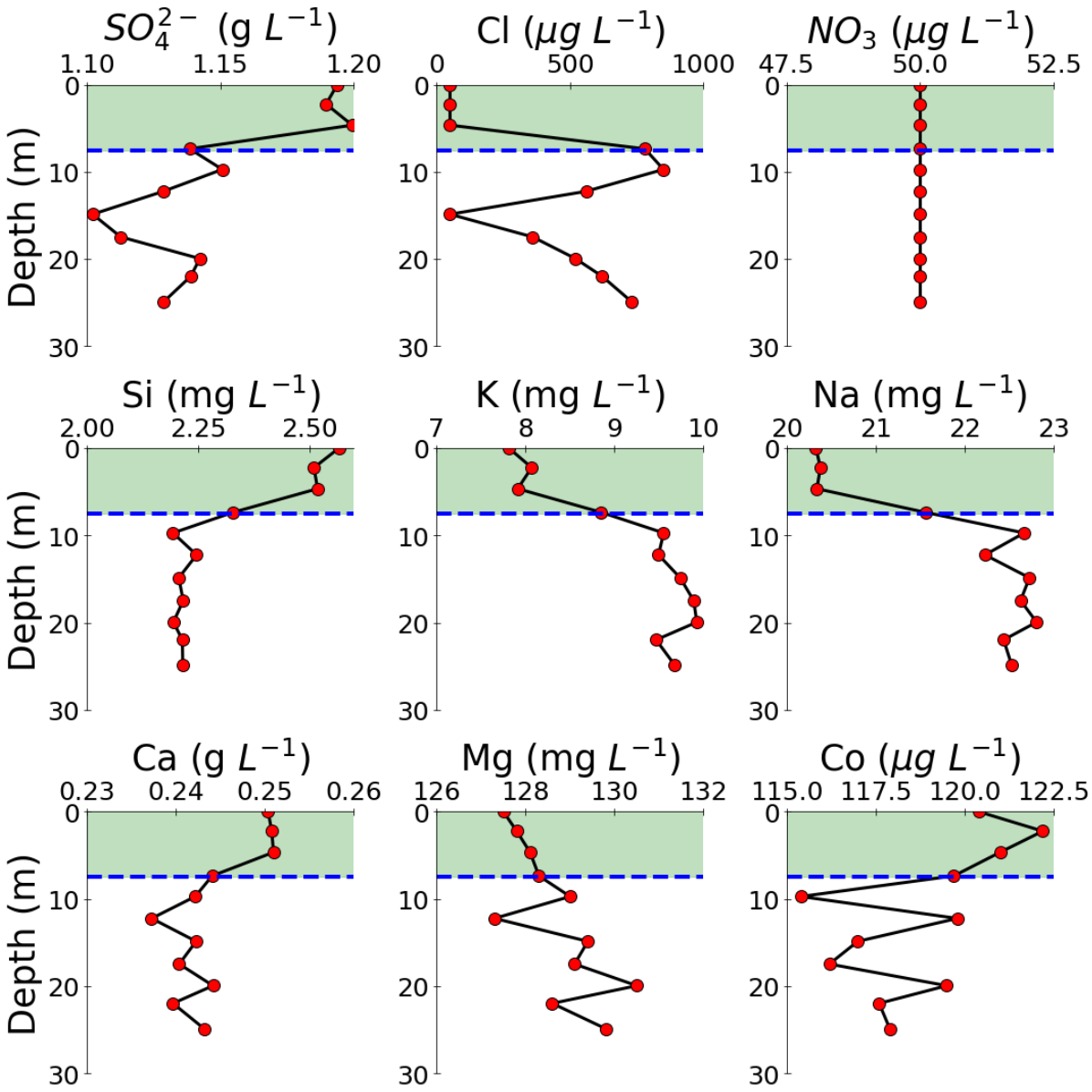

Figure 2.7b Dissolved elemental concentration depth profile in the FPL, sampled on September 4th, 2021. The blue line marks the thermocline, the green highlighted are above depth 10 m marks the epilimnion, and the plain white are under the blue line is the hypolimnion.

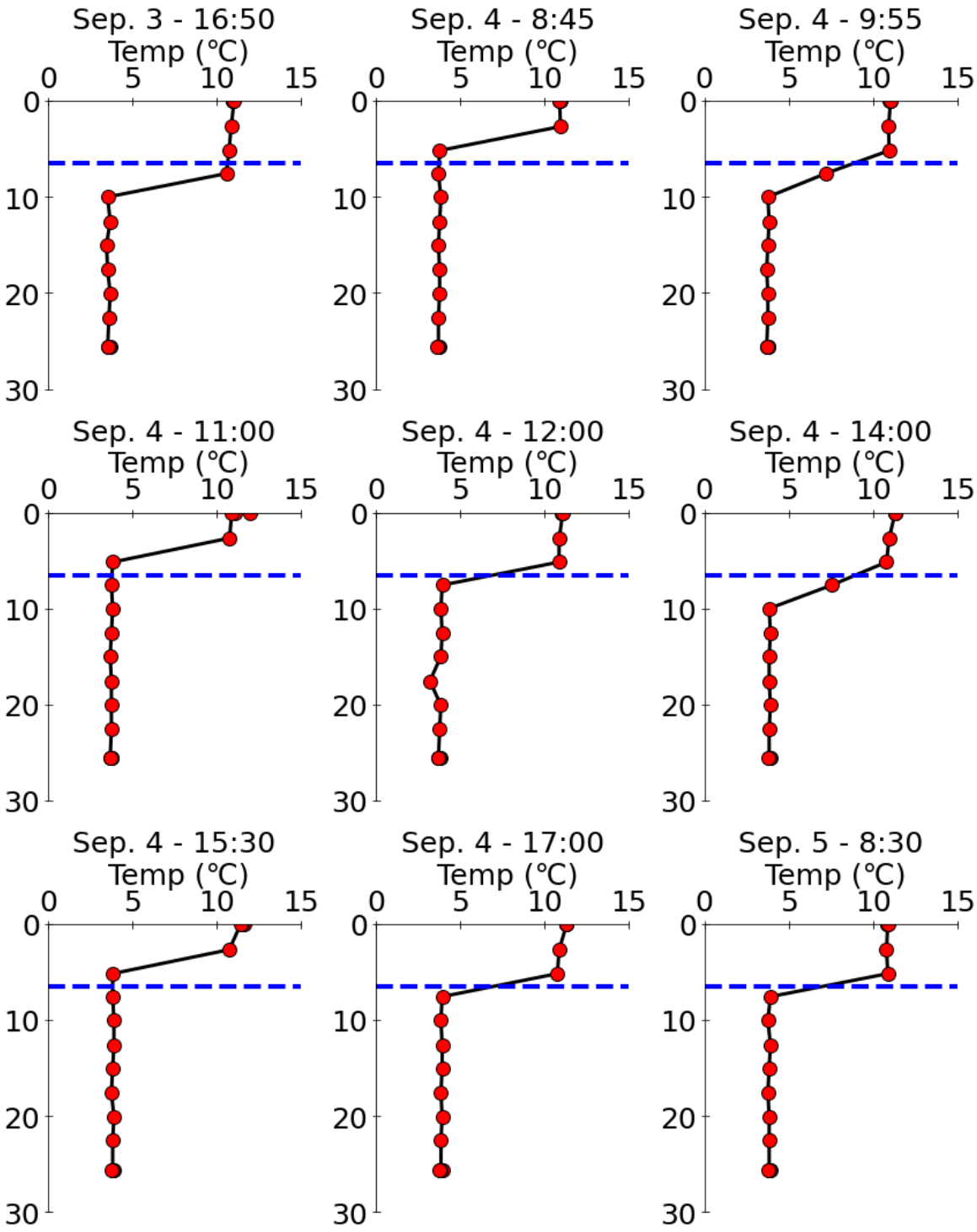

Figure 2.8 Temperature depth profile at FPL, collected with a thermistor. The measurements were conducted between September 3rd, 2021 and September 5th, 2021, at the stated times. The blue line marks the average location of the thermocline, in this time frame.

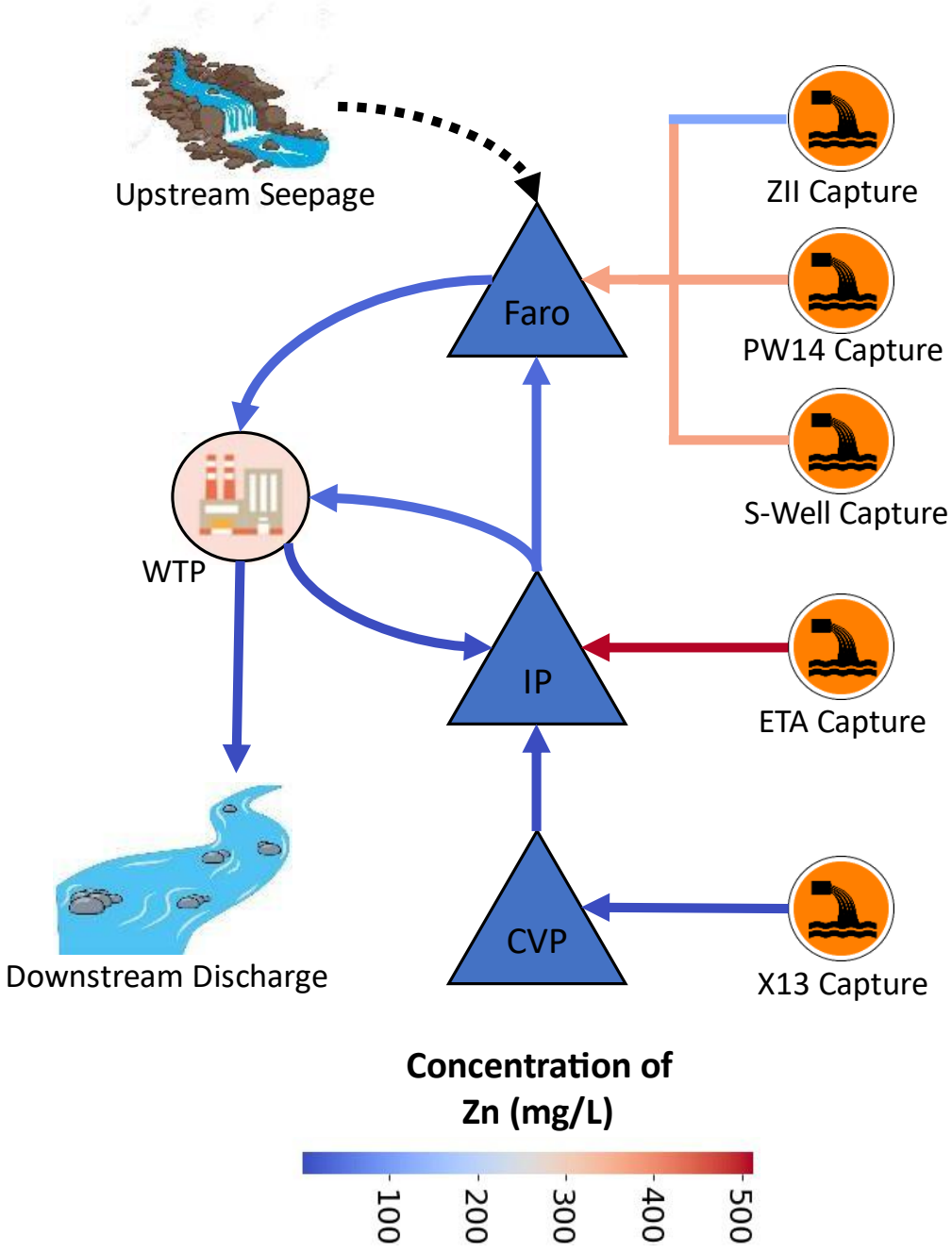

Figure 2.9 Mine waste contact water conveyance system schematic at the FMC, as of 2019. The orange fill circle elements represent seepage or groundwater capture systems. The triangles represent the water reservoirs: Faro Pit Lake, Intermediate Pond (IP), and Cross Valley Pond (CVP). There is seepage flowing into the Faro Pit from the north pit wall, represented in this diagram with a dashed black line. The water treatment plant (WTP) and receiving environment and also represented. The arrow show the water conveyance pathways, colour coded to show the relative concentration of Zn.

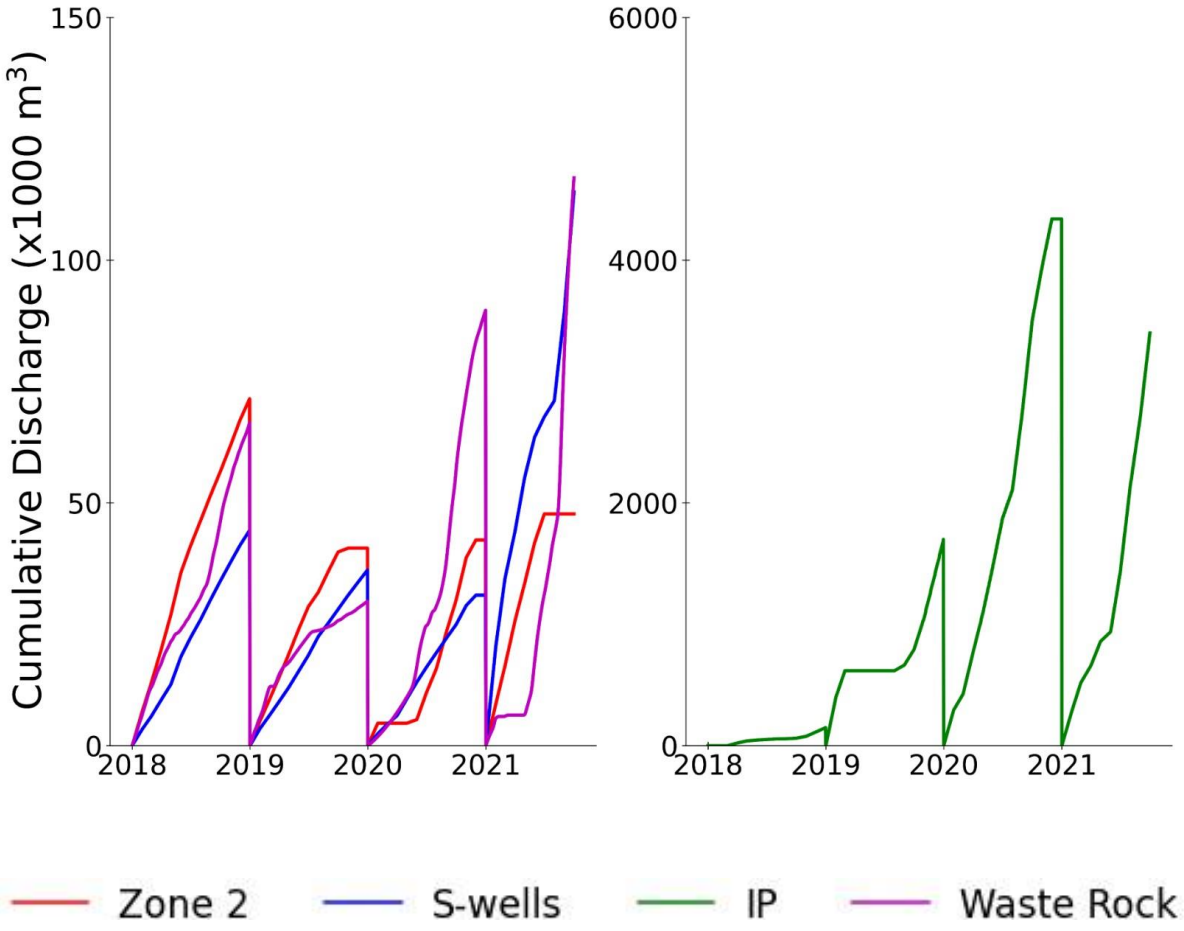

Figure 2.10 Cumulative annual water discharged. Each line represents a water source into the FPL. The Zone 2 backfilled pit, S-wells groundwater capture system, supernatant tailings water Intermediate Pond (IP), and waste rock surrounding the Faro Pit.

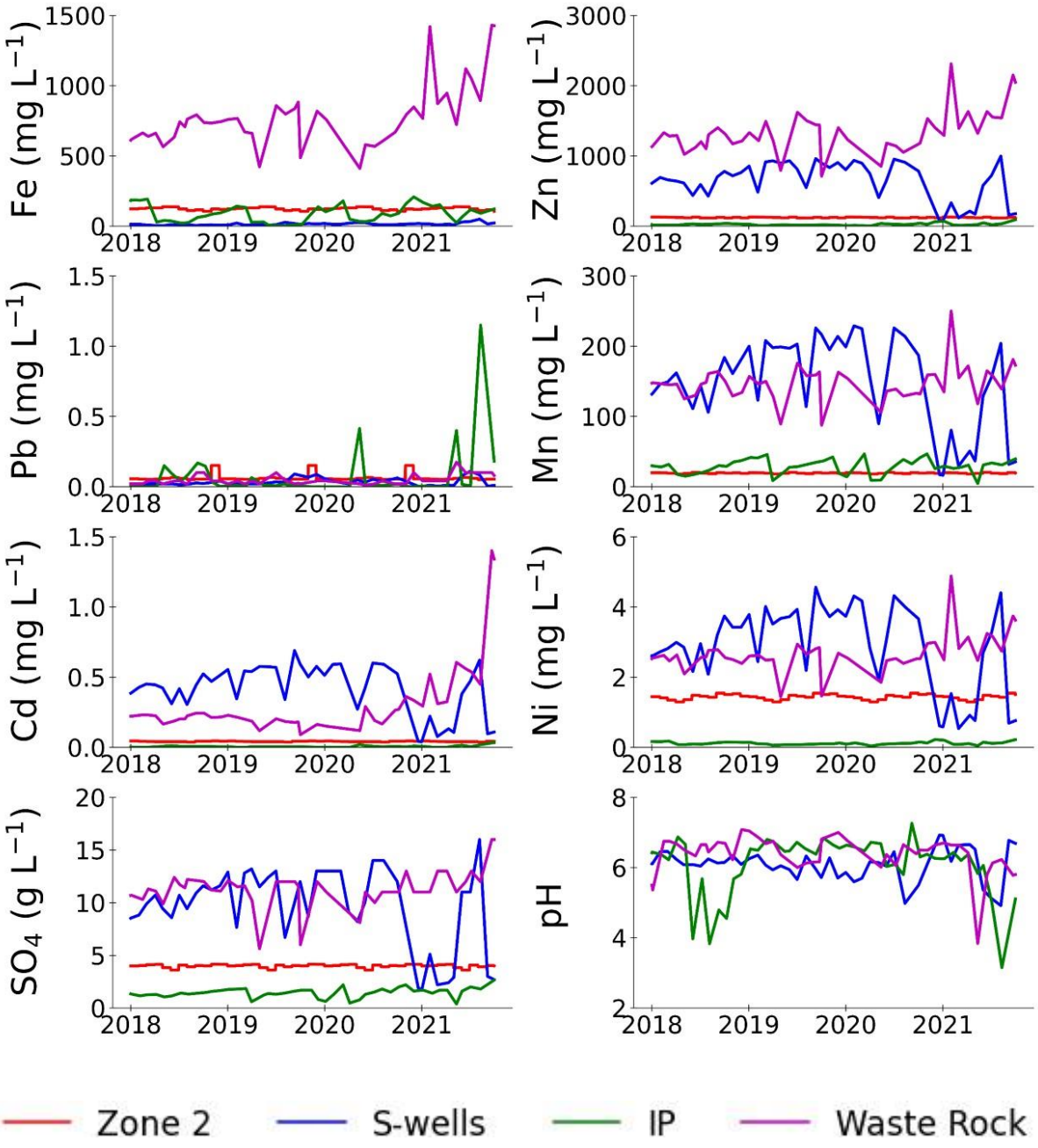

Figure 2.11 Timeseries of dissolved species concentrations and pH. Each line represents a loading source into the FPL. The Zone 2 backfilled pit, S-wells groundwater capture system, supernatant tailings water Intermediate Pond (IP), and waste rock surrounding the Faro Pit.

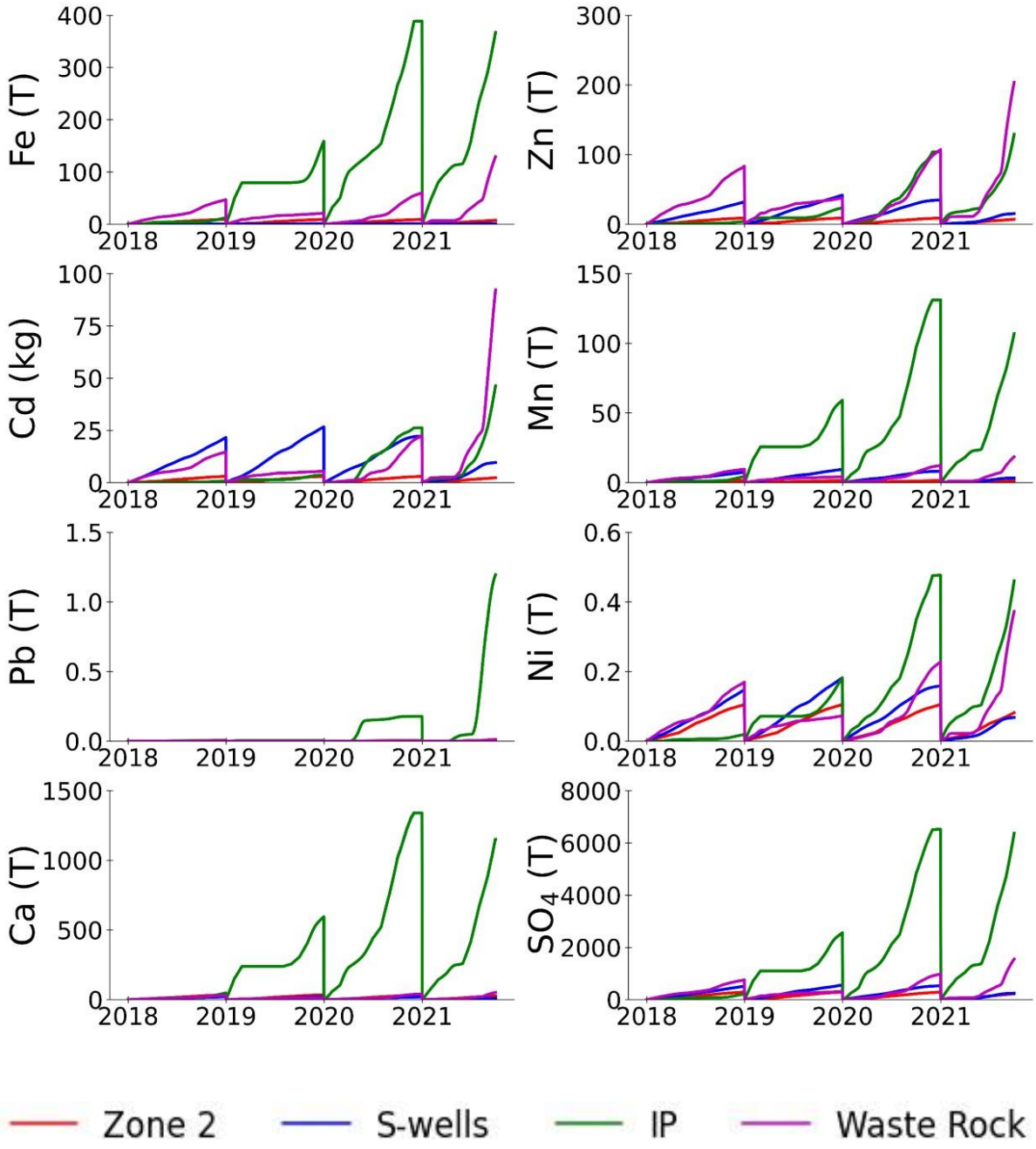

Figure 2.12 Cumulative annual loads of dissolved species. Each line represents a loading source into the FPL. The Zone 2 backfilled pit, S-wells groundwater capture system, supernatant tailings water Intermediate Pond (IP), and waste rock surrounding the Faro Pit.

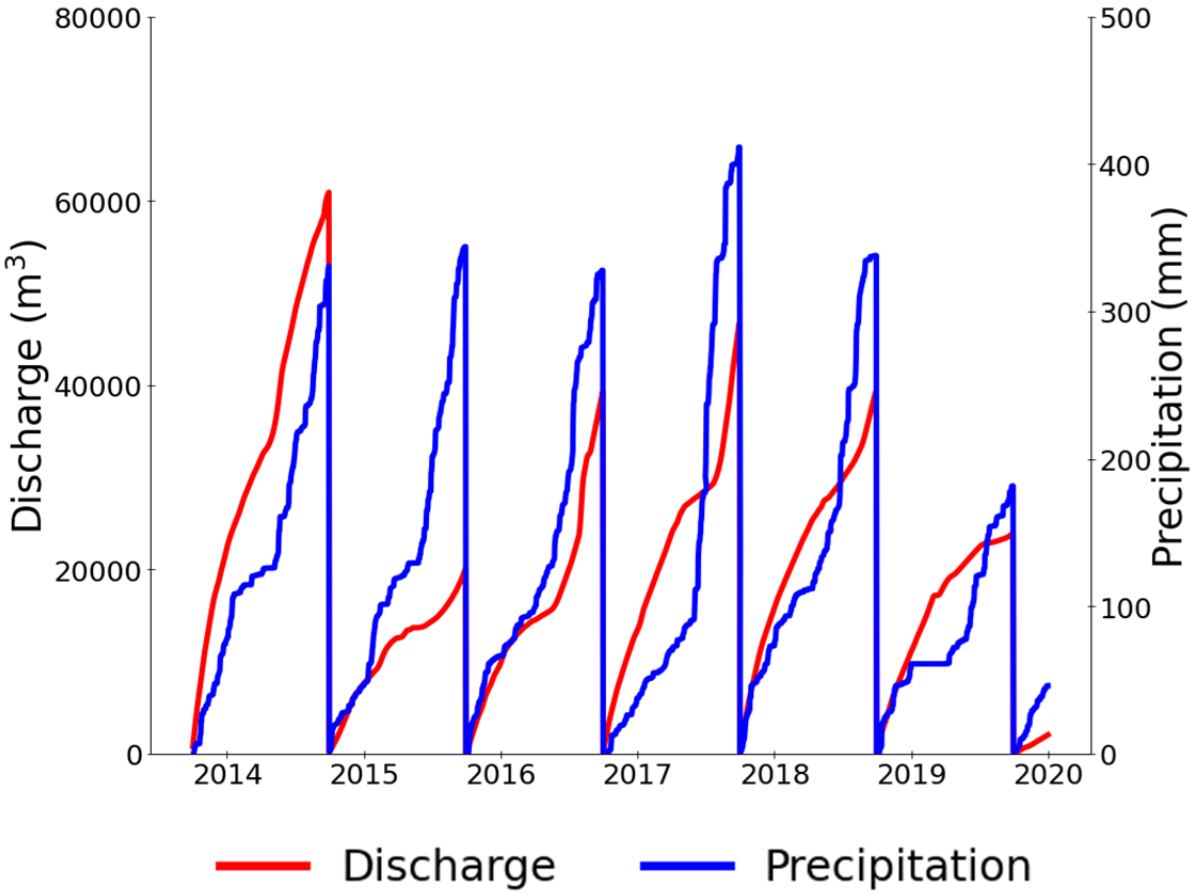

Figure 2.13 Cumulative annual precipitation measured at the Faro Weather station. Cumulative annual seep discharge from the X23 station. The annual cumulative sum is reset on October 1 each year, to report the water year for discharge and precipitation. The X23 sampling station is located in the paleo channel of the Faro Creek, downstream of the Intermediate Waste Rock Dump.

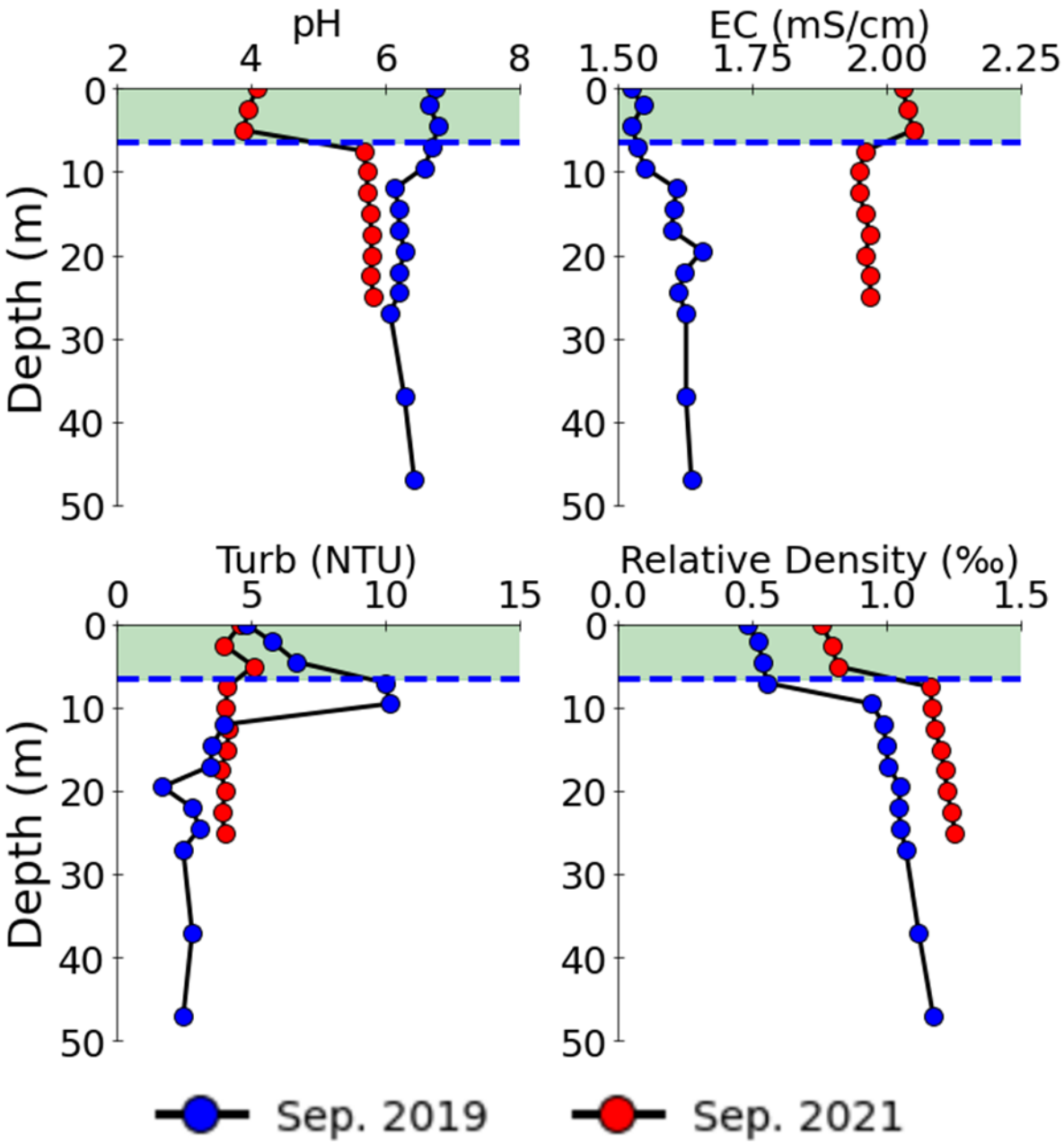

Figure 2.14 Depth profile of geochemical tests performed at the FPL. Two set of results are displayed from measurements on September 7th, 2019 and September 4th, 2021. The blue line marks the thermocline, the green highlighted are above depth 10 m marks the epilimnion, and the plain white are under the blue line is the hypolimnion.

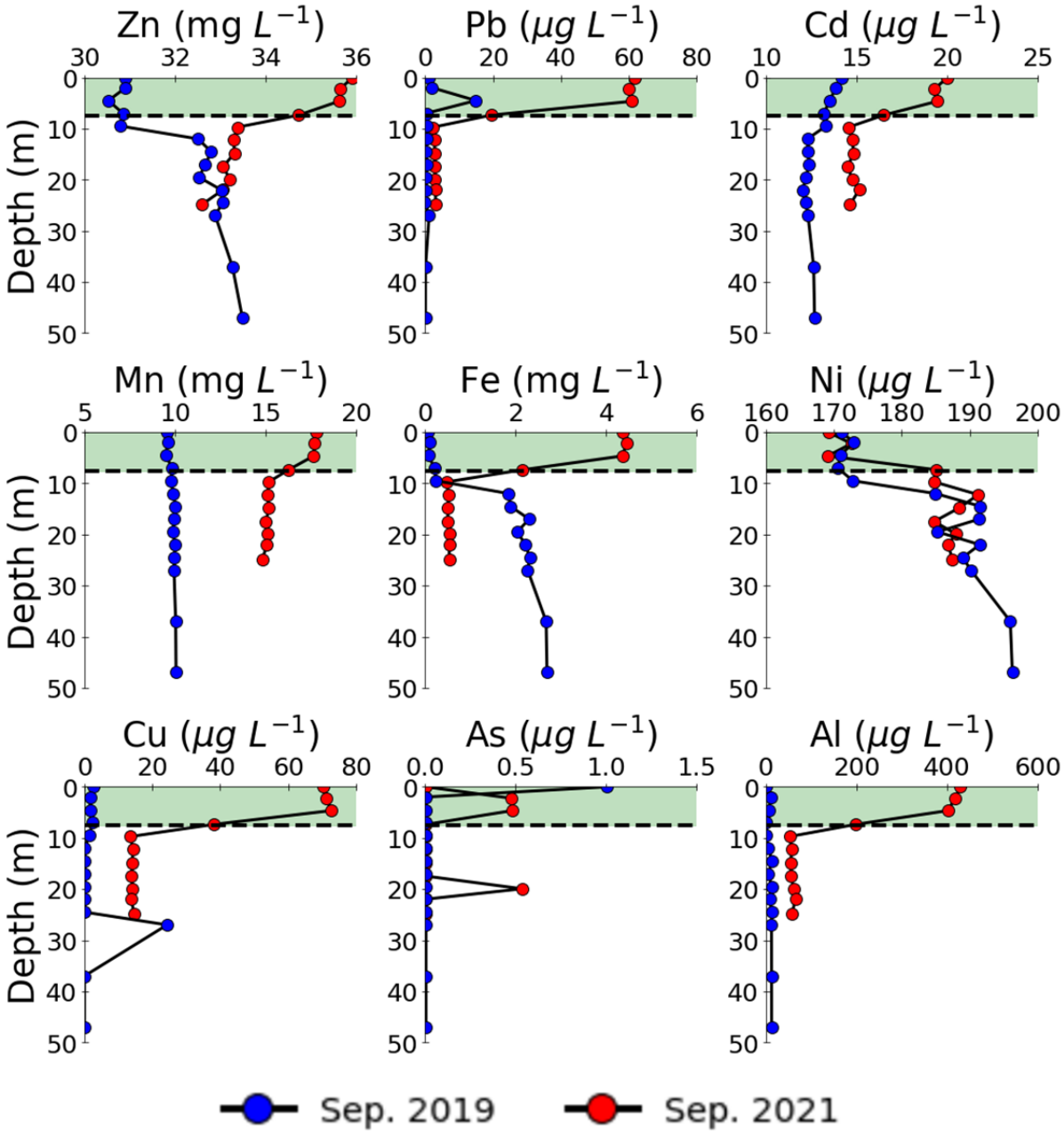

Figure 2.15 Dissolved elemental concentration depth profile in the FPL. Two set of samples displayed, collected on September 7th, 2019 and September 4th, 2021. The black line marks the thermocline, the green highlighted are above depth 7.5 m marks the epilimnion, and the plain white are under the blue line is the hypolimnion.

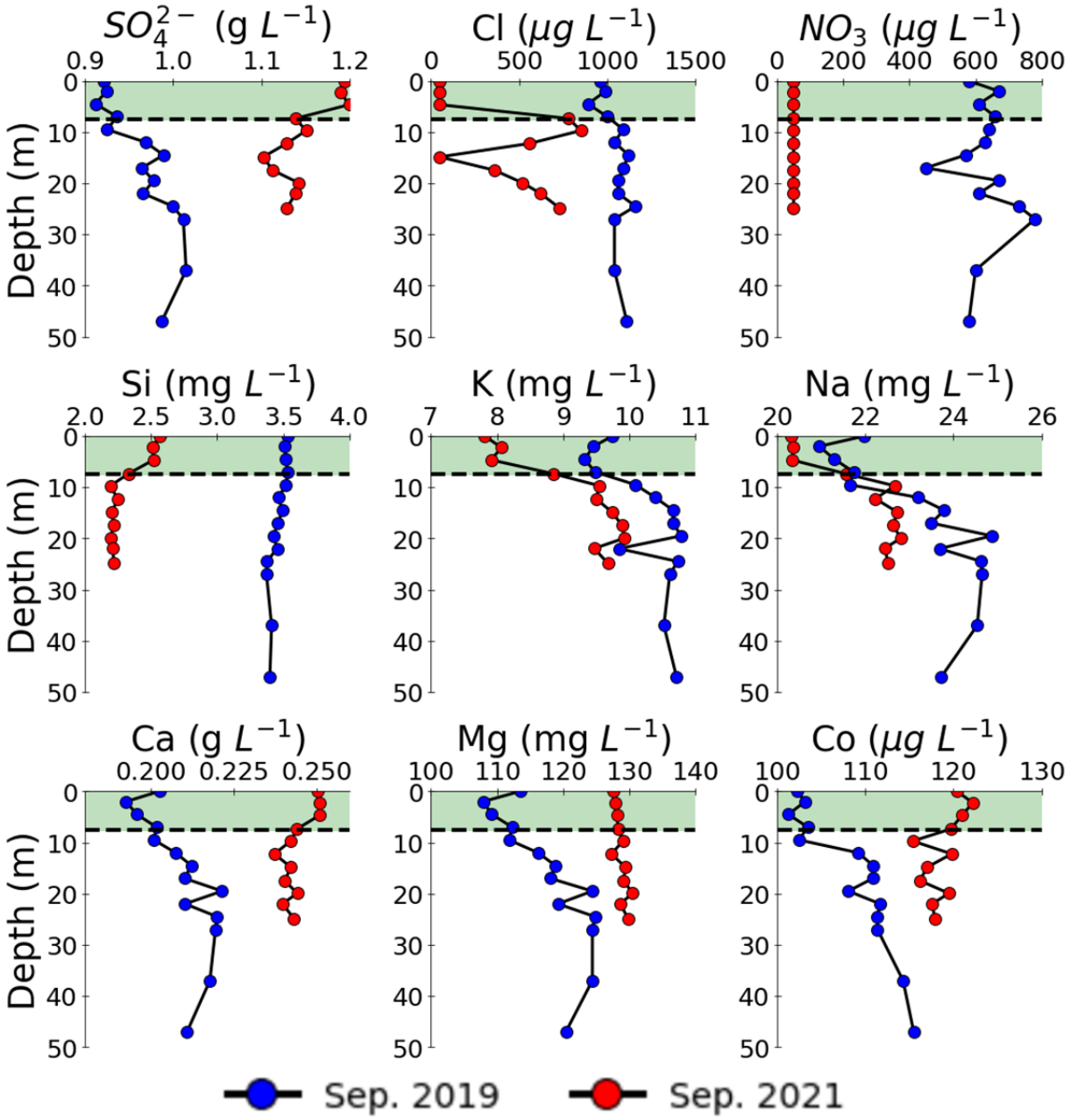

Figure 2.15b Dissolved elemental concentration depth profile in the FPL. Two set of samples displayed, collected on September 7th, 2019 and September 4th, 2021. The black line marks the thermocline, the green highlighted are above depth 7.5 m marks the epilimnion, and the plain white are under the blue line is the hypolimnion.

Table 2.1 Faro Pit lake sampler design. Sampling port depths for samplers FP1 and FP2.

Sampling Port #	Sampler 1 Port Depth (m)	Sampler 2 Port Depth (m)	Thermistor Bead Depth (m)
1	0.0	0.0	0.0
2	0.0	2.2	0.0
3	2.0	4.7	2.5
4	4.5	7.4	5.0
5	7.0	9.7	7.5
6	9.5	12.2	10.0
7	12.0	14.9	12.5
8	14.5	17.5	15.0
9	17.0	19.9	17.5
10	19.5	22.0	20.0
11	22.0	24.9	22.5
12	24.5		25.0
13	27.0		
14	37.0		
15	47.0		

Chapter 3:

Thermodynamic and Kinetic Controls of Contaminant Removal during Lime Treatment of Mine Impacted Waters: Laboratory Batch Experiments

3.1 Introduction

The water treatment process at the FMC uses lime (CaO) to produce an alkaline slurry to increase the pH of the treatment reactor as of 2022. Lime treatment is a widely used method for mine water in Canada (Aubé and Zinck 2003). The lime neutralization treatment approach includes the addition of Ca(OH)2 or CaO to the influent to elevate the pH to a target value, usually around pH 9.5, (Reactions [1.5], [1.6]).

Lime water treatment can be used successfully to remove Fe from solution. Initial concentrations of Fe(II), dissolved O2, and pH determine the removal rate and final Fe concentration (Kirby and Brady 1998). The addition of lime to the influent accelerates the oxidation of Fe(II) and causes the precipitation of carbonates and hydroxides (Johnson and Hallberg 2005). Dissolved Mn can also be removed from solution, promoting the precipitation of MnOx after the solution is increased between pH 9 and 10 (Tan et al. 2010). The removal of Zn and Ni can occur both through surface interactions on the Fe and Al precipitates, or through coprecipitation as oxide or hydroxide species (Miller et al. 2011, Miller et al. 2013). Coprecipitation of As and Fe(III) can occur in lime treatment, at mildly alkaline (pH 8) at solution Fe/As molar ratio ≥ 3 (De Klerk et al. 2015). The removal of Mg and SO4 from mine water can be achieved through lime addition, though a solution pH of 12 is necessary to precipitate Mg(OH)2 and gypsum (Geldenhuys et al. 2003, Madzivire et al. 2011).

The objective of lime treatment is pH neutralization and removal of dissolved metals (Miller et al. 2011). During treatment, CO2 and O2 are exchanged with the atmosphere and OH- ions are added as a base input, these processes increase both the pH and Eh of the

solution (Jenke et al. 1983). The increase of solution Eh and pH in the treatment vessel leads to the precipitation of Fe, Mn, and Al, primarily as amorphous oxides and hydroxides (Nordstrom 2020). Supersaturation and crystallization kinetics are the main controls on direct precipitation of dissolved species in a treatment reactor (Demopoulos 2009). Precipitation of minerals involves the nucleation and growth from a supersaturated solution (Dirksen and Ring 1991).

Metals are removed from solution either via direct precipitation or by sorption onto hydrous iron oxides (Dzombak and Morel 1990). Dissolved Fe and Al is removed from solution in a colloidal form, which can remain suspended in the treatment vessel. The formation of Al and Fe colloidal precipitates, promotes the sorption or coprecipitation of Fe^{2+}, Mn^{2+}, Pb^{2+}, Cu^{2+}, Co^{2+}, Ni^{2+}, As^{5+}, and Zn^{2+} at pH>5 (Cravotta and Trahan 1999; De Klerk et al. 2012).

Neutralization of mine waters with lime slurry integrated in a process called high density sludge (HDS) is widely used method (Aube and Lee 2015). The HDS process relies on physical and chemical processes, designed to occur during the treatment processes of lime slacking, mine water neutralization, flocculation, sedimentation, and sludge recirculation. The main input for HDS treatment is CaO, but it needs to be mixed with water (slaking) to produce a more stable compound $Ca(OH)_2$ (Johnson and Hallberg 2005). The slaking process produces a more reactive alkaline slurry when mixing water with low concentration of SO_4 (<500 mg L^{-1}) and temperature >65 ºC (Hassibi 1999). The lime dosing rate depends on the treatment process and influent water chemistry, the total required mass to increase the mine water to a target pH, after CO_2 outgassing, can be estimated from the measured hot acidity or the computed net acidity (Kirby and Cravotta 2005). During sedimentation the addition of a synthetic polymer aids particle aggregation and settling of suspended precipitates (Huck et al. 1977)

The objective of this study is to assess the fate and removal mechanisms of dissolved contaminants in mine impacted waters at FMC by batch experiments. Batch experiments were used to understand the connection between treatment conditions and the rate and extent of metal removal. Characterization of aqueous and solid phases after treatment were

compared to simulations conducted using existing surface complexation models to assess the fate of contaminants during lime treatment (Farley et al. 1985; Dzombak and Morel 1990; Miller et al. 2013).

3.2 Methodology

3.2.1 Batch Experiment 1 Design

Two sample compositions were examined during experiment 1, (1) FPL water, (2) and a blend of FPL water and Cross Valle Pond water. The FPL water was collected from a depth of 47 m in September 2019. Calculations were conducted prior to the experiment to estimate the mass of calcium hydroxide required to increase the pH to two experimental treatment thresholds: pH 10 and above pH 12, with excess buffering capacity. In a 50 mL centrifuge vials, $Ca(OH)_2$ was added as a slurry (100 g $Ca(OH)_2$:10 g H_2O; Table 1). After addition of the $Ca(OH)_2$, (0.08 g $Ca(OH)_2$:30 g H_2O; and 1.7 g $Ca(OH)_2$:30 g H_2O; Table 1) slurry, the vials were placed in an end-over-end rotator for 24 hours at 35 rpm to ensure the completion of the reaction. The vials were then centrifuged at 2500 rpm for 15 minutes and decanted to separate the aqueous and solid phases.

3.2.2 Batch Experiment 2 Design

Experiment 2 employed a stirred cell reactor (SCR) to progressively increase the pH of a solution, taking samples at different stages. FPL water collected in September 2019 was used for the experiment (Table 2). Contact with atmospheric O_2 during storage resulted in oxidation and precipitation of Fe from the solution. For two hours prior to the experiment, the FPL water was sparged with N_2 gas to remove dissolved oxygen, which was not present in the field sample. The experimental water was then spiked with a 2.0 mmolal $FeSO_4$ solution at pH 3 to restore the Fe(II) concentration to the level observed prior to precipitation of Fe from solution during transportation and storage.

The lime-slaking product $Ca(OH)_2$ was used directly to prepare the reagent base to avoid the exothermic reaction when CaO is mixed with water. The initial solution was a mix

of ultrapure water (Milli-Q Direct 8) and 800 mg L^{-1} (10.8 mmol L^{-1}) of $Ca(OH)_2$, close to the concentration at which it is saturated in respect to this solute.

An automatic titrator (Metrohm Titrando 902) was used to dose with a base solution at a constant rate. The reaction cell was stirred at 600 rpm with a small stir plate, ensuring effective mixing with no excessive turbulence. Each SCR titration was conducted in between 500 mg and 250 mg of sample volume and dosed with base solution at constant rate (Table 3). The pH of the solution was logged two times per second to capture small changes in the solution pH, and to ensure that collected samples represent the desired point of the process. A pH probe (Metrohm 6.0278.300) was connected to the automatic titrator for automated logging and pH-dependent dosing functions. The pH probe was calibrated using pH 4, 7, and 10 Thermo Fisher Scientific pH buffers (traceable to NIST) prior to each experiment. The pH probe had an integrated thermometer connected to the logging titrator. The solution Eh of SCR samples was measured using the combination platinum electrode (Thermo Scientific Orion 9678BN), calibrated to the sample temperature. The performance of the Eh probes were verified using Zobell's and Light's solutions, prior to each experiment (Nordstrom, 1977; Light, 1972). Concentration of Fe(II) of the initial experimental volume was determined with the 10-Phenanthroline method using a HACH DR/2400 spectrophotometer.

After the experiment was initiated, water samples were collected from the reaction cell with a syringe. The samples were collected at time intervals or solution pH values, predetermined to target specific pH-dependent reactions (Table 4). The samples collected were filtered with 0.45 μm cellulose acetate syringe filters, processed and analyzed following the procedure in section Methods - Aqueous Analysis. The experiments were automatically stopped by the automatic titrator when the SCR pH reached the target end of pH 10.

At the end of the SCR experiment, the resulting solution volume was measured and filtered through an in-line vacuum cellulose acetate 0.45 μm filter. The solid precipitate was weighed and compared with the initial dry weight of the filter, which was retained for solid phase analysis. In a separate experiment, replicate samples of the solids retained on 0.45 μm filter membranes were digested, with the volume of nitric acid recorded for subsequent mass-balance calculations.

3.2.3 Analytical Techniques

Samples from the batch experiments were filtered using cellulose acetate syringe 0.45 μm filters. Dissolved-metal samples were acidified to pH<2 with concentrated nitric acid and refrigerated to 4 °C prior to analysis. Cations were analyzed at the University of Waterloo Trace Metal Clean Room with inductively-coupled plasma optical emissions spectroscopy (ICP-OES; Thermo iCAP 6500 Duo) and inductively coupled plasma mass spectrometry (ICP-MS; Thermo XSeries 2). Anion concentrations were determined by ion chromatography (IC; Dionex ICS-3000).

3.2.4 Solid Phase Analysis

The solids collected on cellulose acetate filters were dried at ambient room temperature in a fume hood for 48 hours. The solid residue was then scrapped onto a glass observation slide and ground to a powder consistency. The sample was analyzed in a benchtop X-ray diffractometer (XRD) device (Rigaku Miniflex II with a Cu target). The X-ray diffraction data was collected over the range $10° < 2\theta < 70°$. Measurements were recorded on steps of $0.05° 2\theta$ at a scan rate of $0.5\ min^{-1}$.

Filtered dried solids were then dispersed on conductive carbon tape applied to a metal sample stub. Sample preparation was completed under standard atmospheric conditions before scanning electron microscopy with energy dispersion spectroscopy (SEM-EDS). Grain mounts were characterized with a FEI Quanta™ 250 FEG-ESEM with an Oxford Instruments x-act silicon drift detector (SDD) for energy-dispersive X-ray spectroscopy (EDS). An accelerating voltage of 20 kV was used to collect back-scattered electron (BSE) and secondary electron (SE) images with a sample – detector distance of 10 mm.

The density of FPL water was determined as a function of temperature, salinity, and pressure. These parameters are inserted into the UNESCO equation for water density calculations (Millero et al. 1980). The total dissolved solids (TDS) concentration for the density equation was calculated by the summation of the major ions found in solution: Ca, Mg, Na, K, Fe, Zn, SO_4, and a correction to account for CO_2 degassing. Alkalinity, expressed as mg $CaCO_3\ L^{-1}$ was multiplied by a 0.48 (Hem, 1985).

3.2.5 Geochemical Modeling

The open access geochemical modelling software package PHREEQC coupled with the wateq4f database was used to determine the geochemical speciation of surface water and batch experiment samples (Parkhurst & Appelo, 1999). The speciation calculations ran on a loop at varying pH and Eh conditions, the process yielded a results matrix that can be summarized in a solution-specific species stability diagram or a dominant species time-series. Saturation indexes of relevant mineral phases were calculated using PHREEQC for the purpose of interpretation of control through solid-phase precipitation. The normalized saturation index (SI) is defined by the equation below for each species in the database (Jurjovec et al. 2002):

$$SI_N = \frac{\left(log \frac{IAP}{K}\right)}{N}$$

Where: IAP is the ion activity product of the elements in the phase, K is the equilibrium constant, and N is the number of ions that could precipitate. Values >0 indicate that the solution is supersaturated with respect to the mineral phase, values <0 indicate undersaturation, values =0 indicate equilibrium conditions. Normalizing the SI of the solid phases makes it possible to directly compare species with varying stoichiometric complexity.

3.3 Results

3.3.1 *In Situ* Measurements

The initial pH of the solution was 7.1 for the first experiment. The initial solution for subsequent experiments were spiked with HCl to decrease the solution pH to 6.40, similar to the observed field pH of 6.44 (Figure 3.1). The addition of the base solution increased the pH rapidly from the initial value to pH 9.5. After pH 9.5, the observed solution pH leveled off with an inflection to a slightly decreasing trend to pH 9.4. In the last hour of the experiment the solution pH increased more slowly to the target pH of 10, when the experiment was stopped. At a constant dosing rate, the amount of base needed to increase the solution pH

from 6.5 to 9.5 was similar to the amount was needed to increase the pH past the convex plateau between pH 9.4 and pH 9.5.

The Eh of the solution was measured once a minute (Figure 3.2). The initial Eh measurements of the solution of the first two experiments differed because these solutions were not sparged with N_2 prior to starting the experiment and contained differing concentrations of CO2(g). The Eh values fluctuated rapidly in the initial 10 minutes of the experiment between the initial concentrations of each experiment and 400 mV, as the base dosing and agitation began. The Eh values trended towards a value of 320 mV after at least three hours of experimental time, with constant dosing and mixing. The Eh value plateaued and decreased slightly between 250 and 350 mV at the same time as the pH values reach an inflection point at pH 9.4.

3.3.2 Water Chemistry

The principal anion in of all samples collected was SO_4. The concentration of dissolved SO_4 decreased slightly throughout the experiment from a starting value of 1.05 - 0.98 g L^{-1} (Figures 15, 16). The relatively small drop in concentration of SO_4, from 1.05 to 1.01 g L^{-1} occurred at a constant rate when the solution was between pH 6.4 and 9.0. After the solution reached pH 9.0, the concentrations of SO_4 rapidly decreased from 0.98 g L^{-1} 0.94 g L^{-1}.

The aqueous speciation analysis of S showed that SO_4 was the most abundant S species in solution throughout the experiment (Figure 3.5). Saturation index analysis indicates that the solution was slightly undersaturated in respect to gypsum ($CaSO_4 \cdot 2H_2O$) and $Zn_4(OH)_6SO_4$ (Figure 3.6). The solution was slightly supersaturated in relation to barite ($BaSO_4$) throughout the experiment.

The initial concentration of Fe(II) of the FPL water sample before storage was 2.7 mg L^{-1}, but after storage the concentration dropped by two orders of magnitude to 0.018 mg L^{-1}. After the initial experimental solution was spiked with HCl and $FeSO_4$, Concentration of Fe was found to be similar to the initial concentration in the FPL. At the onset of the experiment, Fe concentration decreased rapidly from 720 μg L^{-1} to a minimum of 6.6 μg L^{-1}

at pH 8, within the first 5 minutes of the experiment. The concentration of Fe remained under 8.4 μg L^{-1} for the remainder of the experiment (Figures 15, 16). A small increase in the Fe concentration at pH 9.7 was observed towards the end of the experiment.

Aqueous speciation analysis showed that Fe(II) was not abundant (~1% of total Fe). Different ferric hydroxide species ($Fe(OH)_2^+$, $Fe(OH)_3$) were predominant at solution pH under 9.2 (Figure 3.7). After solution pH reached 9.2, $Fe(OH)_4^-$ was the most abundant Fe species. Saturation index analysis showed that that the water was supersaturated with respect to multiple Fe phases throughout the experimental pH and Eh range, including amorphous $Fe(OH)_3$, goethite (α-FeO(OH)), magnetite ($Fe^{2+}Fe^{3+}{}_2O_4$), and hematite (α-Fe_2O_3), although the last two were unlikely to precipitate directly under the experimental conditions (Figure 3.6).

The concentration trend for dissolved Zn in all three experiments was consistent with each other (Figure 3.4). The initial Zn concentration was 14.6 mg L^{-1}. The minimum concentration of 0.03 mg L^{-1} was reached at pH 9, after which the concentration remained constant and close to the detection limit. Most of the Zn removal from solution occurred rapidly at the start of the experiment as the pH increased rapidly (Figure 3.3). The removal trend of Zn was similar to that of Fe in terms of the timing and overall titration curve shape. Aqueous speciation analysis showed that Zn^{2+} was initially the predominant aqueous species (Figure 3.8). As the solution pH increased, $Zn(OH)_2^0$ formed first and became the most abundant aqueous Zn species from pH 8.7. The timing of Zn removal from solution during the titration closely coincided with the transition to the predominance of $Zn(OH)_2^0$ complexes. The saturation index analysis showed that the SCR solution was only supersaturated in relation to a few Zn-bearing mineral phases between pH 8 and 9, including zinc oxides or hydroxides ($Zn(OH)_2$, amorphous ZnO, $Zn_4(OH)_6SO_4$) (Figure 3.6). When the solution pH was <8 and >9 the solution was undersaturated in relation to all relevant Zn species.

The concentration of Mn remained constant and close to the initial concentration (10 mg L^{-1}) from the start of the experiment until the solution reached pH 9.5 (Figure 3.3). Above pH 9.5, the Mn concentration decreased sharply (Figure 3.4). At pH 10, Mn reached

the minimum concentration of 0.23 mg L^{-1} after 180 minutes of experiment time. The decrease in Mn concentrations coincided temporally with the plateau in the solution pH (Figure 3.4). Detailed sampling from the reaction conditions of pH 9.0 to 9.7 in batch experiment 5 confirmed the simultaneous occurrence of the pH plateau and decrease in concentration of Mn in solution.

Concentrations of Ni and Cd concentrations exhibited similar trends to each other during the SCR experiments. The initial concentrations of Cd and Ni for each batch experimental replicate were slightly different (Figure 3.3). The initial concentration of Ni for the different replicates ranged from 112 to 193 μg L^{-1}. The initial concentrations of Cd from different experimental replicates were between 10 and 16 μg L^{-1}. As pH increased, the concentration of Cd and Ni of all experiment converged and decreased at the same rate until reaching a minimum value between pH 9.9 and pH 10.0. The concentrations of Cd and Ni decreased linearly with changes in pH until the end of the experiment when the solution reached pH 10 (Figure 3.4). The final observed concentration of Ni was 2.36 μg L^{-1}, which corresponds to a 98.8% removal fraction relative to the initial concentration. The final Cd concentration was 0.12 μg L^{-1}, this corresponds to 99.3% removal.

The initial concentration and removal trends of As and Pb were very similar in the three experimental replicates (Figure 3.3). The initial concentration between the batches were different, as well as the pH when the minimum concentration was reached. The initial concentration of As was between 3.5 and 6.8 μg L^{-1}, and the initial concentration of Pb was between 3.1 and 6.3 μg L^{-1}. The concentration of dissolved As and Pb decreased linearly with an increase in solution pH until the solution reached pH 9 (Figure 3.4). Both As and Pb concentrations remained below the method detection limits (0.03 μg L^{-1} for As; and 0.003 μg L^{-1} for Pb) after the solution reached pH 9.

3.3.3 Solid Phase Characterization

Solid-phase samples of the filtered precipitate were obtained and analyzed after at least 48 hours of drying. The bulk composition of the solid phase was obtained from the sample digested with nitric acid. For direct comparison between the experiment replicates,

the results were presented as a mass balance that shows the difference in dissolved species mass in the initial water, the final solution after treatment, and the filtered precipitate (Figure 3.9).

The mass-balance calculations of Mn, Zn, and Fe show a similar trend: high initial dissolved mass, very low final dissolved ion concentrations, and some mass as a precipitate (Figure 3.9). For Mn, the initial solution mass (7007 μg) and the final solution mass (1.099 μg) corresponded to a dissolved:solid ratio of 1:6376. For Zn, the starting mass was 20342 μg and the final mass was 9.415 μg, with a dissolved:solid ratio of 1:2161. The Fe initial mass was 20342 μg and the final mass was 8.0 μg, resulting in a dissolved:solid ratio of 1:362. These trends indicate removal of these elements of interest from the initial water and accumulation in the precipitated mass. The mass of precipitate and the calculated mass in the final solution did not sum to the initial mass in solution, likely due to loss of solids retained on the filter.

The Ni and Cd mass-balance calculations showed a very low final dissolved metal concentration relative to the initial mass dissolved in solution (Figure 3.9). The Ni starting mass was 135 μg and the final mass was 3.42 μg, resulting in a removal ratio of 1:42. The initial and final Cd masses were 8.13 μg and 0.08 μg; the dissolved:solid ratio was high at the end of the experiment 1:16737

The Ca and Mg mass balance calculations showed a similar trend: high initial mass, a small decline in the final concentration, and a very small mass retained in the precipitate. The initial mass of Ca was 150.0 mg and the final mass was 150.3 mg. The initial mass of Mg was 87.1 mg and the final mass was 77.8 mg. These trends indicate there was very little removal of these elements from the initial water.

Analysis of XRD data provided a nondescript pattern with no distinguishable peaks, in a 2θ range between 10º and 70º (Figure 3.10). A pattern with no discernable peaks indicated that through this method no crystalline solid phases were identified.

The morphology of the solid-phase samples from the base titration batch experiment was examined with SEM-EDS. The precipitate sub-samples, removed from the filter paper

after drying, were irregular flakes between 500 µm and 5 µm in diameter (Figure 3.11, 3.12). Detailed SEM images and EDS analysis were chosen to represent the most prevalent observable textures on the particle surfaces. At the 30 µm scale there were two distinctive textures on the surface of the particles (Figure 3.12): (1) stranded and (2) spherical. The stranded particle morphology appeared as with wispy strands resembled lines of smoke (Figure 3.12). The spherical particle were characterized by spheres morphology, ~0.5 µm in diameter, fuzzy in texture, and were aggregated as clusters on the surfaces of the particles (Figure 3.13).

The results from the EDS analysis showed that there were distinct compositional differences associated with the particles and zones with different textures in each particle. The zones with stranded texture had low proportion of Fe (~3 wt. %), high Zn (~40 wt. %), some Mn (~10 wt. %), and some Mg (~4 wt. %) (Figure 3.14, 3.15). The zones with spheres texture had much higher weight ratios of Fe (~18 wt. %), less Zn (~20 wt. %), less Mn (~5 wt. %), and similar amount of Mg (~4 wt. %) relative to the sections with wispy texture (Figure 3.16, 3.17). Although the weight ratios of Ni, Cd, Pb, and Cu were of interest, they represented less than 1% of the total sample weight ratios and no areas were identified where these elements were present above the detection limit of the EDS.

3.4 Discussion

3.4.1 Change in Geochemical Conditions

The batch experiment source water, collected from FPL hypolimnion in 2019, was not stable at atmospheric conditions. The most perceivable geochemical change to FPL water samples when exposed to atmospheric conditions was increased Eh and lower dissolved Fe. The pH (6.5) and alkalinity (50 mg L^{-1} $CaCO_3$) were stable after extraction and during storage prior to analysis and the experimental procedure. Dissolved Fe was found to not be stable in solution post-extraction, confirming that the element is redox sensitive in this system, and that partial removal from solution can be achieved by exposure to atmospheric levels of oxygen. Dissolved Fe(II) was added to the source water to increase the concentrations to levels initially present in the pit lake.

The source water was placed in a stirred cell reactor (SCR) and dosed with calcium hydroxide. The addition of the basic solution progressively increased the pH of the solution, and samples were collected at target solution pH values. Four replicated experiments indicate that contaminants are removed by processes that consistently occur over narrow pH ranges or time intervals during the SCR experiment. The narrow set of conditions that lead to the precipitation of dissolved species can be replicated systematically to understand the treatment of FPL water. The water sample used for this experiment is representative of the conditions of the pit-lake hypolimnion in 2019, but not representative of geochemical conditions of the pit-lake epilimnion in 2021.

Changes to the geochemistry of the water in the reaction vessel occurred rapidly after the start of the SCR experiment. The Eh of the water rapidly increased in the first 10 minutes of stirring in the SCR. As the experiment progressed the Eh values trended towards a value of 320 mV (Figure 3.2). The solution pH also changes rapidly with only small amounts of based added, in the first hour of the experiment (Figure 3.1). The pH increased from the starting value and plateaus between pH 9.2 and pH 9.5, within the first 100 minutes of the experiment.

3.4.2 Removal of Dissolved Species

The Fe concentration in the batch experiment decreased during the rapid pH and Eh increase in the SCR vessel, within the first 5 minutes of the experiment. Frequent sampling in the initial minutes of the titration were needed to characterize the decrease. The Fe concentration in the reaction vessel decreased rapidly from 720 $\mu g\ L^{-1}$ to a minimum of 6.6 $\mu g\ L^{-1}$ at pH 8, then remained under 8.4 $\mu g\ L^{-1}$ until the reaction reached pH 10 at the end of the experiment. (Figures 15, 16). The Fe concentration reached a minimum in the first 5 minutes of the experiment. This mechanism of removal does not appear to be solely driven by change of solution pH in the vessel, but rather a reaction dominated by oxidation of Fe(II) to Fe(III) species.

The precipitation of Fe(III) from solution occurs in three stages: formation of Fe(III) precursor solids, growth of Fe(III) colloidal particles around a precursor, and aggregation of

colloids to a precipitate that can settle in a reaction cell (Grundl and Delwiche, 1993). The formation of precursors Fe(III) solids for the subsequent precipitation of colloids is often the rate controlling step. At circumneutral pH, the precipitation of rate Fe(III) is controlled by the abundance of $Fe(OH)_3$ species in solution where the maximum rate of inorganic Fe(III) precipitation occurs at pH 8 (Pham et al. 2006). These experimental results are consistent with the observed timing and removal rate of Fe from solution. The experimental observations are also consistent with the speciation calculations, which indicate a transition at pH 8 from Fe(II) to Fe(III) species (Figure 3.3). The pit-lake solution in the reaction vessel remained supersaturated with respect to $Fe(OH)_{3\,(a)}$ throughout the experiment, particularly at the start of the titration (Figure 2.7). The dissolved Fe in the FPL is in a narrow pH-Eh range where Fe(II) species are dominant in solution (Figure 2.5). Amorphous ferric hydroxides precipitate as low-density flocs that can remain suspended in solution in a mixing cell. The addition of synthetic polymers can aid particle aggregation for subsequent sedimentation (Huck et al. 1976). The performance of polymers can be optimized under the appropriate mixing times, dosage rates, and mixing speeds, based on the influent water quality (Huck et al. 1977).

It was observed that dissolved Fe(II) oxidizes to Fe(III) and hydrolyzes, and precipitates as sparingly soluble ferric hydroxide phases. Enhanced oxygen ingress, which is facilitated by agitation of the solution, and increase in pH during the titration experiment accelerated oxidation of Fe(II) and precipitation of Fe(III). Between a pH of 7 and 8, the rate limiting factor controlling the oxidation rate of Fe(II) was H^+ activity, at higher pH values the oxygen ingress into the solution was the rate-limiting factor (Morgan and Lahav, 2007). With the rapid increase in pH and precipitation, there was not sufficient time for formation of crystalline minerals, which was observed during the analysis of the solid phase The EDS-SEM images of precipitate showed that solids formed during the experiment are poorly crystalline and occur as angular flakes (Figure 3.12). Analysis of XRD patterns acquired from the filtered precipitate produced nondescript patterns (Figure 3.10), with no distinguishable peaks which indicates that the precipitated phases were non-crystalline (Machala et al. 2007).

During the SCR experiment 99.8% of the dissolved Zn mass was removed from solution. The Zn concentration decreased steadily from the start of the experiment and reached a minimum at pH 9 (Figure 3.4). Around half of the zinc was removed near the start of the experiment, at the same time as the Fe precipitation (Figure 3.3). The images from the SEM-EDS analysis showed zones of wispy and spherical textures. These texture zones had different compositions, with the Zn occurring in the presence or in the absence of Fe. In the wispy-textured zones the Zn precipitates occurred with low Fe composition, of less than 3 weight %. In the spherical-textured zones, the Zn and Fe precipitated together in spheres of 0.5 μm in diameter.

Frequent sampling at the start of the SCR experiment indicated that the Zn speciation changed as the experiment progressed. In the first hour of the experiment the most abundant species was uncomplexed Zn^{2+} (Figure 3.8). As the experiment progressed, the $Zn(OH)_2$ species became the predominant species. At pH 9.5 the solution transitioned to the dominance of Zn-OH complexes, which led to further precipitation of Zn. The saturation index analysis showed that the SCR solution is only supersaturated in relation to zinc oxides or hydroxides mineral phases between pH 8 and 9 (Figure 3.6). When the solution pH was below pH 8 and above pH 9 the solution was undersaturated in relation to all Zn phases considered.

The Mn concentrations remained constant from the start of the experiment until the solution reached pH 9.5. The precipitation of Mn occurred between pH 9.5 to pH 9.7 for all the batch experiments (Figure 2.6). Despite the difference in titration rate in the batch experiments, the Mn precipitation rate increased as soon as the solution reached pH 9.5 (Figure 2.5). Although there was a pH plateau around pH 9.5 to pH 9.7, the Mn precipitate accumulated at the start of the plateau. The pH-dependent process that controls the removal of Mn appeared to be consistent in controlling Mn concentrations, despite the difference in experiment durations. The analysis of mineral saturation indices suggested that the phase that controls the precipitation of Mn was likely a form of Mn oxide (birnessite or bixbyite; Figure 9). The rate of Mn removal was proportional to the pH and Eh of the solution. The rate oxidation of Mn was characterized as a pseudo first order with respect to the presence of

Mn(II) in solution (Hem, 1981). Speciation analysis indicates that 78% of Mn was $Mn^{2+}_{(aq)}$ and 22% was $MnSO_4^0{}_{(aq)}$. The rate of Mn oxidation decreases when high concentrations of HCO_3^- and SO_4 are present (Davies and Morgan, 1989). The rate of Mn oxidation is autocatalytic, where the presence or initial formation of Mn mineral phases accelerate the rate of Mn oxidation (Hem, 1981). Other solids like FeOOH and δ-Al_2O_3 also enhance the oxidation of Mn(II). The SEM-EDS analysis showed that Mn precipitated in the wispy-textured zones, along with high Zn and low Fe mass proportions (Figure 3.14, 3.15). This observation indicates that the wispy texture precipitates were formed towards the middle of the experiment when Mn and the remaining Zn were removed from solution.

The mass balance calculation of the SCR experiments shows that Pb and As were removed from solution, but their mass was poorly recovered in the precipitate analysis. Poor recovery could be due to sorption of elements onto the filter paper or the storage vessel walls. The initial concentration of these elements was similar, between 3.1 and 6.8 $\mu g\ L^{-1}$(Figure 3.4). Pb and As were removed from solution when the pH of the reaction vessel reached 9.0 and remained below the detection limit until the end of the experiment. The Pb and As concentrations decreased at a constant rate, regardless of the solution pH.

The concentration of K, Cl and NO_3 increased linearly throughout the pH/Eh sweep of the experiment. These elements were likely present in trace amounts in the $Ca(OH)_2$ reagent used to prepare the base. Dissolved K, Cl, and NO_3 behave conservatively during the experiment, with an addition rate proportional to the base dosing rate. These elements can be used as an additional method to track the total base added to the SCR.

The mass balance of Cd and Ni indicated a high initial mass, low final concentration, and a remaining mass measured as a precipitate (Figure 3.9). The SCR experiment demonstrated the removal of these contaminants from the initial water and accumulation in the precipitated mass. The concentration of Cd and Ni decreased linearly with pH until the end of the experiment when the solution reached pH 10 (Figure 3.4). As the pH increased, the concentration of Cd and Ni decreased at the same rate in all the experiment replicates to minimum value (Ni 2.4 $\mu g\ L^{-1}$, Cd 0.3 $\mu g\ L^{-1}$) at pH 10 (Figure 3.3). The removal of Cd and Ni requires higher pH than other contaminants in the FPL influent. If these elements surpass

the water quality standard for discharge from the FPL, the treatment plants will require a higher treatment pH target. Treatment of Cd and Ni requires the treatment vessel to reach a pH of at least 10. To achieve the target pH of 10 the amount of neutralizing base input into the treatment base would have to increase between 80% and 100%, compared to a target pH of 9.4 (Figure 3.1).

The dissolved concentration of SO_4 only decreased slightly throughout the experiment, with a more pronounced drop above pH 9. Sulfate remained as the most abundant dissolved species for the duration of the SCR experiment. Saturation index analysis showed that the solution remained slightly undersaturated in respect to gypsum, anhydrite, and $Zn_4(OH)_6SO_4$ (Figure 3.6). The Ca concentration remained constant, so it is likely that gypsum did not precipitate. The solution was slightly supersaturated with respect to barite throughout the experiment. The presence of SO_4 can decrease the effectiveness of lime treatment because sulfate-bearing precipitates (commonly gypsum) can coat the surface of the lime particles and prevent effective wetting and dilution (Hassibi, 1999). During this experiment, the base was fully diluted in the dosing solution, so surface fouling was not likely to affect the efficiency of the acid-base reaction. For water treatment processes that use high SO_4 solutions for mixing lime or ones that recirculate sludge, the base dosing rate would have to be higher to account for the effect of SO_4 on the lime particles.

3.4.3 Precipitate Stability

Proper disposal of the precipitated solids from water treatment is necessary to remove contaminants from the mine load balance. Precipitates that were formed during water treatment release metal(loids) back into the environment if they are not disposed of properly. The reactions that formed the precipitates during the batch experiments are reversible. The solids produced during this experiment will likely redissolve if the Eh and pH values are lowered or reverted to the pre-treatment conditions (McDonald and Webb, 2006). The amorphous solids that form from the acid-base and oxidation reactions that occurred during the simulated treatment process are susceptible to redissolution (Aubé and Zinck, 1999). Additional metal species, that were removed from solution via adsorption to iron

oxyhydroxides and manganese oxides, may desorb from solid surfaces or redissolve along with the mineral substrates.

3.5 Summary and Implications

3.5.1 Summary

The iron concentration in the batch experiment decreased within the first 5 minutes of the experiment. During this time the remaining Fe(II) oxidizes to Fe(III), and the Fe(III) hydrolyzes and precipitates as ferric hydroxide phases. During the SCR experiment 99.8% of the dissolved Zn mass was removed from solution. The Zn concentration decreased steadily from the start of the experiment and reached a minimum at pH 9. The images from the SEM-EDS analysis showed zones of wispy and spherical textures in the precipitates. In the wispy-textured zones, Zn precipitated with minimal Fe wt. %. In the spherical-textured zones, Zn and Fe precipitated in similar weight proportions, in spheres of 0.5 μm in diameter. These observations show that Fe and Zn coprecipitated in the initial stage of the experiment (Figure 3.16, 3.17). Later in the experiment, Zn precipitated separately as amorphous Zn hydroxides (Figure 3.14, 3.15).

The precipitation of Mn occurred between pH 9.5 to pH 9.7. The SEM-EDS analysis shows that Mn precipitated in the wispy-textured zones, along with high Zn and low Fe mass proportions (Figure 3.14, 3.15). This observation indicates that the Mn and the last of the Zn precipitated at the same time from the solution.

At pH 9.0, Pb and As were almost completely removed from solution. The concentrations of Cd and Ni decrease linearly with changes in pH, until the end of the experiment, when the solution reached pH 10. The removal of Cd and Ni requires higher pH than other contaminants in the FPL influent. If these elements surpass the water quality standard for discharge from the FPL, the treatment plants will require operating at a higher treatment pH target. Treatment of Cd and Ni requires the treatment vessel to reach at least a pH of 10. To achieve the target pH of 10 the amount of neutralizing base input into the

treatment base would have to increase between 80% and 100%, compared to a target pH of 9.4.

The concentration of SO_4 only decreased slightly throughout the experiment. The solution remains slightly undersaturated in respect to gypsum, and the Ca concentration remained constant. It is likely that large amounts gypsum did not precipitate.

3.5.2 Implications

During lime treatment of mine impacted water, an important operational variable is the section of the target treatment pH. Contaminants are precipitated lime during water treatment by processes that consistently occur at narrow pH ranges. Therefore, the treatment plant can operate a different target pH, depending on the characteristics of the contaminant of concern. For instance, in laboratory conditions: Zn was removed at pH 9, most of the Fe at pH 6.5, Mn at pH 9.7, and Ni and Cd at pH above 10. Other variables affect the performance of mine impacted water treatment, but the metal solubility ranges are useful guiding concepts.

The water treatment plant influent mainly comes from the FPL, on occasions also blended with water from the tailings area. The intake pipe from the FPL is within the epilimnion, so changes to the water quality in this layer would affect the treatment processes in the plant. In 2021 the dissolved species in the pit-lake epilimnion increased and the pH decreased to 3.8. The lime consumption associated with higher dissolved metal concentrations and lower pH is expected to increase. In addition, the elemental concentrations of Cd, Ni, and Mn might become high enough that they become non-compliant for release. These elements require target treatment pH of 9 to 10.5, which is higher than the current operational pH. Increasing the target pH to 10 would increase the lime consumption and treatment process would need to be adapted to ensure compliance considering the increasing trend in Cd, Ni, Mn and other dissolved species.

Under lower pH conditions, higher quantities of metals can remain in solution. That was the case of increased Fe concentrations in the more acidic epilimnion. In 2021, 12% of

Fe was present as a reduced form Fe(II). As part of the treatment process, dissolved Fe(II) would have to be oxidated to Fe(III) before it can be removed from solution.

Adequate disposal of the precipitated solids from water treatment is necessary to avoid remobilization of contaminants at a mine site. The reactions that formed the precipitates during water treatment are reversible. Without proper disposal the solids that contained the contaminants during water treatment, may release metals back into the environment. The solids produced will likely redissolve if the Eh and pH values are lowered or reverted to the pre-treatment conditions.

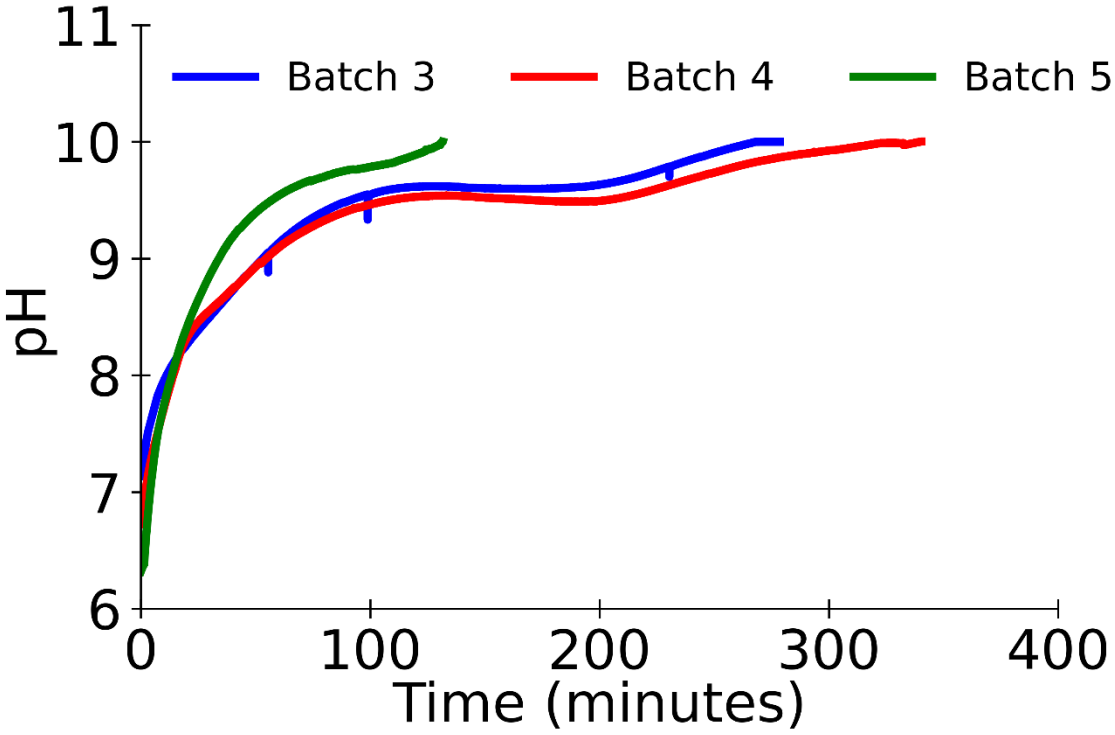

Figure 3.1 pH measurements for Faro Pit treatment batch experiment 3, 4, and 5.

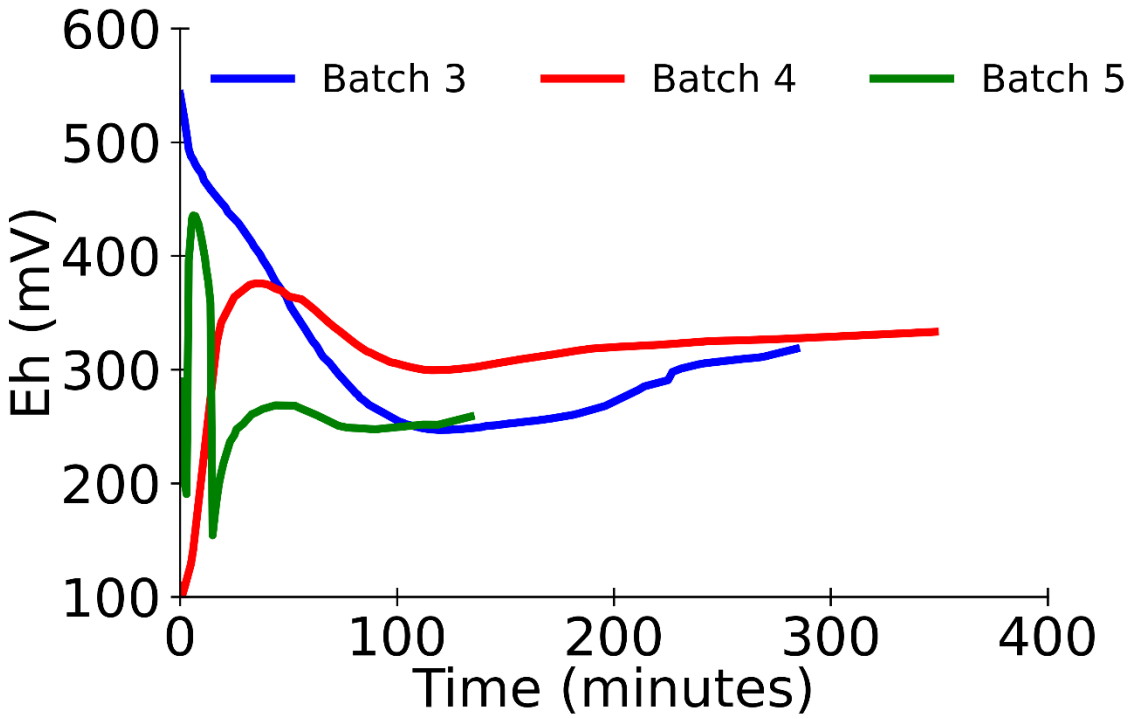

Figure 3.2 Redox potential expressed as Eh over time for the Faro Pit treatment batch experiment for replicate experiments 3 and 4.

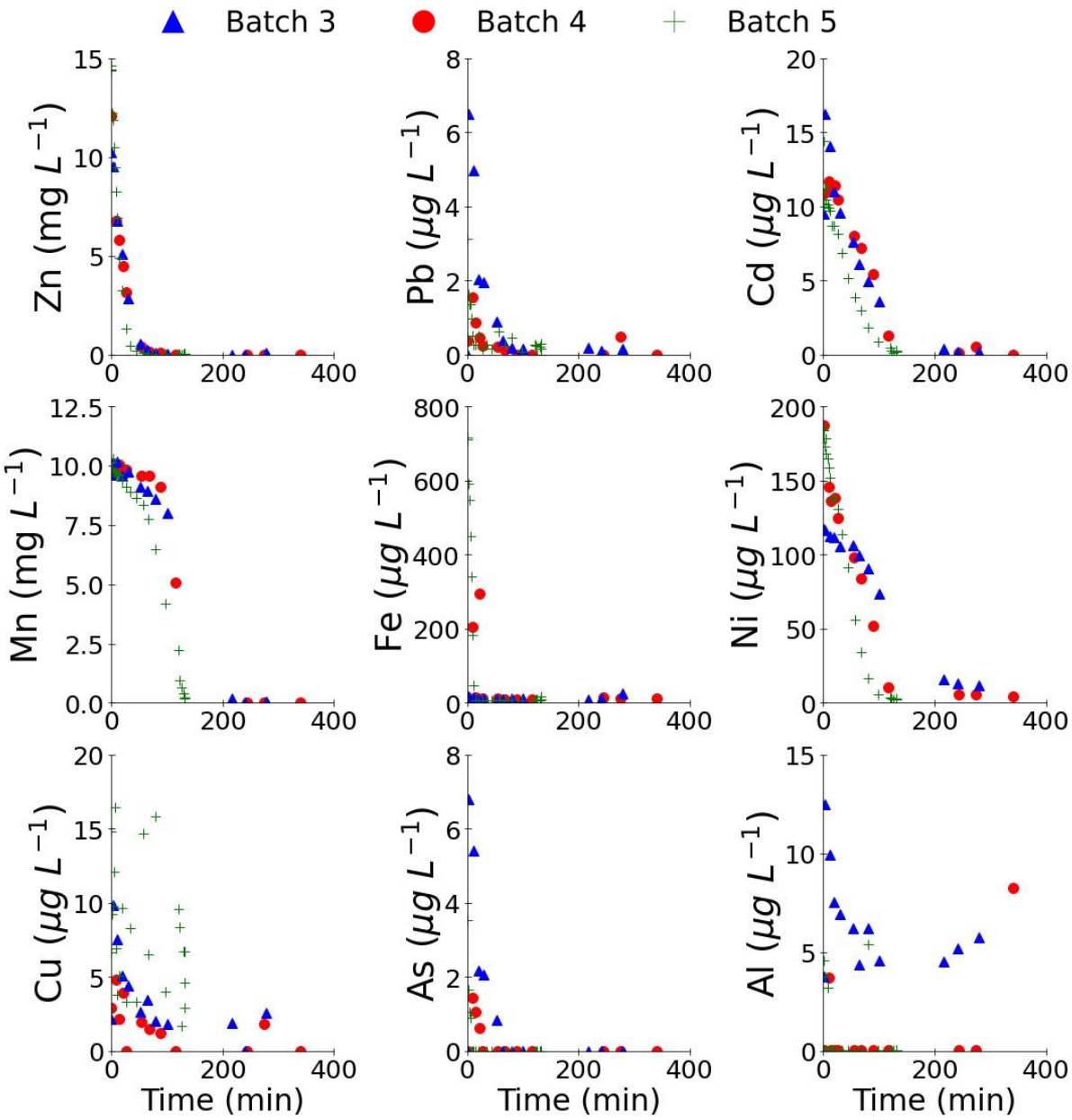

Figure 3.3a Dissolved elemental concentration over time for the Faro Pit treatment batch experiment for batches 3, 4, and 5.

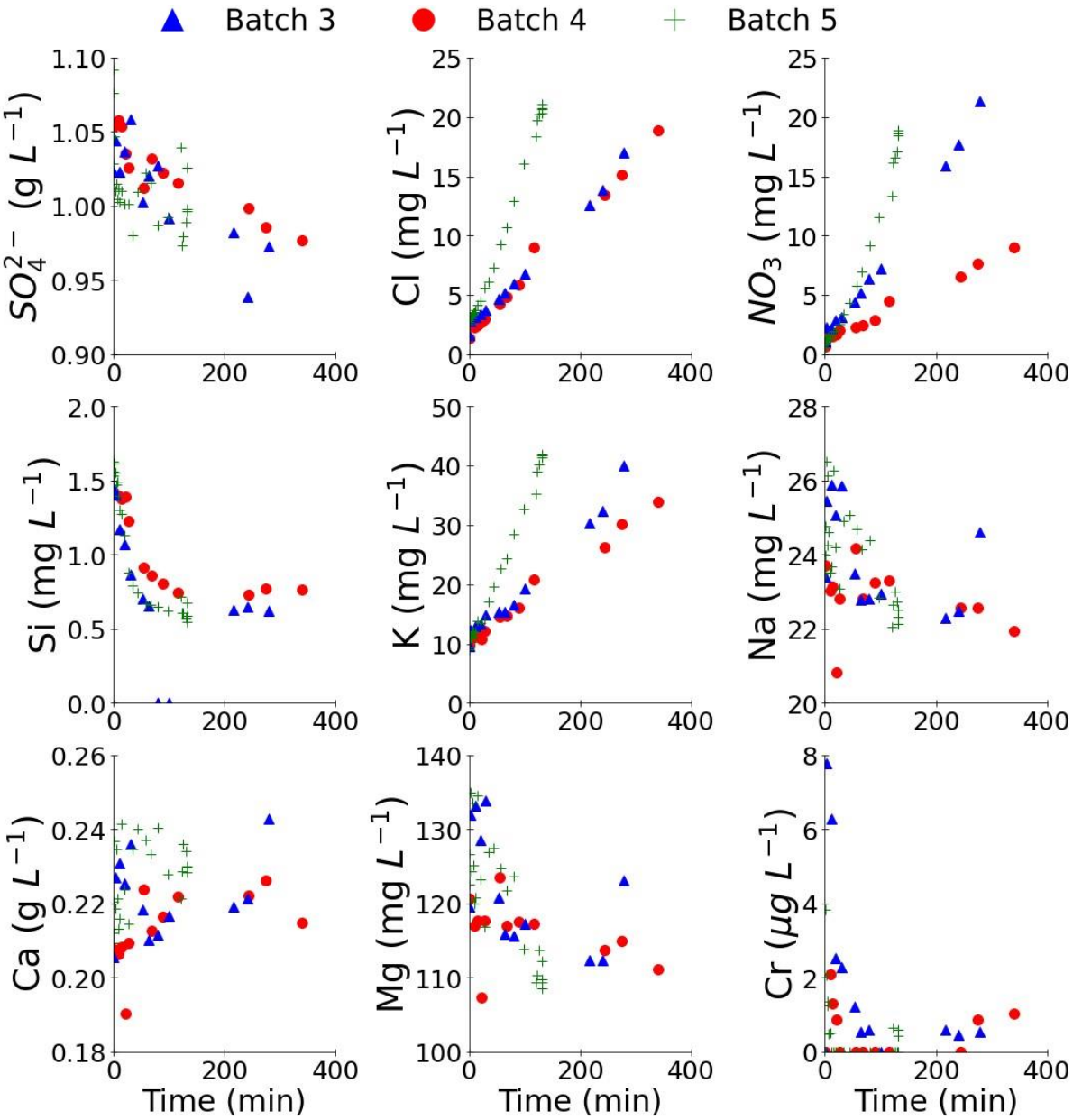

Figure 3.3b Dissolved elemental concentration over time for the Faro Pit treatment batch experiment for batches 3, 4, and 5.

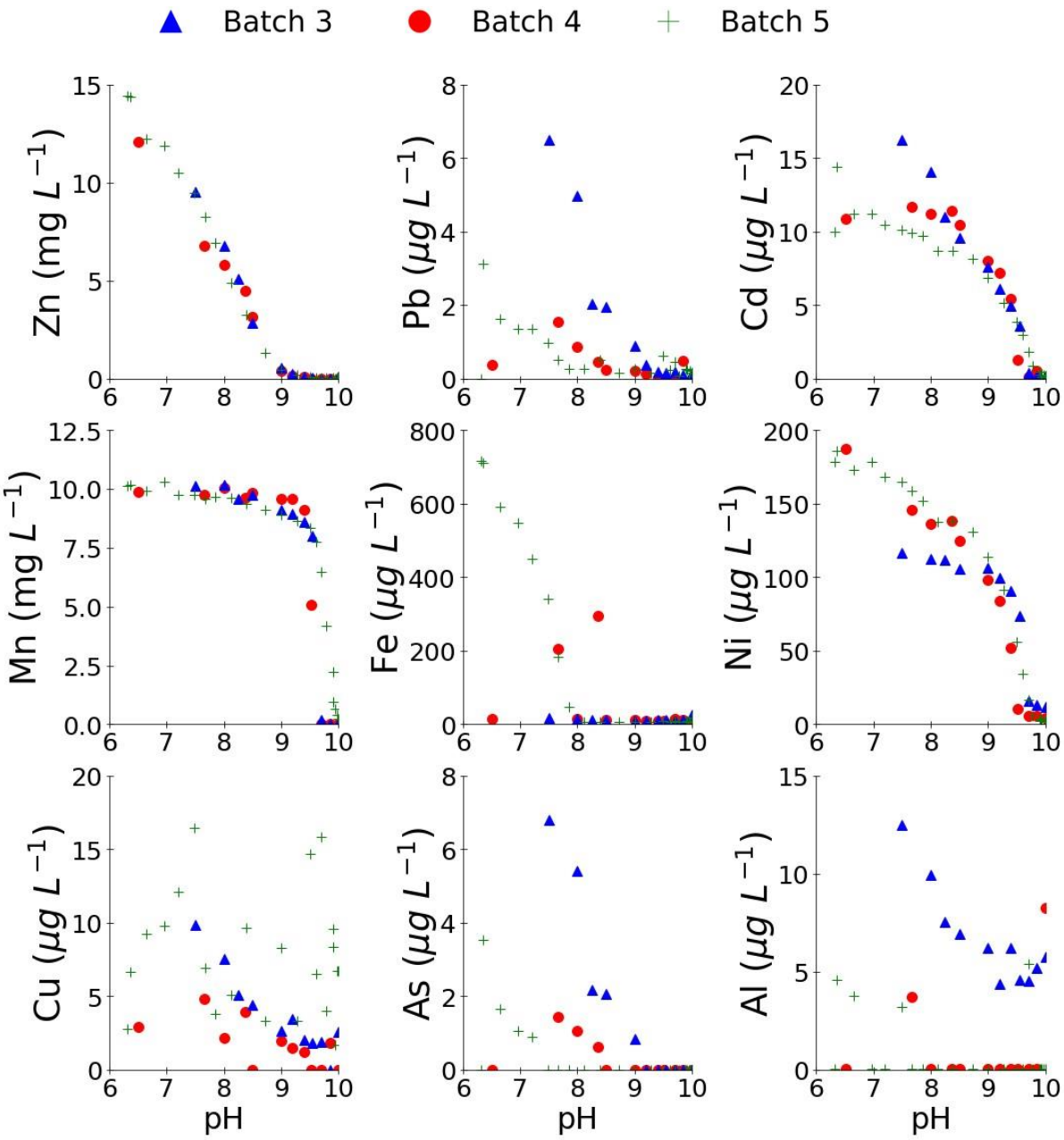

Figure 3.4a Dissolved elemental concentration as a function of pH for the Faro Pit treatment batch experiment for batches 3, 4, and 5.

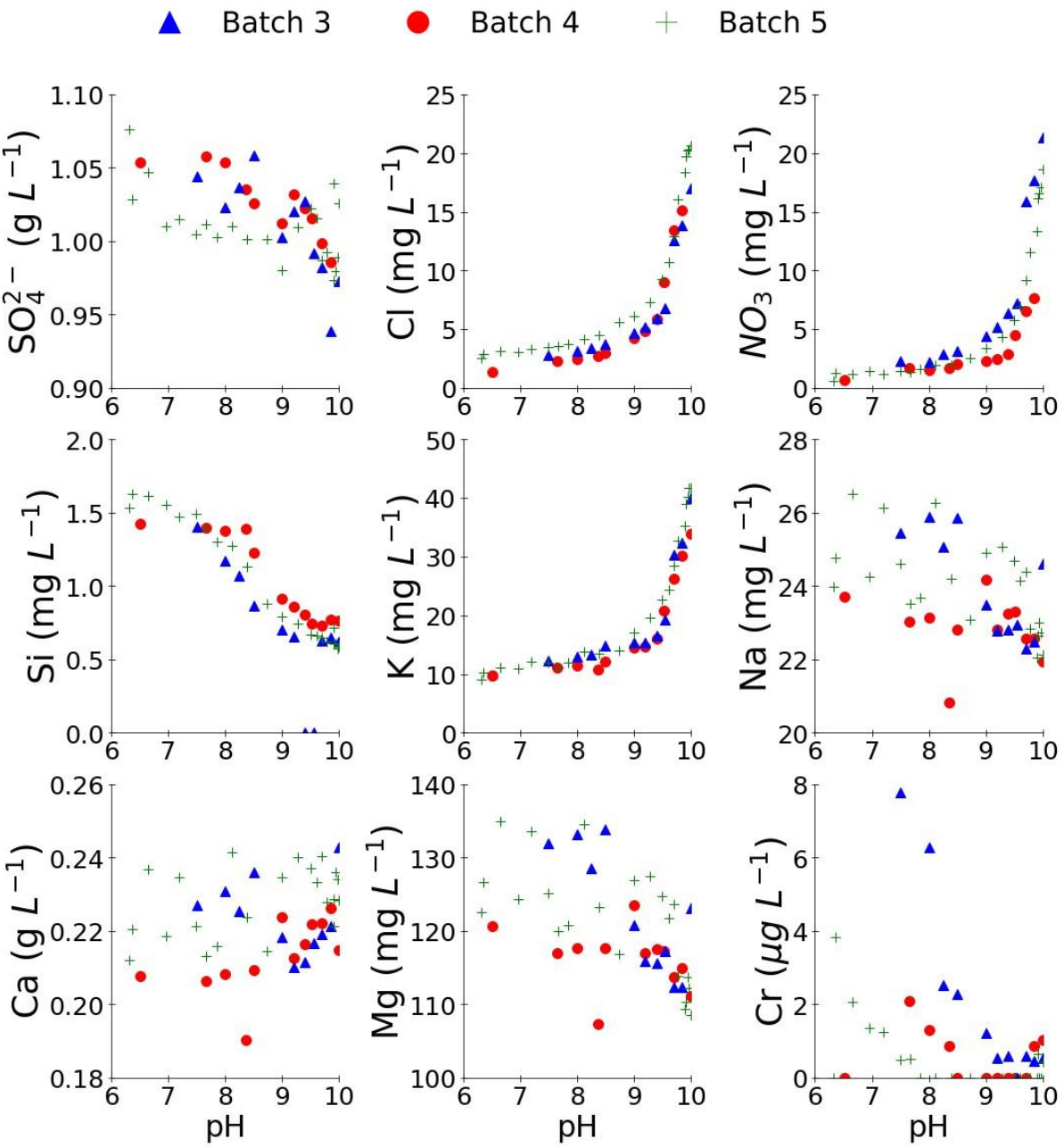

Figure 3.4b. Dissolved elemental concentration as a function of pH for the Faro Pit treatment batch experiment for batches 3, 4, and 5.

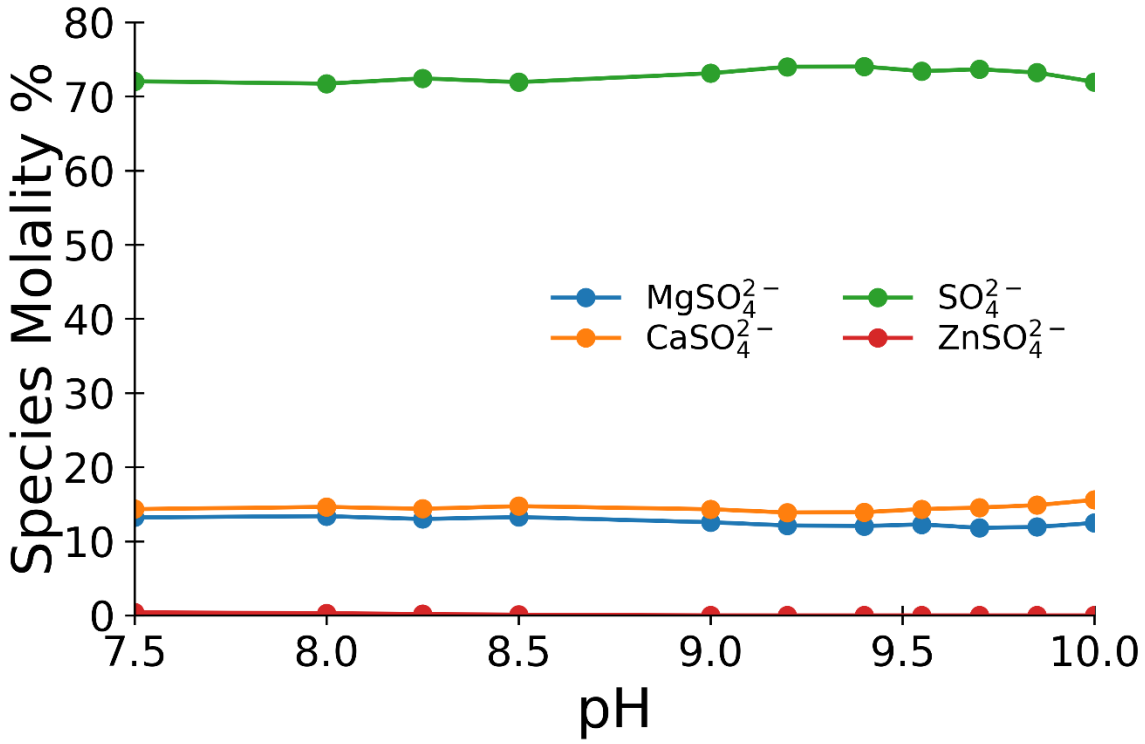

Figure 3.5 Concentration of sulfur species expressed as percentage of total sulfur concentration over time for Faro Pit treatment batch experiment 4

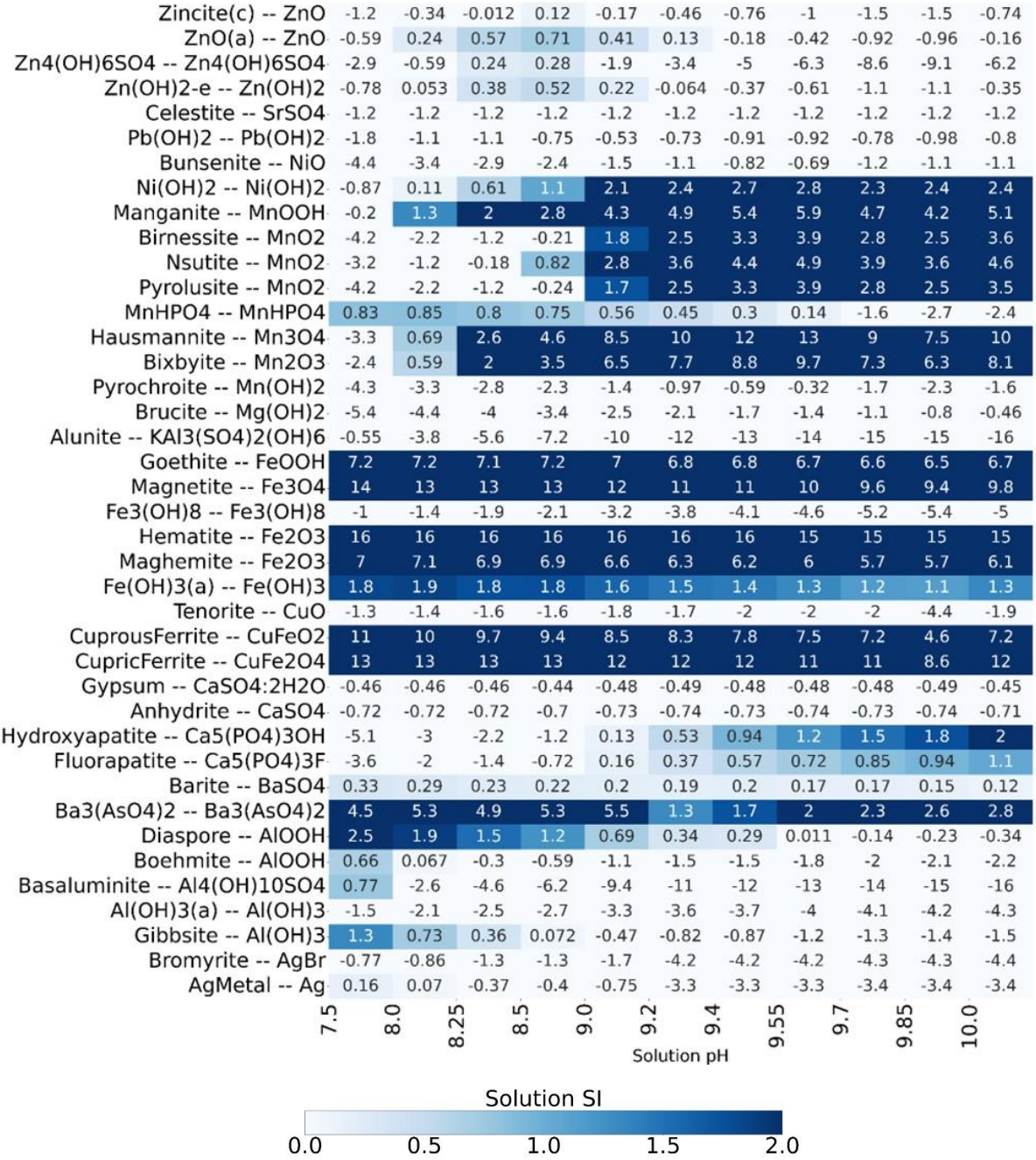

Figure 3.6 Crosstab of the mineral species and the batch experiment sample pH. The values show the saturation index (SI), and the shade of color highlights positive values as shown in the continuous scale. Only mineral species with SI values above -2 are included.

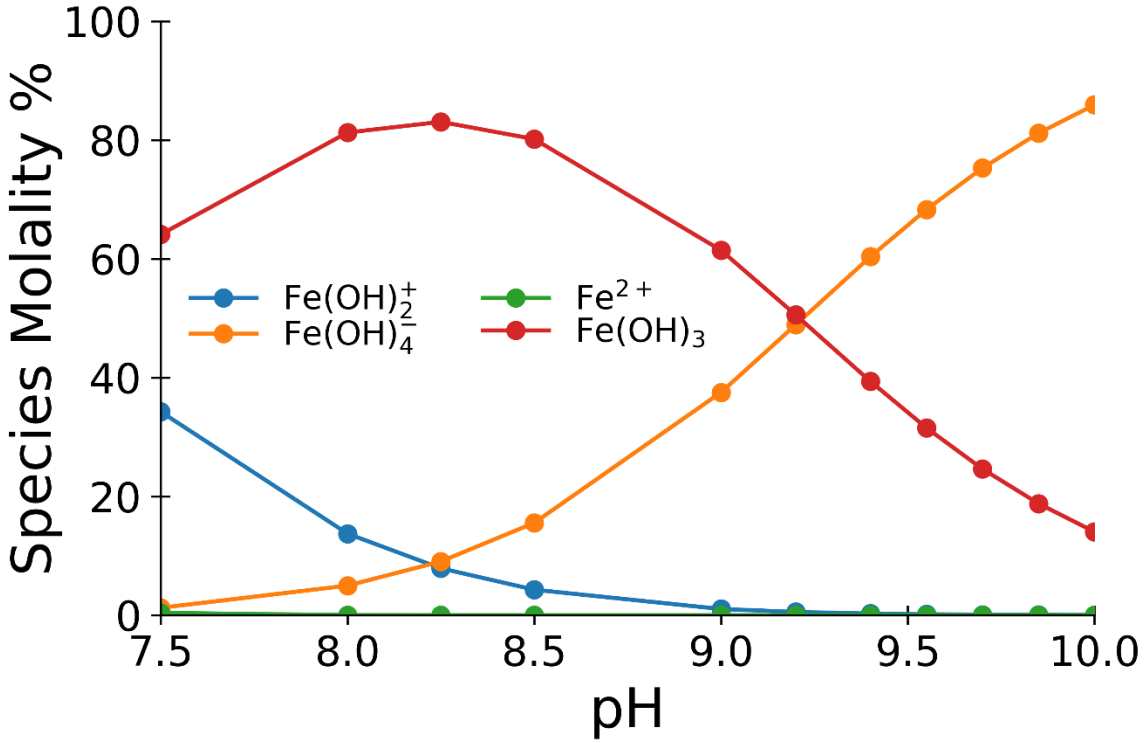

Figure 3.7 Concentration of iron species expressed as percentage of total iron concentration over time for Faro Pit treatment batch experiment 4

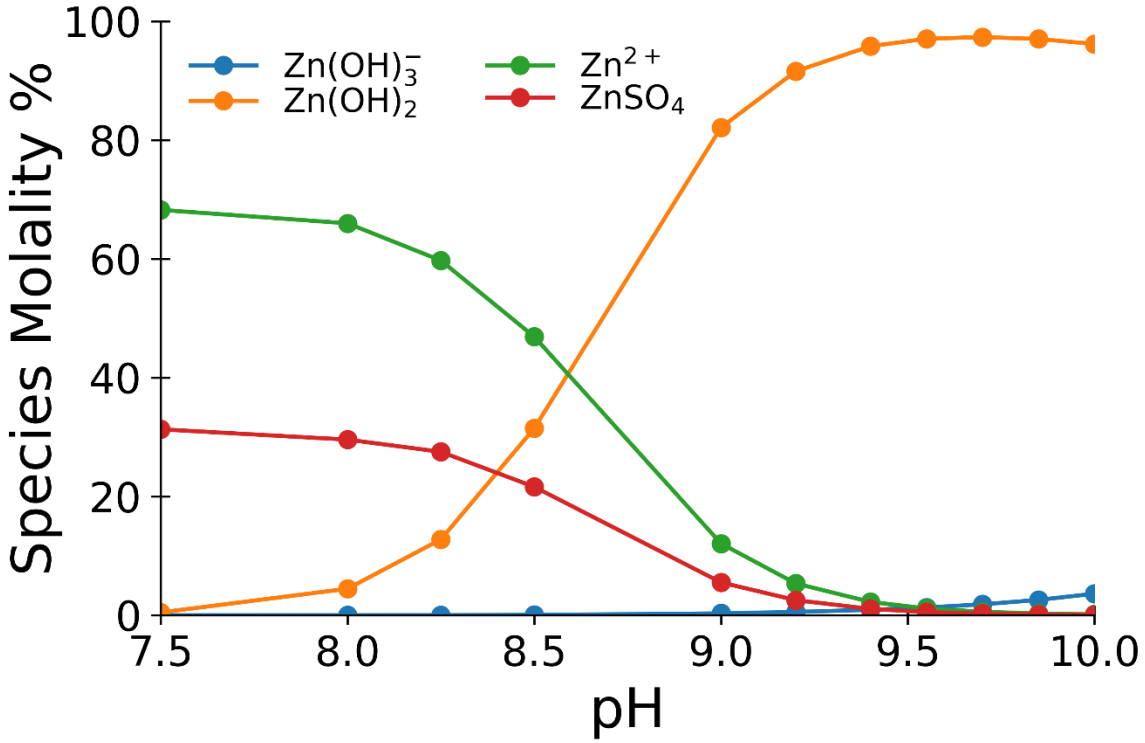

Figure 3.8 Concentration of zinc species expressed as percentage of total zinc concentration over time for Faro Pit treatment batch experiment 4.

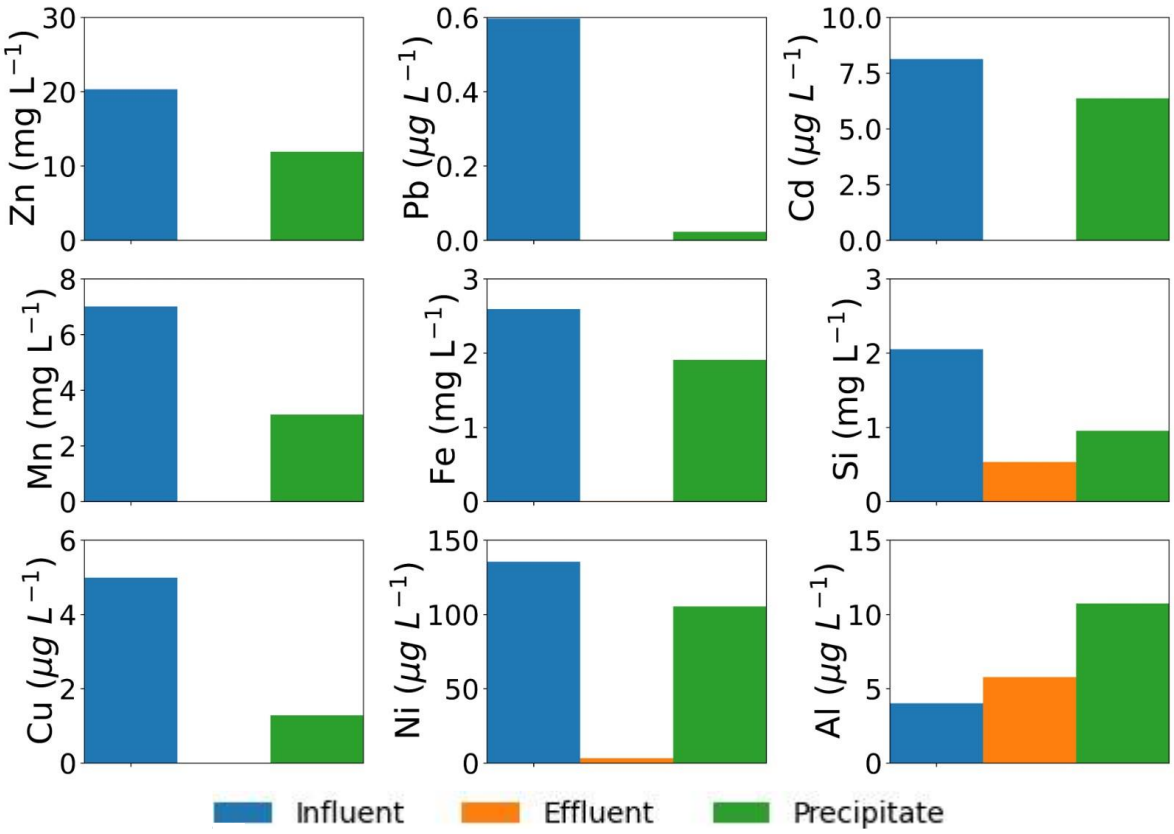

Figure 3.9a Element mass of elements in influent, effluent, and precipitate of the Faro Pit treatment batch experiment.

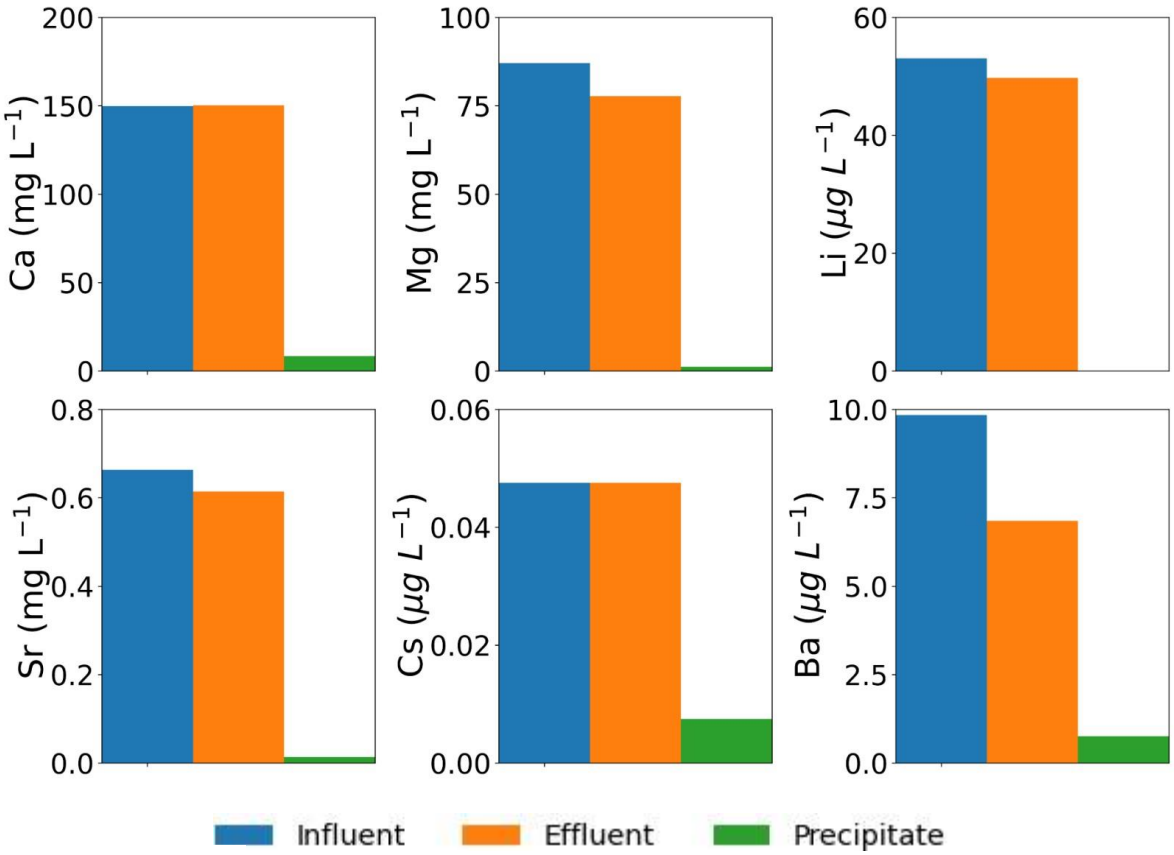

Figure 3.9b Element mass of elements in influent, effluent, and precipitate of the Faro Pit treatment batch experiment.

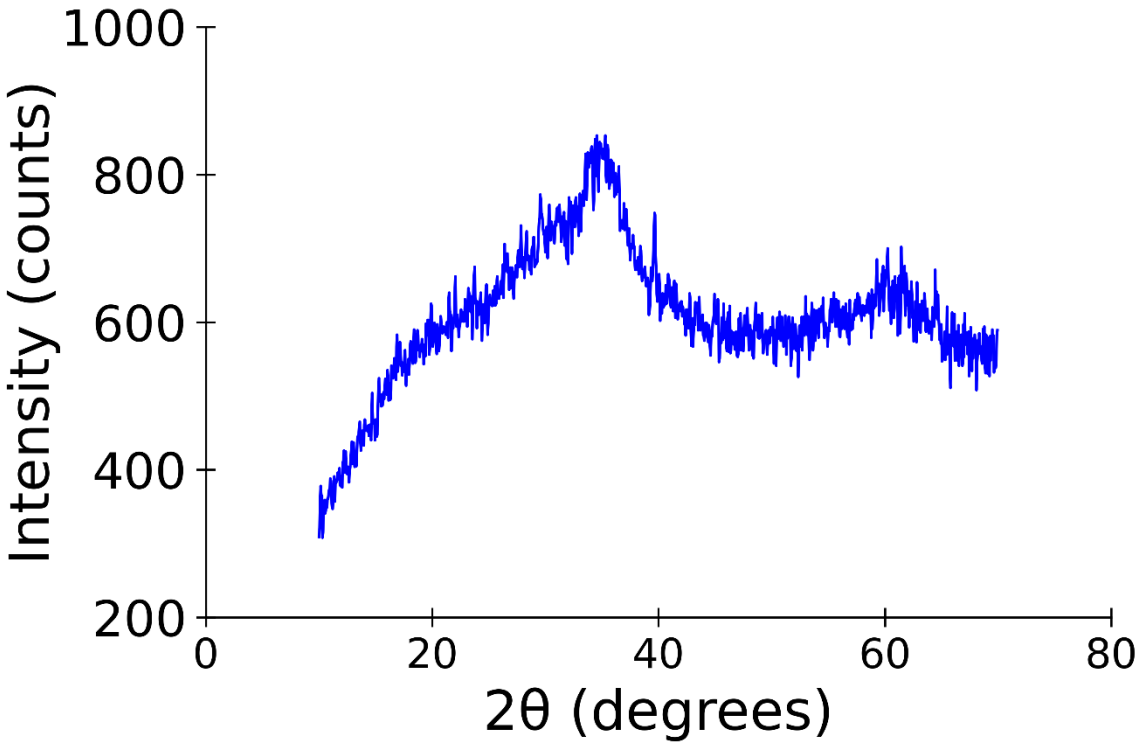

Figure 3.10 Powder X-ray diffraction (XRD) pattern of batch experiment precipitate solids.

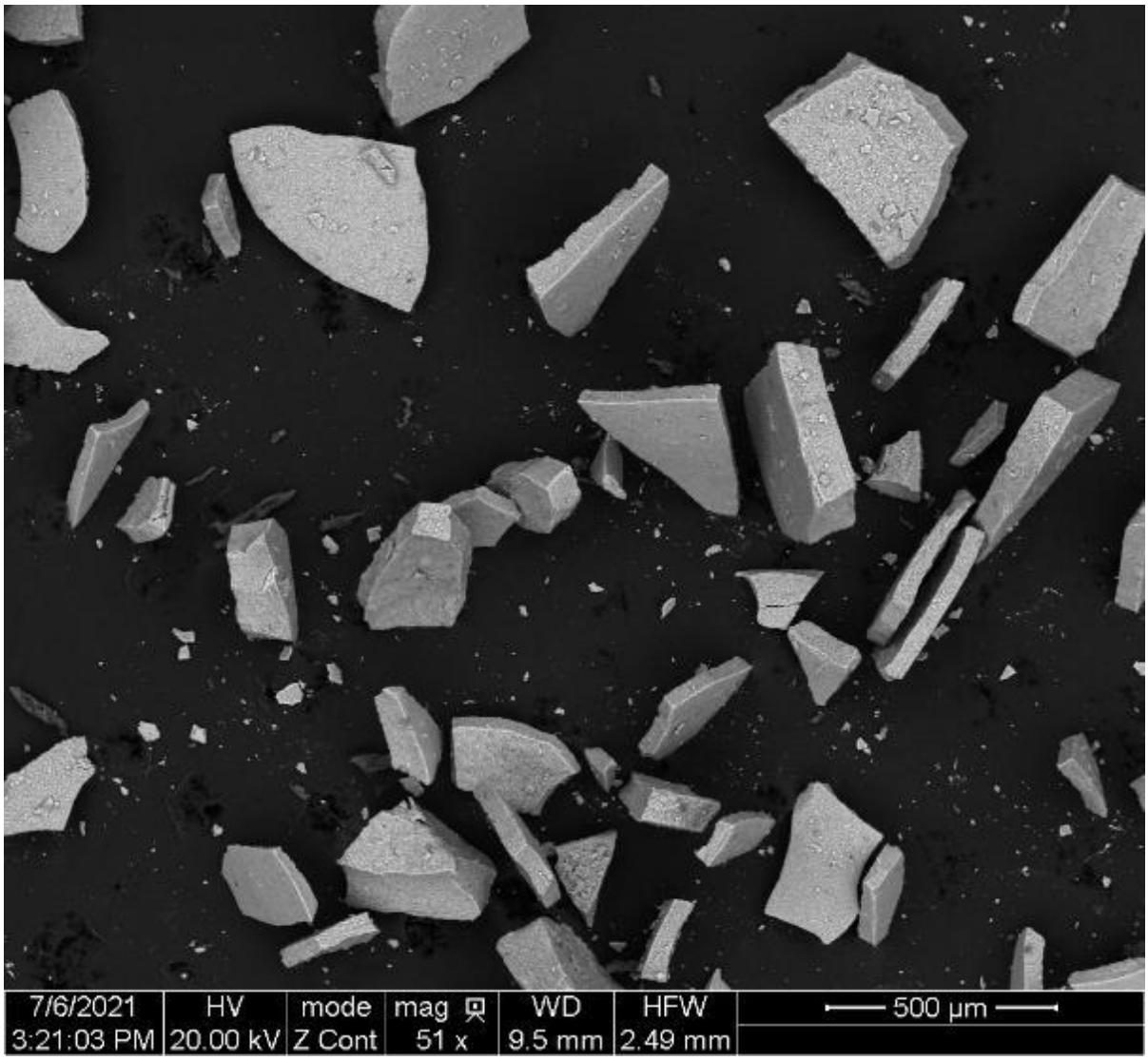

Figure 3.11 SEM photomicrograph of the precipitate obtained from batch experiment 6. The scale shows 500 µm.

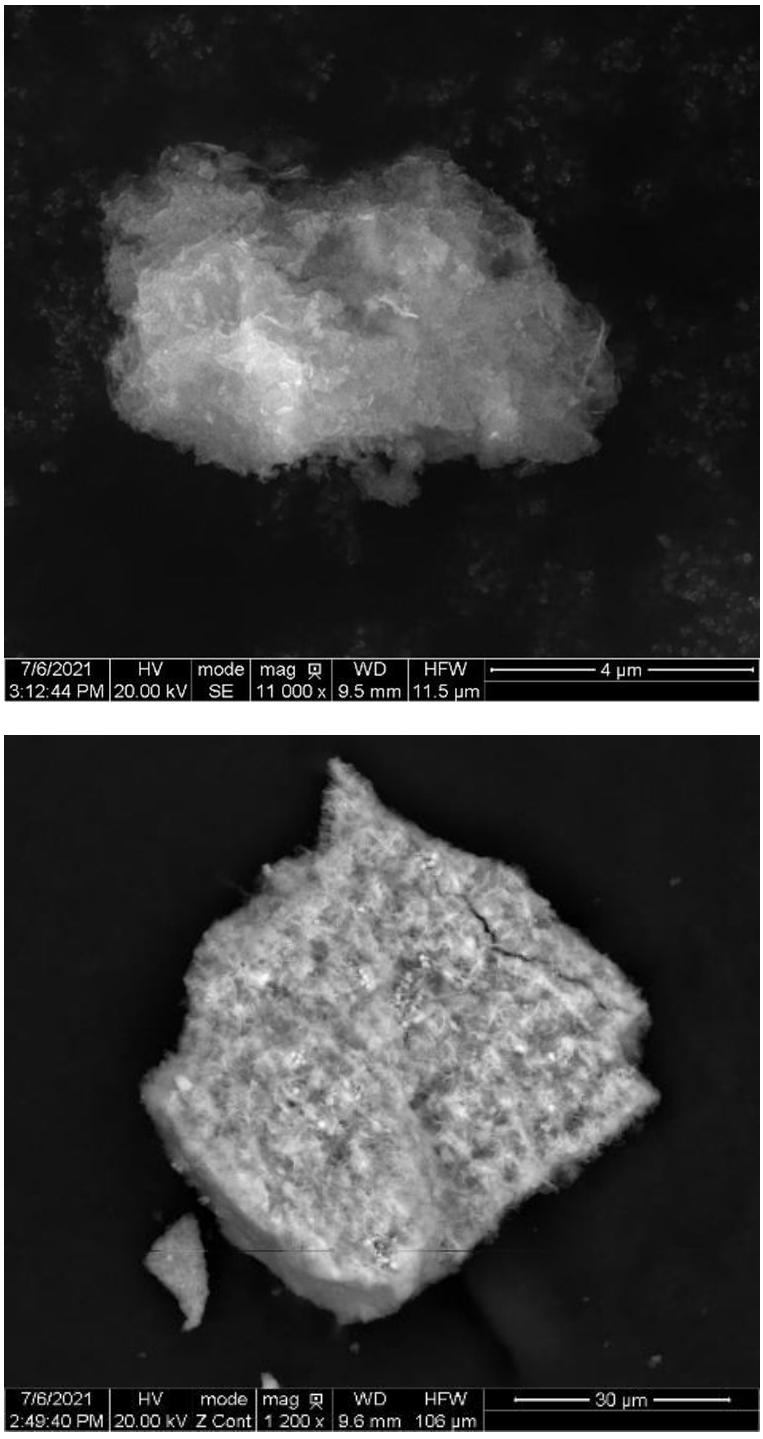

Figure 3.12 SEM photomicrograph of the precipitate obtained from batch experiment 6. Particles contain low Fe weight %.

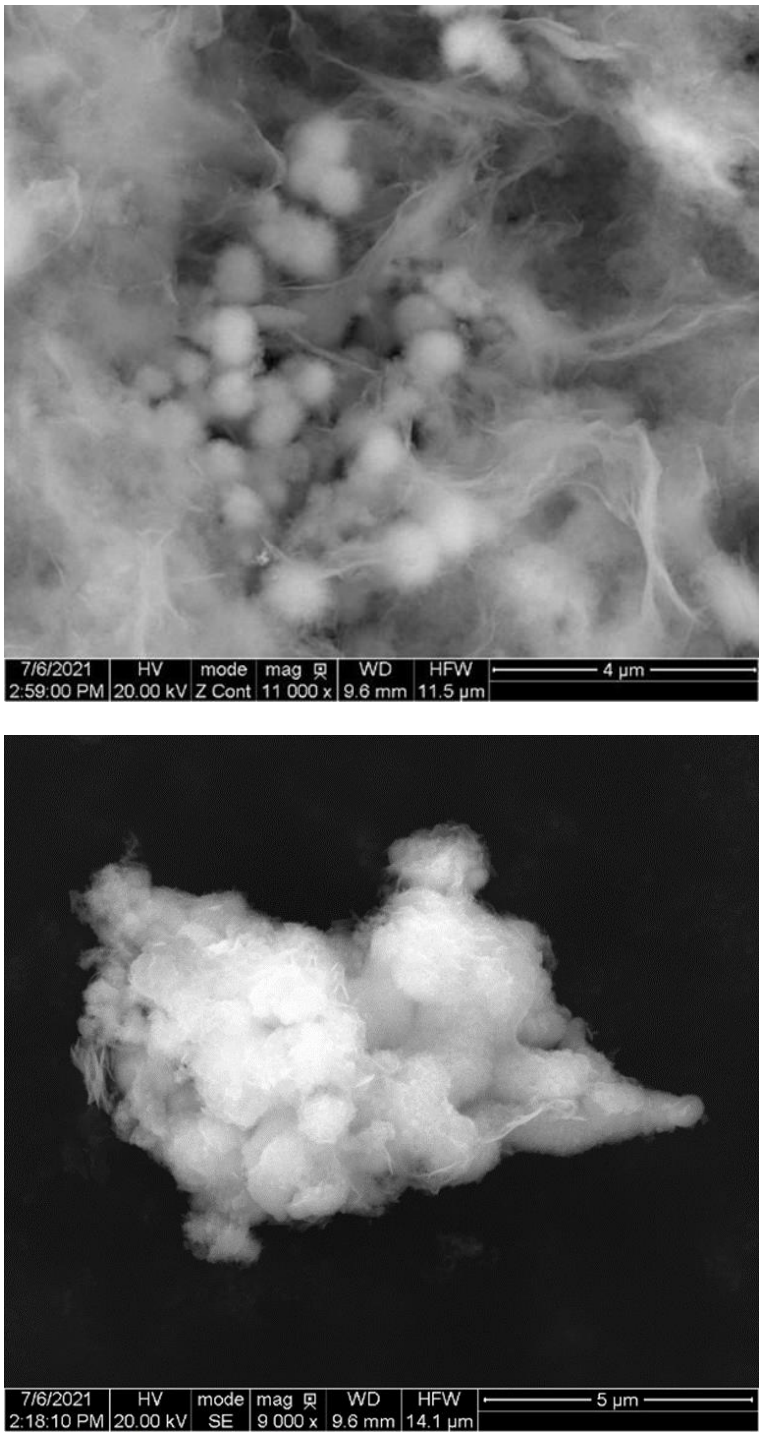

Figure 3.13 SEM photomicrographs of the precipitate obtained from batch experiment 6. Particles contain high Fe weight %.

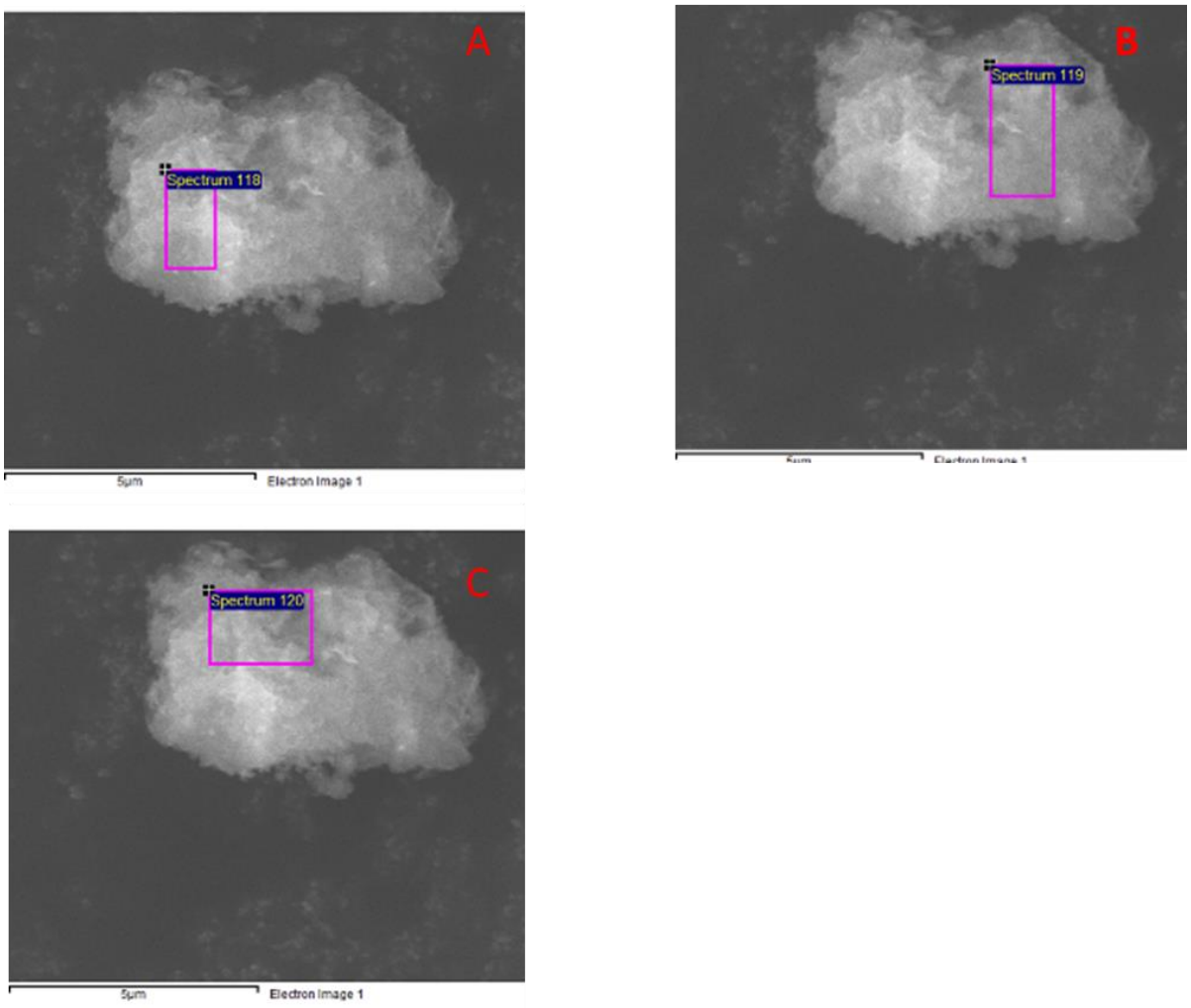

Element	Spectrum 109 (A)	Spectrum 110 (B)	Spectrum 111 (C)
O	33.27	39.56	42.89
Mg	2.36	3.57	3.33
Si	5.55	5.24	6.43
Ca	1.13	0.91	1.38
Mn	9.78	8.64	7.90
Zn	47.90	42.08	38.08

Figure 3.14 SEM-EDS photomicrograph of the precipitate obtained from batch experiment 6. The purple square is the section that was analyzed with the EDS. The table below corresponds to the EDS results, expressed as weight %. The scales show 5 µm.

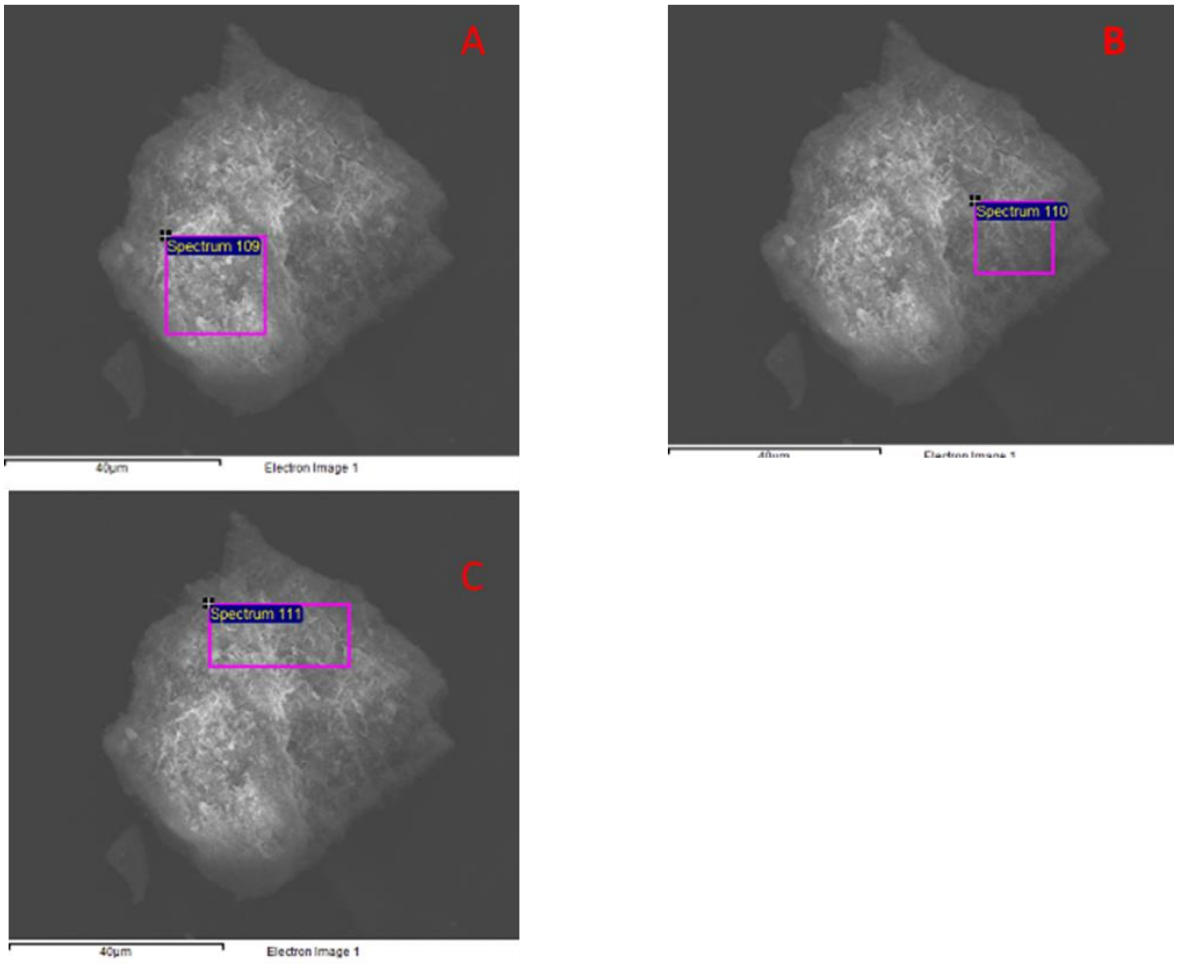

Element	Spectrum 109 (A)	Spectrum 110 (B)	Spectrum 111 (C)
O	37.81	35.69	38.14
Mg	3.97	3.12	3.79
Si	4.36	4.73	4.57
Ca	2.25	1.85	1.48
Mn	10.61	11.31	10.41
Fe	1.77	2.45	1.83
Zn	39.24	40.86	39.78

Figure 3.15 SEM-EDS photomicrograph of the precipitate obtained from batch experiment 6. The purple square is the section that was analyzed with the EDS. The table below corresponds to the EDS results, expressed as weight %. The scales show 40 µm.

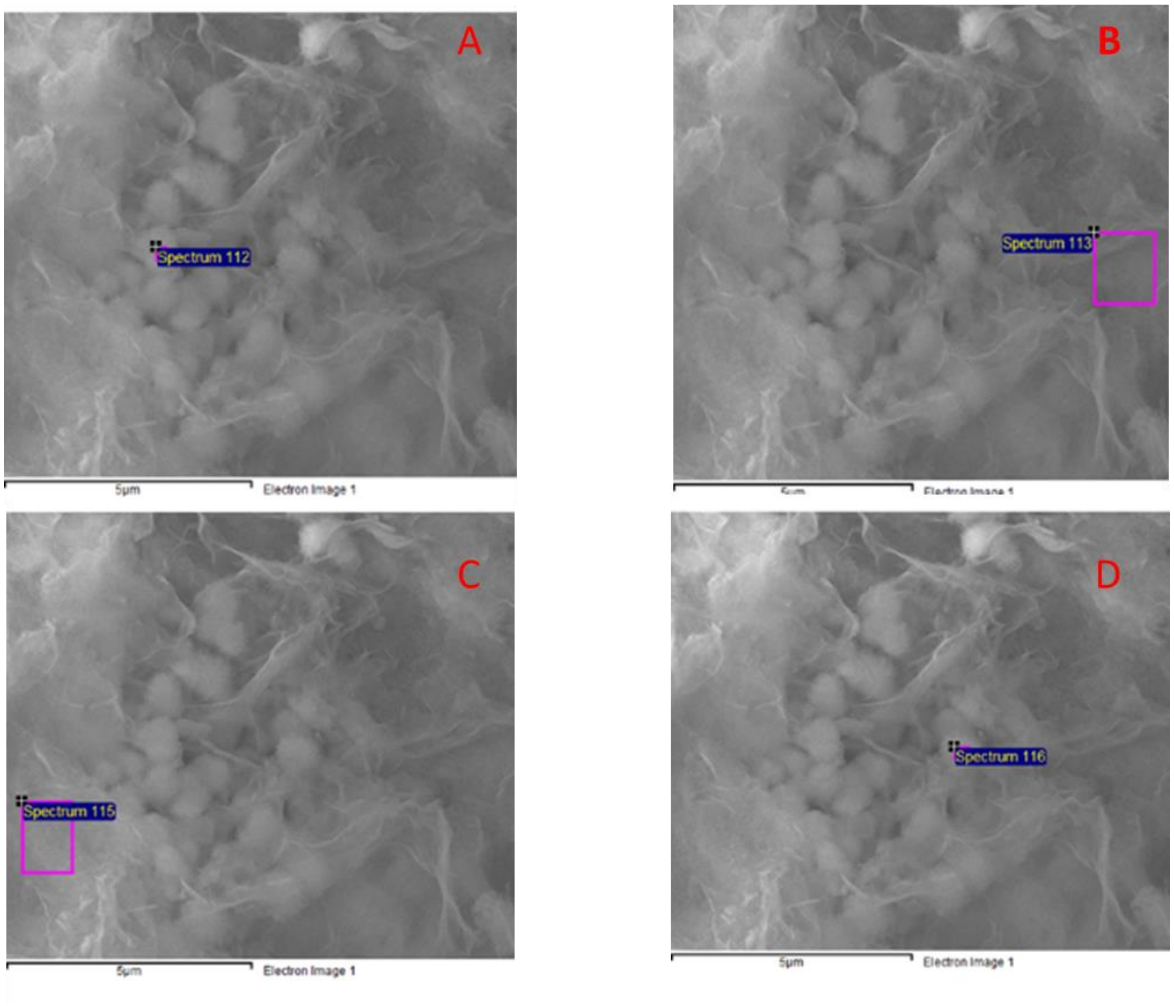

Element	Spectrum 112 (A)	Spectrum 113 (B)	Spectrum 115 (C)	Spectrum 116 (D)
O	44.60	34.80	41.42	44.33
Mg	3.11	3.31	3.78	2.41
Si	4.15	4.78	4.56	4.13
Ca	0.88	1.25	1.11	0.97
Mn	5.20	10.99	9.81	4.81
Fe	17.83	3.12	4.69	20.46
Zn	24.24	41.73	34.64	22.89

Figure 3.16 SEM-EDS photomicrograph of the precipitate obtained from batch experiment 6. The purple square is the section that was analyzed with the EDS. The table below corresponds to the EDS results, expressed as weight %. The scales show 5 µm.

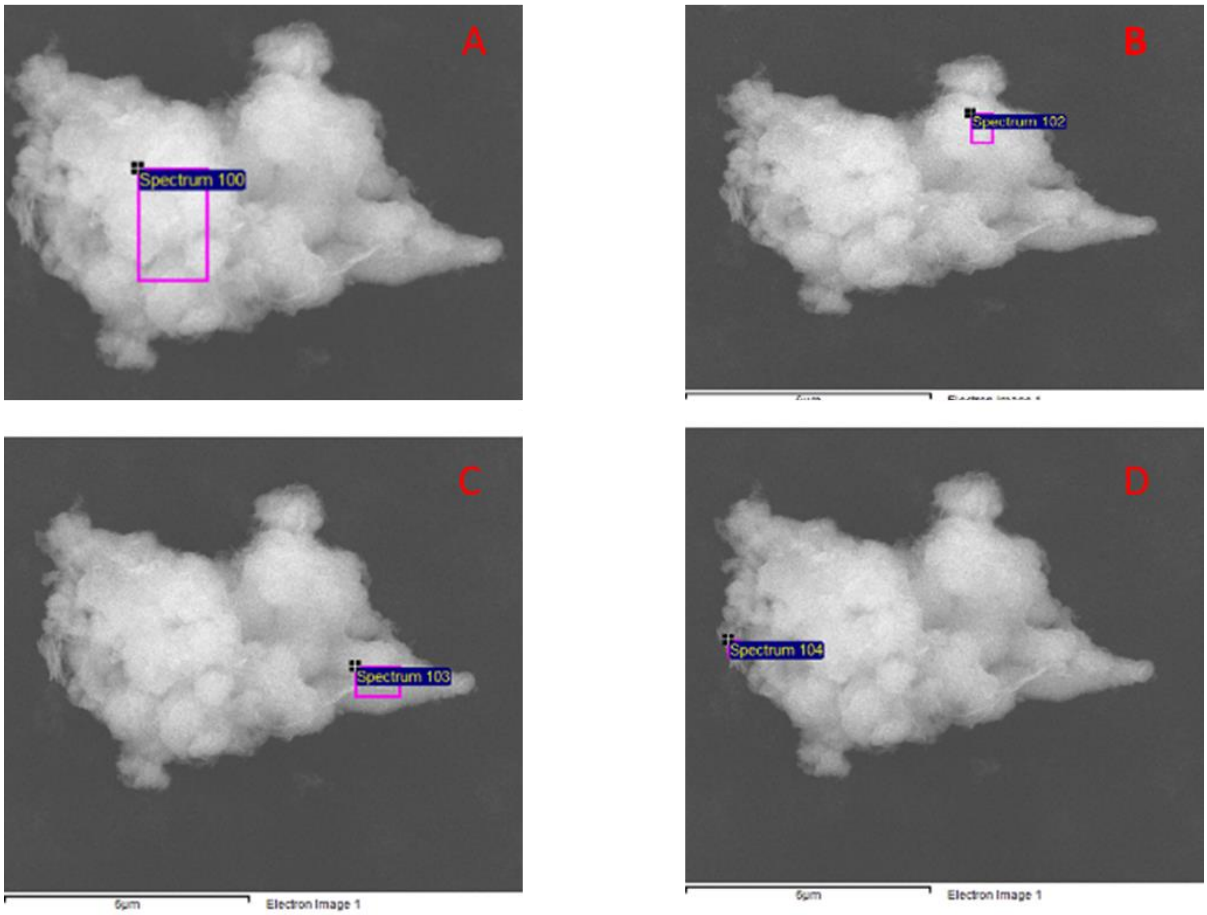

Element	Spectrum 100 (A)	Spectrum 102 (B)	Spectrum 103 (C)	Spectrum 104 (D)
O	39.34	45.23	43.35	32.51
Si		3.69	3.31	1.69
Ca	0.85	1.09	1.04	1.04
Mn	2.82	1.71	1.83	1.99
Fe	35.65	31.96	32.89	13.82
Zn	21.33	16.33	17.58	48.94

Figure 3.17 SEM-EDS photomicrograph of the precipitate obtained from batch experiment 6. The purple square is the section that was analyzed with the EDS. The table below corresponds to the EDS results, expressed as weight %. The scales show 5 µm.

Table 3.1 Experimental design of batch tests 1 and 2. The water sources column describe the blend ratio of water from the FPL and CVP used for the experiment.

Water Source	**Treatment**	**$Ca(OH)_2$ added (g)**	**End Solution pH**
Faro Pit	Target pH 10	0.08	9.85
Faro Pit	Excess Lime	1.7	12.9
Faro Pit	No Lime	0	6.7
Faro Pit : CVP (8:2)	Target pH 10	0.08	9.85
Faro Pit : CVP (8:2)	Excess Lime	1.7	12.9
Faro Pit : CVP (8:2)	No Lime	0	6.7
Ultrapure water	Excess Lime	1.7	12.9
Ultrapure water	No Lime	0	7

Table 3.2 Experimental details for batch experiments 3, 4, 5, and 6. Geochemical characteristics and treatments of the solution used for the experiments.

	Initial pH	Initial Zn (mg L^{-1})	Initial Fe (μg L^{-1})	Added $FeSO_4$ (m)
Batch 3	7	10.26	16.93	0
Batch 4	6.75	12.11	205.6	0.0020
Batch 5	6.31	14.4	716.8	0.0020
Batch 6	6.86	12.6	723.3	0.0020

Table 3.3 Experimental details for batch experiments 3, 4, 5, and 6. Test design details

	Initial solution volume (mL)	Final solution volume (mL)	Number of samples	Dosing rate (mL of base/ hr)
Batch 3	500	383	21	5.5
Batch 4	700	240	23	5.5
Batch 5	500	60	41	5.5
Batch 6	770	725	9	16.1

Table 3.4 Experimental details for batch experiments 3, 4, 5, and 6. Test design details

Sample #	Batch 3 Sample pH	Batch 4 Sample pH	Batch 5 Sample pH	Batch 6 Sample pH
1	7.5	7.66	6.36	7.01
2	8	8	6.65	8.04
3	8.25	8.365	6.96	9.25
4	8.5	8.5	7.20	9.86
5	9	9	7.49	7.01
6	9.2	9.2	7.67	8.04
7	9.4	9.4	7.85	9.25
8	9.55	9.52	8.12	9.86
9	9.7	9.7	8.39	10
10	7.5	9.85	6.36	
11	8	10	6.65	
12	8.25	6.75	6.96	
13	8.5	7.66	7.20	
14	9	8	7.49	
15	9.2	8.365	7.67	
16	9.4	8.5	7.85	
17	9.55	9	8.12	
18	9.7	9.2	8.39	
19	9.85	9.4	8.73	
20	9.85	9.52	8.73	
21	10	9.7	9.00	
22		9.85	9.28	
23		10	9.50	
24			9.61	
25			9.70	
26			9.78	
27			9.90	
28			9.91	
29			9.94	
30			9.98	
31			9.00	
32			9.28	
33			9.50	
34			9.61	
35			9.70	
36			9.78	
37			9.90	
38			9.91	
39			9.94	
40			9.98	
41			10	

Chapter 4:

Conclusions and Recommendations

Contaminated water management at an abandoned mine can be challenging. Conveyance, storage, and treatment of variable water volumes and concentrations requires an adaptable and robust system. In addition, continued release of acid rock drainage (ARD) and metal leaching (ML) can increase the load of metal, metalloid, and sulfate that need to be stored and treated. Survey of FPL showed that thermal stratification can affect the distribution of contaminants, and therefore the input to the water treatment plant. Load-balance calculations increased the understanding of the load inputs into the pit lake, and how concentrations of elements of interest changed over time. Treatment batch experiments helped to characterize the removal mechanisms that control precipitation of dissolved metals from treatment influent water.

The FPL was sampled in two separate occasions, in September 2019 and September 2021. A sampling apparatus was installed to collect depth discreate samples from southwest area of the pit lake, while standing on the shore. The results from both sampling events showed that the pit lake was thermally stratified in the fall months. The average temperature of the epilimnion was 10 ºC and hypolimnion was 4 ºC. The temperature difference was caused because the epilimnion was in thermal contact with the atmosphere, while the hypolimnion has limited heat propagation. The difference in density of water at 10 ºC and 4 ºC caused seasonal stratification in the pond. The thermocline depth fluctuates between 8 m and 10 m depth, likely caused by wind-driven internal waves. The TDS vertical profile in the pit lake was marked by a sharp boundary at the same depth as the thermocline. Similarly, concentrations of multiple dissolved species showed a sharp transition at the thermocline. Temperature stratification in the pit lake limits water mixing between the top and bottom layer. Water discharged into the epilimnion remained in that layer, resulting in an epilimnion geochemically distinct from the remainder of the lake.

The pH of the FPL was circumneutral in 2019, with slightly higher values in the epilimnion, on average pH 6.7. In 2021, the pH of the epilimnion (4.0) was lower than the

hypolimnion (5.8). The concentration depth profile of many dissolved species were marked by a sharp contrast that corresponds with the depth of the thermocline. In 2019, dissolved Fe, Zn, and Mn concentrations were higher in the hypolimnion than in the epilimnion, whereas the concentrations of these elements were higher in the epilimnion in 2021. Concentration of Pb in the epilimnion increased by two orders of magnitude between 2019 to 2021. Concentrations of Cd in the pit-lake epilimnion are 70% higher in 2021 compared to 2019.

The waste-rock leachate and the IP were the largest load inputs to the FPL, despite having lower contaminant concentrations than other sources. Between 2020 and 2021, Fe loading to the FPL doubled mainly due to additional loads sourced from IP. The annual Mn load into the pit lake increased by 150% between 2018 and 2020, also sourced from IP. The loading of Ni, Zn, and Cd into the pit increased by 100%, driven by the combination of loads from the IP, S-Wells, and waste-rock seepage. The load from waste-rock leachate to the FPL increased by a factor of two for Fe, Zn, and Ni and by a factor of four for Cd.

In batch experiments, a sample of FPL hypolimnion water was placed in a stirred cell reactor (SCR) and dosed with a calcium hydroxide solution. The addition of $Ca(OH)_2$ solution increased the pH to the final target pH of 10. This batch experiment replicated the geochemical processes that are used at the FMC for treatment of mine impacted water. Samples were collected at specific time and pH intervals from the SCR to characterize pH-dependent processes. The solution pH and Eh increased rapidly from the start of the batch experiment. The Eh trended towards 320 mV over time. The pH increased to a plateau between 9.2 -9.5 within the first 100 minutes of the experiment, with little change for the second half of the experiment.

Batch experiments indicated that contaminant removal processes at the FPL were pH-dependent, and precipitation occurs within a narrow pH and Eh range. Dissolved Fe was removed from solution within the first 5 minutes of the experiment, removal occurred at the starting pH (6.3) and reached a minimum concentration at pH 8.0. The speciation modeling shows that Fe precipitated as amorphous $Fe(OH)_3$ minerals. Half of the Zn loading in solution was removed at the start of the experiment, concurrently with Fe. The remaining Zn was removed between pH 8.0 and 9.0. The concentration of Mn remained constant during the

experiment until the solution pH reached 9.5-9.7, at which point Mn precipitation occurred at an exponential rate. Concentrations of Ni and Cd decreased at a constant rate from the start of the experiment until the reaction vessel reached pH 10. There was limited removal of SO_4 and the solution remained undersaturated in respect to gypsum.

XRD analysis showed that precipitated solids obtained from the batch experiment were predominantly amorphous internal structures. Characterization of the precipitate with SEM-EDS showed that Fe and Zn coprecipitated in the initial stage of the experiment. Between pH 8 and 9.4, amorphous Zn hydroxides and Mn-oxides were co precipitated, with no observed Fe co precipitation..

The findings of this study indicates that additional load sources captured and conveyed to the FPL can change the distribution of contaminants within the pit-lake. Operational decisions that increased load inputs to the pit lake altered long-term trend of lower TDS in the lake epilimnion. Load-balance calculations were useful to evaluate the effect of future or past changes to the contaminant distribution on site. Load-balance calculations into a pit lake should include the flow and concentration of inputs, and also the depth at which the water is discharged. This study increased the understanding of the processes that contribute to the efficient removal of contaminants from mine-impacted water. The water treatment processes assessment was tied to the characterization of the contaminant distribution in the pit lake. With deteriorating water quality in the treatment influent, the treatment requirements will change. Sludge production, target pH, and residence time requirements increased with higher ARD load water inputs into the treatment process.

References

Amos, R. T., Blowes, D. W., Bailey, B. L., Sego, D. C., Smith, L., & Ritchie, A. I. M. (2015). Waste-rock hydrogeology and geochemistry. *Applied Geochemistry*, *57*, 140–156. https://doi.org/10.1016/j.apgeochem.2014.06.020

Aubé, B., & Lee, D. (2015). The High Density Sludge (HDS) Process and Sulphate Control. *International Conference on Acid Rock Drainage and IMWA 2015*.

Aubé, B. C., & Zinck, J. M. (1999). Comparison of AMD treatment processes and their impact on sludge characteristics. *Proceedings for Sudbury*, *99*, 261–270.

Aubé, B., & Zinck, J. (2003). Lime Treatment of Acid Mine Drainage in Canada. *Proceedings Brazil-Canada Seminar on Mine Rehabilitation*.

Bao, Z., Bain, J., Holland, S. P., Wilson, D., MacKenzie, P., Ptacek, C. J., & Blowes, D. W. (2020). Faro Waste Rock Project: Characterizing Geochemical Heterogeneity in Sulfide- and Carbonate-Rich Waste Rock. *Applied Geochemistry*, 104691. https://doi.org/10.1016/j.apgeochem.2020.104691

Bao, Z., Bain, J., Holland, S. P., Wilson, D., Ptacek, C. J., & Blowes, D. W. (2022). Hydrogeochemical response of a variably saturated sulfide-bearing mine waste-rock pile to precipitation: A field-scale study in the discontinuous permafrost region of Northern Canada. *Water Resources Research*, e2021WR031082.

Bao, Z., Blowes, D. W., Ptacek, C. J., Bain, J., Holland, S. P., Wilson, D., Wilson, W., & MacKenzie, P. (2020). Faro Waste Rock Project: Characterizing Variably Saturated Flow Behavior Through Full-Scale Waste-Rock Dumps in the Continental Subarctic Region of Northern Canada Using Field Measurements and Stable Isotopes of Water. *Water Resources Research*, *56*(3). https://doi.org/10.1029/2019WR026374

Blowes, D. W., Ptacek, C. J., Jambor, J. L., Weisener, C. G., Paktunc, D., Gould, W. D., & Johnson, D. B. (2014). The Geochemistry of Acid Mine Drainage. In *Treatise on Geochemistry* (pp. 131–190). Elsevier. https://doi.org/10.1016/B978-0-08-095975-7.00905-0

Boehrer, B., Kiwel, U., Rahn, K., & Schultze, M. (2014). Chemocline erosion and its conservation by freshwater introduction to meromictic salt lakes. *Limnologica*, *44*, 81–89. https://doi.org/10.1016/j.limno.2013.08.003

Boehrer, B., & Schultze, M. (2008). Stratification of lakes. *Reviews of Geophysics*, *46*(2), RG2005. https://doi.org/10.1029/2006RG000210

Campble Scientific. (2014). Model 109SS Temperature Probe. Logan, Utah.

Castendyk, D. N., Balistrieri, L. S., Gammons, C., & Tucci, N. (2015). Modeling and management of pit lake water chemistry 2: Case studies. *Applied Geochemistry*, *57*, 289–307. https://doi.org/10.1016/j.apgeochem.2014.09.003

Castendyk, D. N., Eary, L. E., & Balistrieri, L. S. (2015). Modeling and management of pit lake water chemistry 1: Theory. *Applied Geochemistry*, *57*, 267–288. https://doi.org/10.1016/j.apgeochem.2014.09.004

Chermak, J. A., Wielinga, B., Taylo, J. r, & Wyatt, G. (2004). Cost-effective Acid Rock Drainage Water Treatment Applied to Mining-Impacted Watersheds. *Journal American Society of Mining and Reclamation*, *2004*(1), 272–294. https://doi.org/10.21000/JASMR04010272

Cravotta Iii, C. A., & Trahan, M. K. (1999). Limestone drains to increase pH and remove dissolved metals from acidic mine drainage. *Applied Geochemistry*, *14*(5), 581–606. https://doi.org/10.1016/S0883-2927(98)00066-3

Davies, S. H., & Morgan, J. J. (1989). Manganese (II) oxidation kinetics on metal oxide surfaces. *Journal of Colloid and Interface Science*, *129*(1), 63–77.

De Klerk, R. J., Feldmann, T., Daenzer, R., & Demopoulos, G. P. (2015). Continuous circuit coprecipitation of arsenic(V) with ferric iron by lime neutralization: The effect of circuit staging, co-ions and equilibration pH on long-term arsenic retention. *Hydrometallurgy*, *151*, 42–50. https://doi.org/10.1016/j.hydromet.2014.11.003

De Klerk, R. J., Jia, Y., Daenzer, R., Gomez, M. A., & Demopoulos, G. P. (2012). Continuous circuit coprecipitation of arsenic(V) with ferric iron by lime neutralization: Process parameter effects on arsenic removal and precipitate quality. *Hydrometallurgy*, *111–112*, 65–72. https://doi.org/10.1016/j.hydromet.2011.10.004

Demopoulos, G. P. (2009). Aqueous precipitation and crystallization for the production of particulate solids with desired properties. *Hydrometallurgy*, *96*(3), 199–214. https://doi.org/10.1016/j.hydromet.2008.10.004

Dirksen, J. A., & Ring, T. A. (1991). Fundamentals of crystallization: Kinetic effects on particle size distributions and morphology. *Chemical Engineering Science*, *46*(10), 2389–2427. https://doi.org/10.1016/0009-2509(91)80035-W

Dzombak, D. A., & Morel, F. M. M. (1990). *Surface complexation modeling: Hydrous ferric oxide*. Wiley.

Evangelou, V. P. (Bill), & Zhang, Y. L. (1995). A review: Pyrite oxidation mechanisms and acid mine drainage prevention. *Critical Reviews in Environmental Science and Technology*, *25*(2), 141–199. https://doi.org/10.1080/10643389509388477

Farley, K. J., Dzombak, D. A., & Morel, F. M. M. (1985). A surface precipitation model for the sorption of cations on metal oxides. *Journal of Colloid and Interface Science*, *106*(1), 226–242. https://doi.org/10.1016/0021-9797(85)90400-X

Fogo, J. K., & Popowsky, M. (1949). Spectrophotometric Determination of Hydrogen Sulfide. *Analytical Chemistry*, *21*(6), 732–734. https://doi.org/10.1021/ac60030a028

Gammons, C. H., & Duaime, T. E. (2006). Long Term Changes in the Limnology and Geochemistry of the Berkeley Pit Lake, Butte, Montana. *Mine Water and the Environment*, *25*(2), 76–85. https://doi.org/10.1007/s10230-006-0114-6

Geldenhuys, A. J., Maree, J. P., de Beer, M., & Hlabela, P. (2003). *An integrated limestone/lime process for partial sulphate removal*. 10.

GoldSim Technology Group (2021), GoldSim User's Guide (Version 14.0), https://www.goldsim.com/Web/Customers/Education/Documentation/, October 2021.

Grundl, T., & Delwiche, J. (1993). Kinetics of ferric oxyhydroxide precipitation. *Journal of Contaminant Hydrology*, *14*(1), 71–87.

Gunsinger, M. R., Ptacek, C. J., Blowes, D. W., & Jambor, J. L. (2006). Evaluation of long-term sulfide oxidation processes within pyrrhotite-rich tailings, Lynn Lake, Manitoba. *Journal of Contaminant Hydrology*, *83*(3–4), 149–170. https://doi.org/10.1016/j.jconhyd.2005.10.013

Hassibi, M. (1999). An Overview Of Lime Slaking And Factors That Affect The Process. *Chemco Systems, L.P.*, 19.

Hem, J. D. (1981). Rates of manganese oxidation in aqueous systems. *Geochimica et Cosmochimica Acta*, *45*(8), 1369–1374.

Hem, J. D. (1985). *Study and interpretation of the chemical characteristics of natural water* (Vol. 2254). Department of the Interior, US Geological Survey.

Huck, P. M., Murphy, K. L., Reed, C., & LeClair, B. P. (1977). Optimization of polymer flocculation of heavy metal hydroxides. *Journal (Water Pollution Control Federation)*, 2411–2418.

Huck, P., Murphy, K., & LeClair, B. (1976). Flocculation of Neutralized Mine Drainage With Polymers. *Water Quality Research Journal*, *11*(1), 46–56.

Jambor, J. L., Dutrizac, J. E., & Raudsepp, M. (2007). Measured and computed neutralization potentials from static tests of diverse rock types. *Environmental Geology*, *52*(6), 1019–1031. https://doi.org/10.1007/s00254-006-0542-4

Janzen, M. P., Nicholson, R. V., & Scharer, J. M. (2000). Pyrrhotite reaction kinetics: Reaction rates for oxidation by oxygen, ferric iron, and for nonoxidative dissolution. *Geochimica et Cosmochimica Acta*, *64*(9), 1511–1522. https://doi.org/10.1016/S0016-7037(99)00421-4

Jenke, D. R., Pagenkopf, G. K., & Diebold, F. E. (1983). Chemical changes in concentrated, acidic, metal-bearing wastewaters when treated with lime. *Environmental Science & Technology*, *17*(4), 217–223. https://doi.org/10.1021/es00110a007

Johnson, D. B., & Hallberg, K. B. (2005). Acid mine drainage remediation options: A review. *Science of The Total Environment*, *338*(1–2), 3–14. https://doi.org/10.1016/j.scitotenv.2004.09.002

Johnson, R. H., Blowes, D. W., Robertson, W. D., & Jambor, J. L. (2000). The hydrogeochemistry of the Nickel Rim mine tailings impoundment, Sudbury, Ontario. *Journal of Contaminant Hydrology*, *41*(1–2), 49–80. https://doi.org/10.1016/S0169-7722(99)00068-6

Jurjovec, J., Ptacek, C. J., & Blowes, D. W. (2002). Acid neutralization mechanisms and metal release in mine tailings: A laboratory column experiment. *Geochimica et Cosmochimica Acta*, *66*(9), 1511–1523. https://doi.org/10.1016/S0016-7037(01)00874-2

Kirby, C. S., & Brady, J. A. E. (1998). Field determination of Fe2+ oxidation rates in acid mine drainage using a continuously-stirred tank reactor. *Applied Geochemistry*, *13*(4), 509–520. https://doi.org/10.1016/S0883-2927(97)00077-2

Kirby, C. S., & Cravotta, C. A. (2005). Net alkalinity and net acidity 2: Practical considerations. *Applied Geochemistry*, *20*(10), 1941–1964. https://doi.org/10.1016/j.apgeochem.2005.07.003

Light, T. S. (1972). Standard solution for redox potential measurements. *Analytical Chemistry*, *44*(6), 1038–1039. https://doi.org/10.1021/ac60314a021

Livingstone, D. M., & Imboden, D. M. (1989). Annual heat balance and equilibrium temperature of Lake Aegeri, Switzerland. *Aquatic Sciences*, *51*(4), 351–369. https://doi.org/10.1007/BF00877177

Machala, L., Zboril, R., & Gedanken, A. (2007). Amorphous Iron(III) OxideA Review. *The Journal of Physical Chemistry B*, *111*(16), 4003–4018. https://doi.org/10.1021/jp064992s

McDonald, D. M., Webb, J. A., & Taylor, J. (2006). Chemical Stability of Acid Rock Drainage Treatment Sludge and Implications for Sludge Management. *Environmental Science & Technology*, *40*(6), 1984–1990. https://doi.org/10.1021/es0515194

Metal and Diamond Mining Effluent Regulations (MDMER) (SOR /2002-222)

Miller, A., Figueroa, L., & Wildeman, T. (2011). Zinc and nickel removal in simulated limestone treatment of mining influenced water. *Applied Geochemistry*, *26*(1), 125–132. https://doi.org/10.1016/j.apgeochem.2010.11.009

Miller, A., Wildeman, T., & Figueroa, L. (2013). Zinc and nickel removal in limestone based treatment of acid mine drainage: The relative role of adsorption and co-precipitation. *Applied Geochemistry*, *37*, 57–63. https://doi.org/10.1016/j.apgeochem.2013.07.001

Miller, G. C., Lyons, W. B., & Davis, A. (1996). The increase in deep pit mining in western North America raises concerns about the environmental impact of mine closure. *Environmental Science & Technology*, *30*(3), 6.

Millero, F. J., CHENt, C.-T., Bradshaw, A., & Schleicher, K. (1980). *A new high pressure equation of state for seawater*. 10.

Moncur, M. C., Ptacek, C. J., Blowes, D. W., & Jambor, J. L. (2006). Spatial variations in water composition at a northern Canadian lake impacted by mine drainage. *Applied Geochemistry*, *21*(10), 1799–1817. https://doi.org/10.1016/j.apgeochem.2006.06.016

Morgan, B., & Lahav, O. (2007). The effect of pH on the kinetics of spontaneous Fe(II) oxidation by O2 in aqueous solution – basic principles and a simple heuristic description. *Chemosphere*, *68*(11), 2080–2084. https://doi.org/10.1016/j.chemosphere.2007.02.015

Nordstrom, D. K., (2020). Geochemical Modeling of Iron and Aluminum Precipitation during Mixing and Neutralization of Acid Mine Drainage. *Minerals*, *10*(6), 547. https://doi.org/10.3390/min10060547

Nordstrom, D. K., & Campbell, K. M. (2014). Modeling Low-Temperature Geochemical Processes. In *Treatise on Geochemistry* (pp. 27–68). Elsevier. https://doi.org/10.1016/B978-0-08-095975-7.00502-7

Nordstrom, D. K., & Jenne, E. A. (1977). Fluorite solubility equilibria in selected geothermal waters. *Geochimica et Cosmochimica Acta*, *41*(2), 175–188. https://doi.org/10.1016/0016-7037(77)90224-1

Parkhurst, D. L., Appelo, C., & others. (1999). User's guide to PHREEQC (Version 2): A computer program for speciation, batch-reaction, one-dimensional transport, and inverse geochemical calculations. *Water-Resources Investigations Report*, *99*(4259), 312.

Patton, C. J., & Crouch, S. (1977). Spectrophotometric and kinetics investigation of the Berthelot reaction for the determination of ammonia. *Analytical Chemistry*, *49*(3), 464–469.

Pham, A. N., Rose, A. L., Feitz, A. J., & Waite, T. D. (2006). Kinetics of Fe(III) precipitation in aqueous solutions at pH 6.0–9.5 and 25°C. *Geochimica et Cosmochimica Acta*, *70*(3), 640–650. https://doi.org/10.1016/j.gca.2005.10.018

Pieters, R., & Lawrence, G. A. (2009). Effect of salt exclusion from lake ice on seasonal circulation. *Limnology and Oceanography*, *54*(2), 401–412. https://doi.org/10.4319/lo.2009.54.2.0401

Pieters, R., & Lawrence, G. A. (2014). Physical processes and meromixis in pit lakes subject to ice cover. *Canadian Journal of Civil Engineering*, *41*(6), 569–578. https://doi.org/10.1139/cjce-2012-0132

Pigage, L. C., Abbott, J., & Turner, R. (1990). Field guide Anvil Pb-Zn-Ag district, Yukon Territory, Canada. *Mineral Deposits of the Northern Canadian Cordillera, Yukon-Northeastern British Columbia*, *2169*, 283–308.

Sánchez España, J., Pamo, E. L., Pastor, E. S., & Ercilla, M. D. (2008). The acidic mine pit lakes of the Iberian Pyrite Belt: An approach to their physical limnology and hydrogeochemistry. *Applied Geochemistry*, *23*(5), 1260–1287. https://doi.org/10.1016/j.apgeochem.2007.12.036

Singer, P. C., & Stumm, W. (1970). Acidic Mine Drainage: The Rate-Determining Step. *Science*, *167*(3921), 1121–1123. https://doi.org/10.1126/science.167.3921.1121

SRK (2020), 2019 Faro Pit Monitoring Report. Technical Memo.

Steinhart, J. S., & Hart, S. R. (1968). Calibration curves for thermistors. *Deep Sea Research and Oceanographic Abstracts*, *15*(4), 497–503. https://doi.org/10.1016/0011-7471(68)90057-0

Tan, H., Zhang, G., Heaney, P. J., Webb, S. M., & Burgos, W. D. (2010). Characterization of manganese oxide precipitates from Appalachian coal mine drainage treatment systems. *Applied Geochemistry*, *25*(3), 389–399. https://doi.org/10.1016/j.apgeochem.2009.12.006

Todd, E. C., Sherman, D. M., & Purton, J. A. (2003). Surface oxidation of pyrite under ambient atmospheric and aqueous (pH = 2 to 10) conditions: Electronic structure and mineralogy from X-ray absorption spectroscopy. *Geochimica et Cosmochimica Acta*, *67*(5), 881–893. https://doi.org/10.1016/S0016-7037(02)00957-2

Usher, B., Roald, S., Strachotta, C., & Jackson, J. (2010). *Proceedings IMWA 2010*. 4.

Webb, M. R. (1992). A continuous spectrophotometric assay for inorganic phosphate and for measuring phosphate release kinetics in biological systems. *Proceedings of the National Academy of Sciences*, *89*(11), 4884–488